UNIVERSITÀ DI PARMA

UNIVERSITA' DEGLI STUDI DI PARMA

DOTTORATO DI RICERCA IN SCIENZE DEL FARMACO,
DELLE BIOMOLECOLE E DEI PRODOTTI PER LA SALUTE

CICLO XXXIV

INVESTIGATION OF THE INFLUENCE OF HYALURONIC ACID MOLECULAR WEIGHT ON CHARACTERISTICS AND BEHAVIOUR OF NANOPARTICLES FOR PULMONARY DRUG DELIVERY

Coordinatore:
Chiar.mo Prof. Marco Mor

Tutore:
Chiar.mo Prof. Ruggero Bettini

Dottorando: Laura Bertocchi

Anni Accademici 2018/2019 - 2020/2021

SUMMARY

CHAPTER 2

CHAPTER 4

List of Symbols and Acronyms

ALI	Air-liquid interface
AmB	Amphotericin B
AUC	Area under the curve
α-CD	α-cyclodextrin
β-CD	β-cyclodextrin
CD44	Cluster of differentiation 44
CF	Cystic fibrosis
CFC	Course fraction collector
CFTR	Cystic fibrosis transmembrane conductance regulator
Cps	Capsule
CS	Chitosan
$D_v(10)$	10^{th} percentile volume diameter
$D_v(50)$	Volume median diameter
$D_v(90)$	90^{th} percentile volume diameter
Dev	Device
DMSO	Dimethyl sulfoxide
DPI	Dry powder inhaler
DLS	Dynamic light scattering
DSC	Differential scanning calorimetry
DX	Dexamethasone
ED	Emitted dose
EE	Encapsulation efficiency
EF	Emitted fraction
FBS	Fetal bovine serum
FFC	Fine fraction collector
FLZ	Fluconazole
FPD	Fine particle dose
FPF	Fine particle fraction
FSI	Fast screening impactor
FT-IR	Fourier-transform infrared spectroscopy
GSD	Geometric standard deviation
HA	Sodium hyaluronate
HPLC	High pressure liquid chromatography
IP	Induction port
Leu	Leucine
LOD	Limit of detection
LOQ	Limit of quantification
MMAD	Mass median aerodynamic diameter
MOC	Micro-orifice collector
MW	Molecular weight
NGI	Next generation impactor
NP	Nanoparticles
PB	Phosphate buffer
PdI	Polydispersity index
PG	Propylene glycol
q_{peak}	q value of the correlation peak
SAXS	Small-angle X-ray scattering
SD	Spray drying
SEM	Scanning electron microscopy
WAXS	Wide-angle X-ray scattering
XRPD	X-ray powder diffraction
ζ	Zeta potential

List of Figures

List of Tables

List of Equations

AIM OF THE THESIS

The aim of the present thesis was to set up a platform for pulmonary drug delivery based on hyaluronic acid (HA) as *active* excipient. The biological effects of the polymer in the lungs and its technological role suggested to better investigate hyaluronic acid for the construction of nanoparticulate and nano-embedded microparticulate respirable powders for pulmonary drug delivery to exploit said properties. In particular, it has been widely demonstrated that its biological behaviour is strictly dependent on its molecular weight (MW), promoting opposite inflammatory responses at cellular level when present at high MW or when depolymerized into shorter chains at low MW.

The first aim of the present thesis was the investigation of the influence of seven different ranges of HA MW on characteristics of HA nanoparticles obtained by anti-solvent precipitation using ethanol as the anti-solvent. In addition, the best conditions to produce small nanoparticles with a narrow particle size distribution were assessed and established for each range of HA MW *(Chapter 1)*.

The second aim of the thesis was the loading of three different model drugs used for the treatment of pulmonary diseases: amphotericin B, fluconazole and dexamethasone (*Chapters 2, 3 and 4*, respectively). A method to produce drug-loaded HA nanoparticles was developed according to the solubility of each drug and a specific HA MW range was selected for particle production to exploit its biological effect in synergy with the payload. Powders for inhalation were then produced by spray drying and characterized.

CHAPTER 1

Sodium hyaluronate-based nanocarriers for pulmonary drug delivery

1. INTRODUCTION

1.1 Sodium hyaluronate

1.1.1 Physico-chemical properties

Hyaluronic acid is a glycosaminoglycan consisting of repeating disaccharide units of glucuronic acid and N-acetyl-glucosamine (*Figure 1, Panel A* [1]) [2]. The number of disaccharide units can reach 10000, leading to a molecular mass around 4000 kDa. The structure of hyaluronic acid presents a non-polar backbone with a relatively hydrophobic face and more polar side chains involved in the creation of intra- and inter-molecular hydrogen bonds (*Panel B*).

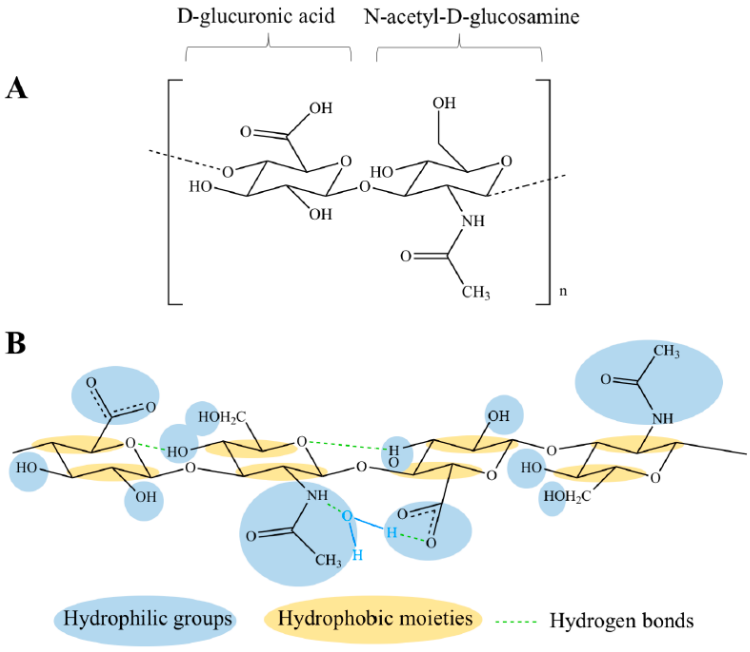

Figure 1. Chemical structure of hyaluronic acid. Reproduced with permission from [1].

At physiological pH, the carboxyl groups present an anionic charge, balanced with cations such as Na+, K+ and Ca2+: in this form, hyaluronic acid is called hyaluronan or hyaluronate (HA) [3]. This structure manifests hydrophilic characteristic, providing particular rheological properties due to the entanglement among chains and to the

interaction with the solvent. Polymeric solutions, in fact, present jelly-like texture with a very high but shear-dependent viscosity, typical of the so-called "pseudo-plastic" materials. The viscoelastic nature of HA is at the base of some biological functions of the polymer, naturally found in connective tissues, skin, umbilical cord, synovial fluid and vitreous humour. Here, it is involved as lubricant, thanks to its high ability to bind water and to control tissue hydration, and these functions are correlated to its role as main constituent of the extracellular matrix (ECM) [4]. At the same time, HA occurs also intracellularly, presenting a biological role in several cellular functions.

1.1.2 Biological functions

Together with connective tissues, sodium hyaluronate is found in lungs, kidney, brain and muscle tissues. It is naturally involved as signalling molecule in cell motility, tumour development and metastasis, immunological processes and wound healing. In addition, it possesses an antioxidant activity [4]. In the cells, it is synthetized by transmembrane enzymes called hyaluronan synthases (HAS), able to produce HA molecules with high molecular weight (HMW), from 30 kDa to more than 2000 kDa according to the HAS isoform (HAS1, HAS2 and HAS3). Its degradation is accomplished by catabolic enzymes named hyaluronidases (HYAL), together with non-specific reactive oxygen species (ROS) that generate HA fragments at low molecular weight (LMW) (*Figure 2*, [1]).

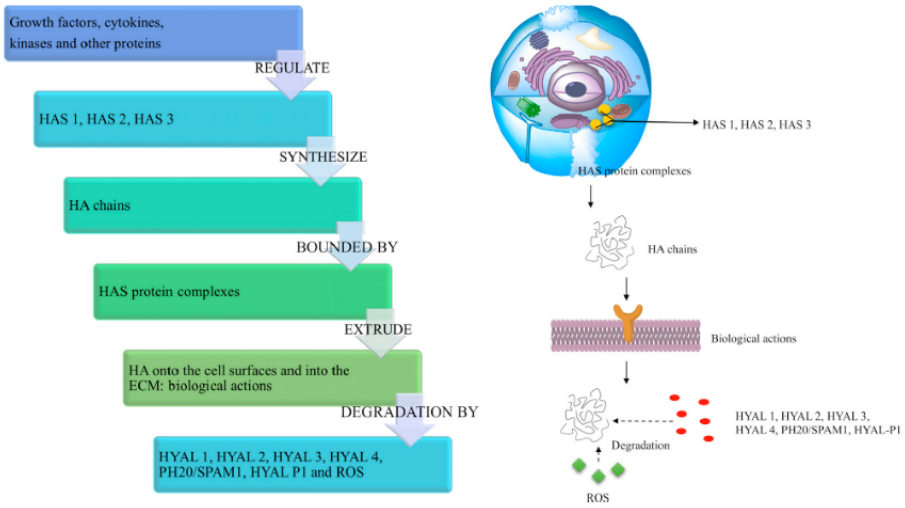

Figure 2. Schematic description of HA metabolism. Reproduced with permission from [1].

The equilibrium between the synthesis and degradation of HA plays a key role in the biological functions of the polymer, that strictly depend on its molecular weight [5][6][7][8]. In fact, as part of the ECM, during pathological conditions such as inflammation or tumour invasion, HMW-HA is degraded into fragments with LMW and then depolymerized into oligosaccharides (oHA) able to act as pro-inflammatory signals with opposite functions compared to those of HA they derived from [9][10][11]. Increased levels of LMW-HA have been found in many lung disorders including asthma, pulmonary fibrosis, COPD, allergic alveolitis, interstitial lung disease, sarcoidosis, and pulmonary hypertension as well as other inflammatory diseases like rheumatoid arthritis. LMW-HA can also induce angiogenesis and tumour progression. On the contrary, endogenous HMW-HA can either protect from epithelial apoptosis in lung injury or promote an invasive fibroblast phenotype and the fibrotic process [12]. These different biological functions are due to the interaction of HA with its receptors, summarized in *Figure 3* [1].

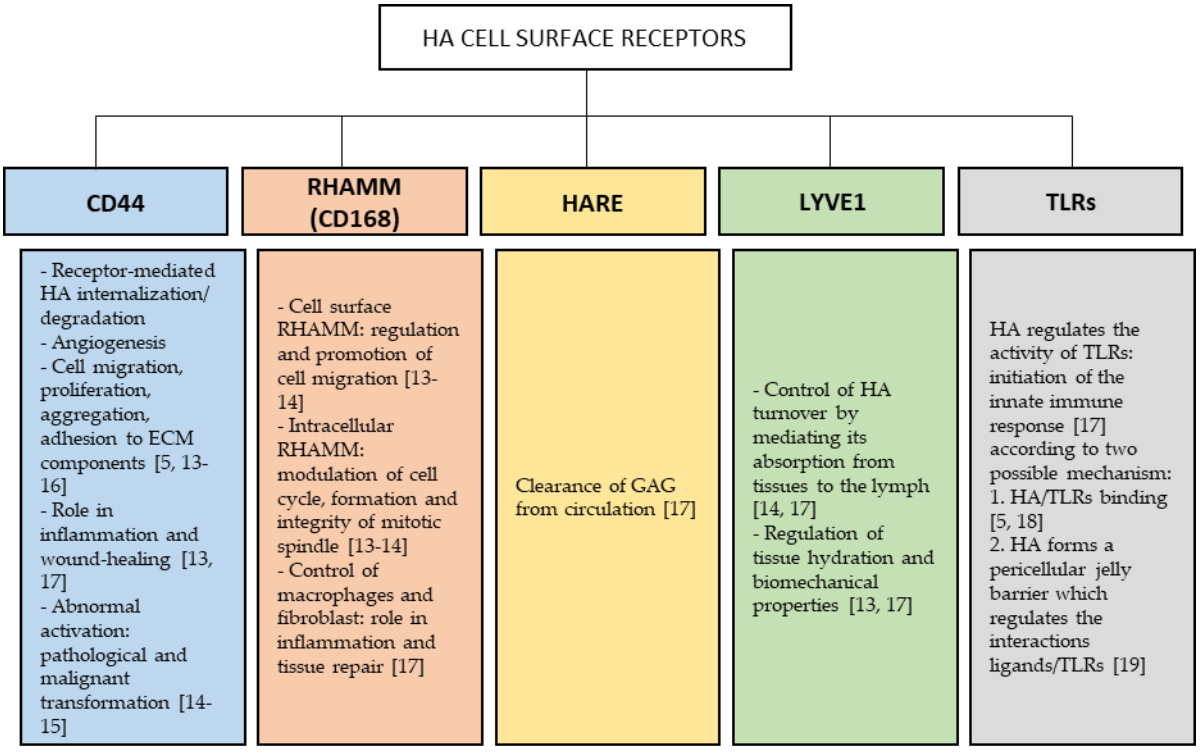

Figure 3. Summary of HA cell surface receptors. Modified with permission from [1].

It has been widely demonstrated that their responses after HA binding are strictly related to the polymer MW, as demonstrated for the toll-like receptors (TLRs), able to promote cytokine release and airway hyperresponsiveness when activated by LMW-HA

[20][21][22], but with protective functions when bound to HMW-HA [23]. Among HA receptors, the most important is the Cluster of differentiation-44 (CD44), presenting a higher affinity for HMW and LMW compared to oHA. It is involved in binding, endocytosis and metabolism of hyaluronan, but also in additional biological functions of HA in innate and adaptive immunity. Rayahin and colleagues investigated the influence of HA MW on the activation of macrophages after its interaction with CD44 surface receptors, bringing to a deeper understanding of the influence of the polymer on the regulation of inflammatory response. *Figure 4* clearly describes the effect of HA, whose interaction is able to promote phenotypic changes of macrophages depending on its MW [24]:

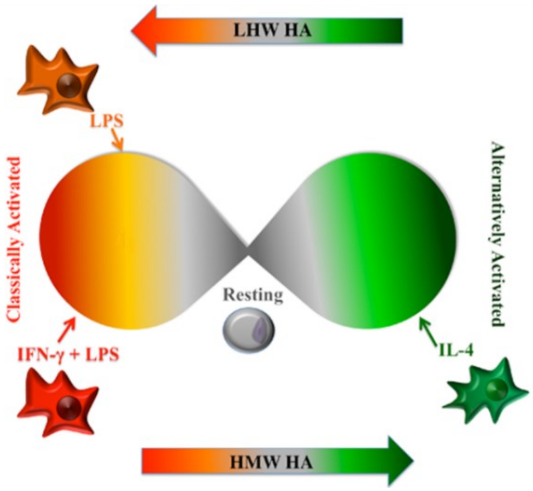

Figure 4. Macrophages polarization after interaction and activation of LMW-HA and HMW-HA. Reproduced with permission from [24].

A classically activated state was observed in macrophages after interaction of LMW-HA with CD44 receptor, that promoted an up-regulation of pro-inflammatory cytokines and genes such as *nos2*, *il-12b* and *cd80* and an enhanced secretion of NO and TNF-α. In contrast, an alternatively activated state was promoted after interaction with HMW-HA, with an up-regulation of pro-resolving genes transcription such as *arg1* and *il-10.*

1.1.3 Clinical application of sodium hyaluronate

The biocompatibility and non-immunogenicity of HA, together with its viscoelastic nature, has led to its application in several fields, including the supplementation of joint

fluid in arthritis, as a surgical aid in eye surgery, to facilitate the healing and regeneration of wounds and in tissue engineering [25][26]. Thanks to its moisturizing, regenerative and protective effects it is used in cosmetics. The anti-inflammatory effect of the polymer with HMW led also to the use of HA in the treatment of inflammatory disease [27][28] and respiratory conditions such as rhinosinusitis, chronic obstructive pulmonary disease (COPD), asthma, cystic fibrosis and pulmonary hypertension, by modulating LMW-HA signalling with HMW-HA (*Figure 5*) [29].

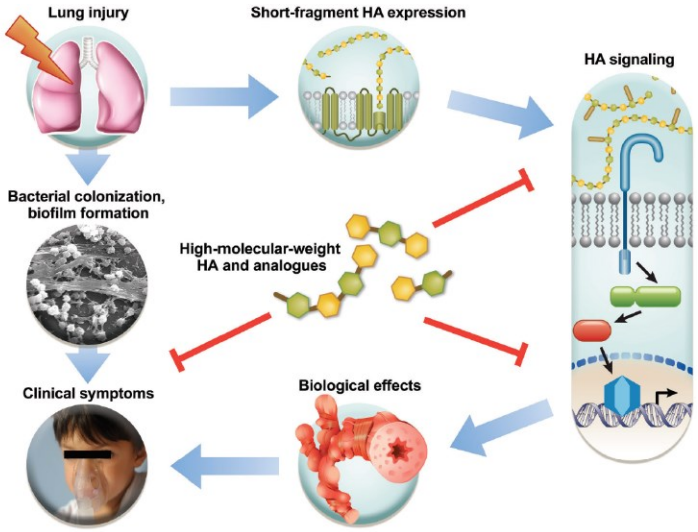

Figure 5. Clinical application of HMW-HA in respiratory diseases. Reproduced with permission from [29].

Finally, HA was deeply investigated for drug targeting in treatment of diseases presenting over-expressed CD44 receptor, employing drug delivery systems such as nanoparticles [30][31][32].

1.2 Nanoparticles for drug delivery

1.2.1 General aspects

Nanoparticles (NP) are particles that present structural components smaller than 1 μm in at least one dimension. This characteristic related to their size confers to these kind of materials particular properties, such as a large surface area and the consequent high

particle number per unit mass [33]. Nanotechnology resulted very promising to improve disease diagnosis and treatment specificity, overcoming the limitations of conventional delivery *(Figure 6, Panel A)*, together with the stabilization of the cargo and the higher safety and efficacy [34]. Engineered nanoparticles can be obtained according to the desired target, modulating their size, shape, morphology and surface properties *(Panel B)*.

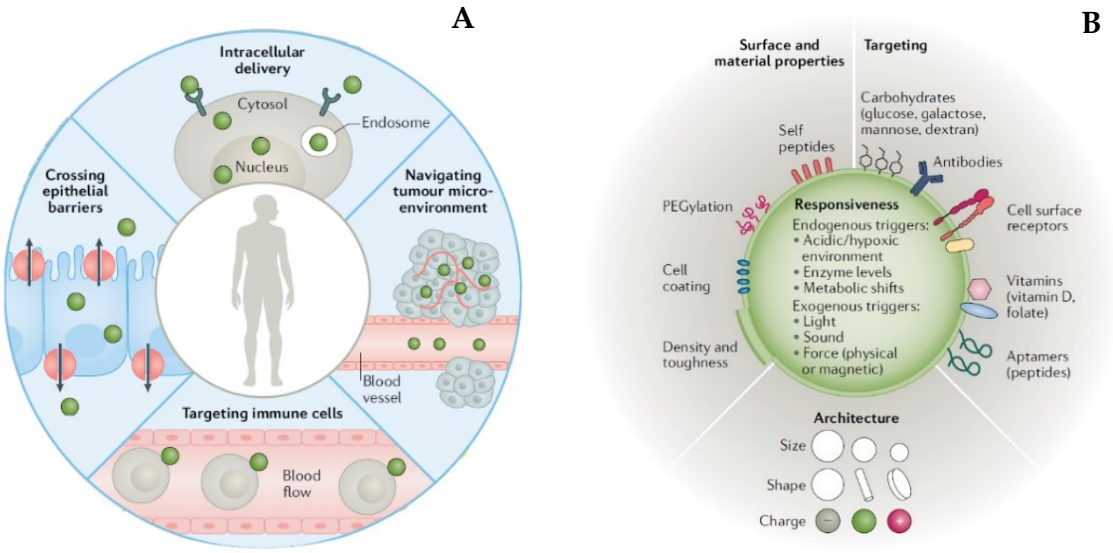

Figure 6. Schematic representation of advantages (Panel A) and properties (Panel B) of nanoparticles. Reproduced with permission from [34].

In the pharmaceutical field, NP can be classified into three main categories based on their composition: inorganic, polymeric and lipid-based NP. Inorganic NP, mainly composed of gold, iron or silica, present a large variability of size and shapes, together with unique electrical and magnetic properties that suggest their application in diagnostic, imaging and photothermal therapies. Among lipid-based NP, liposomes, composed of phospholipids, are the most common class of FDA-approved nanomedicines, offering many advantages such as the facility of formulation, biocompatibility and ability to carry large payloads. Finally, polymeric NP represent the widest class, composed of natural or synthetic polymers. They can be synthesized using various technique, such as emulsification (solvent displacement or diffusion), nanoprecipitation, ionic gelation and microfluidics, obtaining structures able to entrap hydrophobic or hydrophilic drug molecules as well as biological macromolecules inside the core, chemically conjugated to

the polymer or bound on their surface. The most common categories of polymeric NP are nanocapsules, composed by a core surrounded by a polymeric shell, and nanospheres, constituted by a solid matrix system. The advantages offered by polymeric NP consist mainly in the easy surface modifications for obtaining specific targeting and their water solubility, biocompatibility and stability during storage [35][34]. Synthetic polymers employed for NP production, such as polylactide acid (PLA), polyglycolide acid (PLG) and poly(lactide coglycolide) acid (PLGA), and natural polymers such as sodium alginate, albumin, chitosan and hyaluronic acid should guarantee biocompatibility and biodegradability avoiding toxicity and antigenicity [36][37].

1.2.2 Sodium hyaluronate nanoparticles

Hyaluronic acid is one of the main constituents of the extracellular matrix in mammals and for this reason it has been investigated as polymer for NP production, thanks to the good biocompatibility, biodegradability and non-immunogenicity. In addition, the ability to recognize and bind specific receptors over-expressed in some diseases has corroborated its application as carrier in drug delivery systems [30]. Different HA NP have been proposed, based on polymeric cross-linking [38] and polyelectrolyte complexes with chitosan [39][40][41], chitosan and heparin [42] and polyarginine [43]. In order to exploit HA active targeting, it has been proposed also as coating for drug delivery systems [8]. CD44 over-expression led to the development of HA NP for drug delivery to alveolar macrophages [44][45], atherosclerotic tissues [31] and in particular to cancer cells [46][47][48][49].

1.2.3 Nanoparticles for pulmonary drug delivery

Pulmonary drug delivery presents many advantages compared to other routes of administration such as oral delivery or injection. Lungs have in fact high permeability, a

large surface area for absorption and a limited enzymatic degradation. In addition, it can be exploit for both local and systemic applications while still being non-invasive for the patients. The targeted delivery for local treatments allows to reduce the doses and the side effects usually resulting from high levels of systemic drug exposure. In contrast, systemic drug delivery can be achieved by targeting alveolar region where the drug can be absorbed through the thin layer of epithelial cells into the systemic circulation avoiding the first-pass metabolism typical of the oral administration (*Figure 7*, [50]) [45].

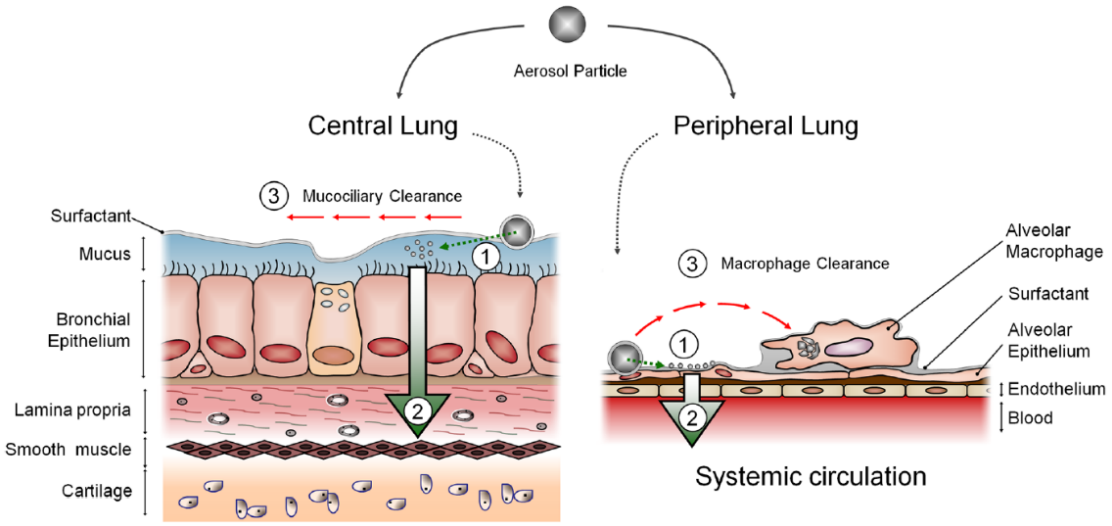

Figure 7. Anatomy of high and low regions of the lungs. Reproduced with permission from [50].

Devices for inhalation have been divided into three main categories, including nebulizers, pre-metered dose inhalers (pMDI) and dry powder inhalers (DPI). Formulations for nebulizers are cheaper and easier to develop compared to the others and are useful for paediatric, elderly, ventilated and non-conscious patients since no coordination between inhalation and actuation is required. pMDI are the most popular inhalers to treat local respiratory diseases and contain formulations such as solutions or suspensions with one or more propellants activated by the patients. Coordination between inhalation and actuation is required and not always successful for the administration of the drug. Finally, DPI are portable and breath-actuated devices. Formulations for DPI, consisting of a respirable dry powders, present higher chemical and microbiological stability compared to formulations needed for other kind of devices, but appropriate characteristics are

required to obtain a proper aerosolization of the powder and a successful pulmonary delivery of the drug [52].

After inhalation, in fact, particles deposit along the respiratory tracts from the upper (oropharynx, trachea and bronchi) to the lower (respiratory bronchioles and alveolar sacs) airways and are cleared by cilia within the mucous layer or by alveolar macrophages depending on their deposition [51][53].

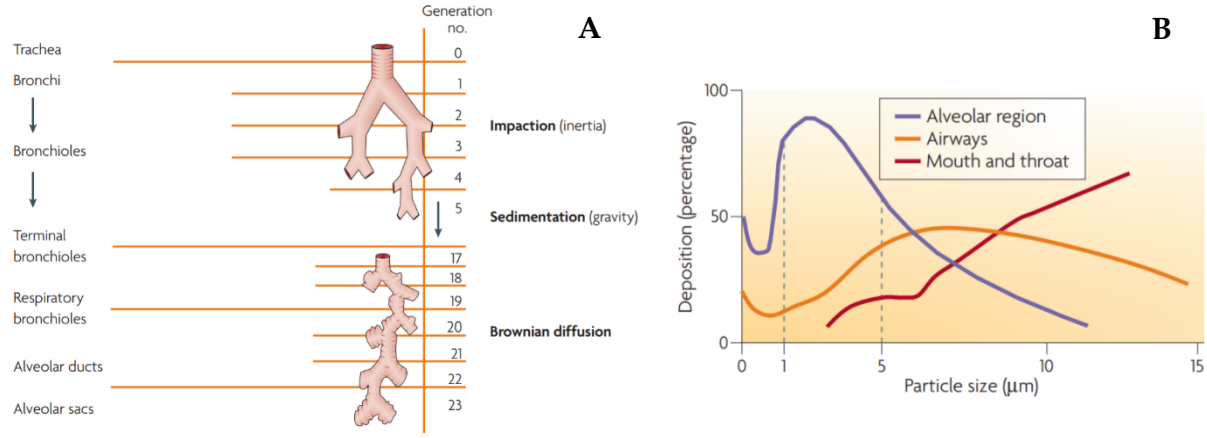

Figure 8. Mechanism of particle deposition (Panel A) according to their aerodynamic diameter (Panel B). Reproduced with permission from [51].

The deposition occurs by inertial impaction, sedimentation and diffusion and it depends on the aerodynamic diameter of the particles, d_{ae}, calculated according to the following equation:

$$d_{ae} = \sqrt{d_g \frac{\rho}{\rho_{ae}}} \qquad (Eq.\ 1)$$

where ρ is the mass density of the particle, ρ_{ae} is the unit mass (1 g/cm^3) and d_g is the geometric diameter. Particles with $d_{ae} > 5$ µm deposit by inertial impaction in the mouth and upper airways, while smaller particles with $d_{ae} = 1 - 5$ µm deposit deeper in the lungs and in the alveolar region by inertial impaction and sedimentation. Particles with $d_{ae} < 1$ µm are driven by diffusion, but mostly remain suspended and are exhaled.

For this reason, nanoparticles administered by inhalation must be formulated as nano-embedded microparticles in order to guarantee the deposition in the lower airways without losing the advantages offered by particles in the nanometre range. In addition to

those described in *paragraph 1.2.1*, in fact, nanoparticles offer other advantages related to their ability to overcome lungs defence mechanisms [51]. Mechanical and immunological barriers represent the main ones, consisting of impaction, entrapment and removal of particle by lung mucociliary clearance and particle engulfment by alveolar macrophages, respectively [54][55]. The fate of nanoparticles is strictly related to their physicochemical properties, including size, surface charge and hydrophobicity. More details will be described in *paragraph 1.2* (Chapter 2) [56].

2. AIM

The first aim of the present part of the thesis was to develop sodium hyaluronate nanoparticles for drug delivery, exploiting both the technological and biological properties of the polymer. The influence of its molecular weight was investigated, deepening its effect on the production as well as on the final characteristics of the nanoparticles by dynamic light scattering.

Secondly, a method for producing Amphotericin B-loaded nanoparticles was explored, investigating first the solvent to be used to solubilize the drug and then the effect of the drug concentration on the characteristics of nanoparticles obtained with different sodium hyaluronate molecular weights.

3. MATERIALS AND METHODS

3.1 MATERIALS

Sodium Hyaluronate at different molecular weights (15-30, 50-90, 130-300, 750-1000, 1000-1250, 1500-1750, 2000-2200 kDa) were obtained from *Contipro*, Czech Republic. Amphotericin B was supplied by *Dayangchem*, China. Ultrapure water was purified by reverse osmosis with Purelab Pulse flex, *Elga-Veolia*, Italy.

3.2 METHODS

3.2.1 Measurement of the viscosity of sodium hyaluronate solutions

The viscosities of polymeric solutions were compared after measurements at room temperature using a rotational viscometer (Smart, *Fungilab*, USA) with different spindles *(Table 1).*

Table 1. Codes of spindles employed for the measurement of the viscosity of HA aqueous solution at different concentrations of HA MW > 250 kDa.

HA % (w/v)	**0.25%**	**0.5%**	**0.75%**	**1%**
100-400 kDa	-	-	-	R2
750-1000 kDa	R3	TR8	TR8	TR8
1000-1250 kDa	TR8	TR8	TR9	TR9
1500-1750 kDa	R3	TR9	TR9	TR9
2000-2200 kDa	R3	TR9	TR9	TR9

For HA 250 kDa, the viscosity was measured at different rotation rates (10 - 60 rpm) due to its pseudo-plastic behaviour and the mean was then calculated for each HA%. For HA MW > 250 kDa, the viscosities of the solutions were compared after fixing the speed at 50

rpm. For HA MW < 250 kDa, because of the difficulty of measuring the viscosities due to their low values, a capillary viscosimeter was created using a Silberbrand Eterna® glass pipette type 3, volume = 1 mL and length = 360 mm. Viscosities were compared by measuring the time needed by the polymeric solutions for flowing from notch 0.1 mL to notch 0.5 mL.

3.2.2 Preparation of blank and AmB-loaded NP

Sodium hyaluronate nanoparticles were obtained by anti-solvent precipitation using ethanol as the anti-solvent. For blank NP, sodium hyaluronate was first dissolved in ultrapure water. The optimal concentration of the polymeric solution was assessed for each range of MW in order to obtain the most appropriate viscosity value, as will be explained in *paragraph 4.1.1*. Ethanol was then added dropwise to the aqueous solution kept under stirring at 165 rpm at fixed temperature (25°C or 45°C), promoting the nanoprecipitation of the polymer. The volume of ethanol to add to the HA solution was assessed for each MW by analysing by dynamic light scattering the nanosuspension after each addition of small volumes of anti-solvent.

AmB-loaded nanoparticles were obtained by anti-solvent precipitation as for blank NP. AmB was first solubilized in propylene glycol at a concentration of 1 mg/mL, the value of solubility obtained by HPLC *(paragraph 3.2.3)* and confirmed in literature [57]. The drug solution was mixed under stirring at room temperature with the polymeric aqueous solution and ethanol was added dropwise to the mixture, acting as anti-solvent for both the polymer and the drug.

3.2.3 High Pressure Liquid Chromatography

Dissolved AmB was quantified in solubility measurement experiments by liquid chromatography using an HPLC Agilent technologies 1200 (*Agilent*, USA). The method was set modifying the one proposed by Echevarria and colleagues [58]:

1. Column = Reversed-phased column Ascentis C_{18}, 150 mm x 4.6 mm, 3µm
2. Flux rate = 0.8 mL/min
3. Temperature = 25 °C
4. Injection volume = 50 µL
5. Detection λ = 405 nm
6. t_{run} = 8 minutes (t_{rit} = 3 minutes)
7. Mobile phase = 41% v/v Acetonitrile, 43% v/v Acetic Acid at 10% v/v, 16% v/v Water.

The analytical method was assessed in terms of linearity of response (Area Under the Curve, AUC, of the peak at 3 minutes *vs* concentration) in the concentration range 0.2 - 20 µg/mL. Limit of Quantification (LOQ) and Limit of Detection (LOD) were calculated as follows:

$$LOD = 3.3\ \sigma/slp \qquad (Eq.\ 2)$$

$$LOQ = 10\ \sigma/slp \qquad (Eq.\ 3)$$

where *slp* and σ are the slope and the standard deviation of most diluted sample of the regression line absorbance *vs* concentration *(Figure 9)*, respectively. In the set conditions LOQ was 0.233 µg/mL and LOD = 0.0768 µg/mL.

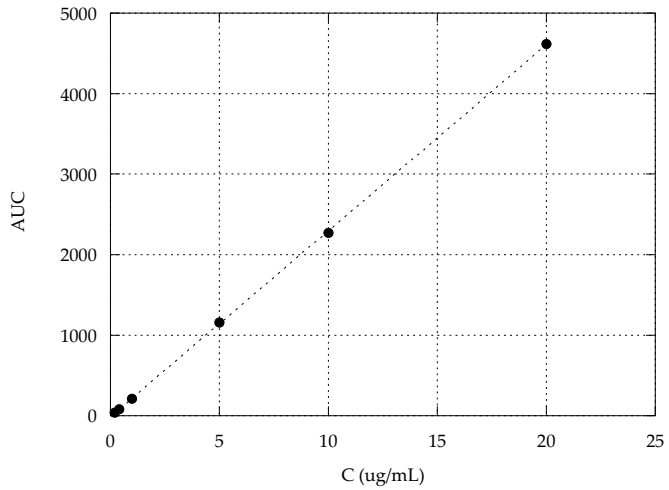

Figure 9. Calibration curve of AmB in mobile phase: y = -12.921 + 231.05x, R^2 = 0.99994.

AmB solubility was assessed by sampling from a 3 mg/mL suspension of AmB in propylene glycol left to equilibrate at ambient temperature for 30, 60, 90 and 120 minutes. The samples were filtered using a 0.45 μm filter in cellulose acetate and diluted 1:100 in mobile phase before injection. The integrated area of the peak was converted into concentration using the calibration curve reported in *Figure 9*.

3.2.4 Dynamic Light Scattering

Size and size distribution of blank and AmB-loaded nanoparticles were assessed by Dynamic Light Scattering (Zetasizer Nano ZS, *Malvern Panalytical*, UK). One mL of nanosuspension was loaded into a cuvette DTS0012 and the parameters were set as follow:

1) Material: RI = 1.336 (blank NP); 1.59 (AmB-loaded NP); Absorption = 0.010
2) Dispersant: Viscosity (25°C) = 1.3022 cP; RI = 1.354
3) Temperature = 25°C
4) Cuvette = DTS0012
5) Angle of detection = 173° Backscatter
6) Equilibration time = 60s
7) Number of measurements = 3

All samples were analysed at their actual concentration, except for the nanosuspensions containing HA 130-300 kDa and AmB at different concentrations, for which a dilution 1:20 was performed before DLS analysis.

4. RESULTS AND DISCUSSION

4.1 Assessment of the optimal conditions for HA nanoparticles precipitation

4.1.1 Concentration of HA aqueous solution

Rheological properties of sodium hyaluronate have been demonstrated to be related to its MW and concentration [59][60][61][62]. With their increase, HA networks are strengthened, and HA solutions present increased viscosity and viscoelasticity. In addition, HA rheological properties in aqueous solutions are influenced by ionic strength, pH and temperature: as these factors increase, HA viscosity decreases markedly, suggesting a weakening of the interactions among the polymeric chains [1]. A proper viscosity represents a prerequisite for particles production because of the strong influence that it imparts to the freedom of polymeric chains to move and interact each other. To establish HA initial concentration, HA with molecular weight ranging from 100 to 400 kDa (HA 250kDa) was chosen and four different concentrations were tested (1%, 2%, 3%, 5% w/v) *(Figure 10)*.

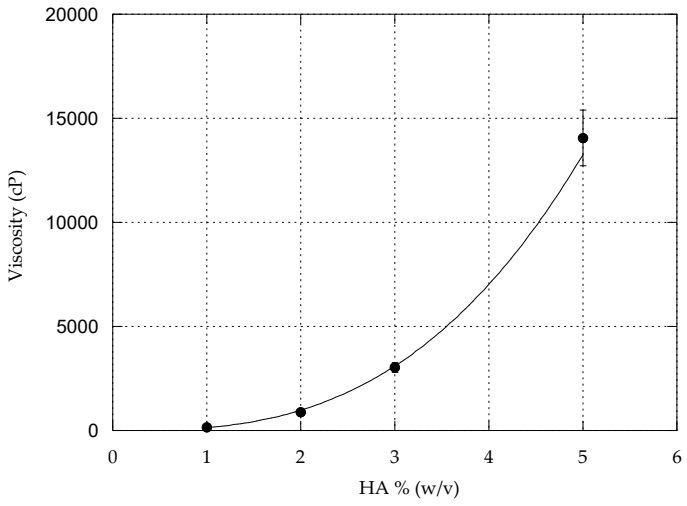

Figure 10. Viscosity of HA 250 kDa aqueous solutions at different concentrations. The bars represent the standard deviation (n = 5). The line is the interpolation of the experimental points with the Power equation: $y = 135.78\ x^{2.8462}$, $R^2 = 0.99984$.

As expected, the viscosity of HA solutions presented an increase with the increase of the polymer concentration, explained by the higher possibility of polymeric chains to bind water. Interestingly, the trend of the experimental points reported in *Figure 10* was well described and fitted with a Power Equation with R^2 = 0.99984, highlighting the strict dependence of viscosity on the cubed concentration of the polymer *(y = 135.78 * x^2.8462)*.

Aqueous solutions at different concentrations of HA with MW > 250 kDa were prepared and their viscosity measured with the rotational viscosimeter. Also in these cases the strong dependence between the polymer concentration, MW and viscosity was observed *(Figure 11)*.

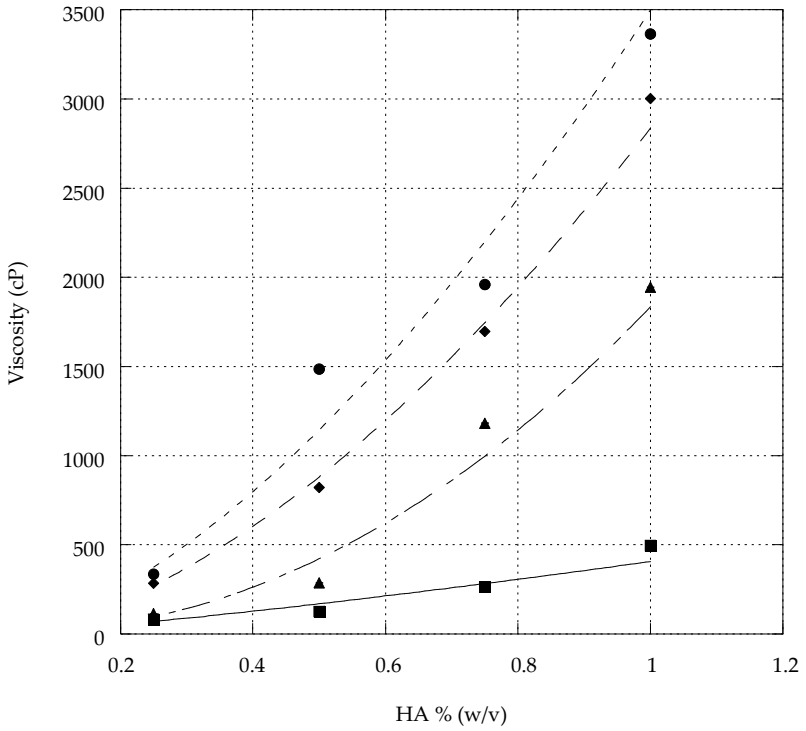

Figure 11. Viscosities of HA solutions at different concentrations (MW > 250 kDa): —■— HA 750-1000 kDa, -▲— HA 1000-1250; —◆— HA 1500-1750 kDa; - -●- - HA 2000-2200 kDa. The bars represent the standard deviation (n=4).

Experimental points were interpolated also in this case with a power equation, with a quite good fitting, thus further supporting this type of relation between viscosity and HA concentration as described by the following equation:

$$Viscosity = a\ HAconcentration^{b} \qquad (Eq.\ 4)$$

where a is a constant and b the power exponent.

The parameters of the fitting equations are reported in *Table 2*.

Table 2. Parameters of Eq. 4 obtained from solution of HA at different MW.

HA MW (kDa)	a	b	R^2
750-1000	406.5	1.26	0.941
1000-1250	1835.1	2.12	0.982
1500-1750	2836.3	1.69	0.996
2000-2200	3497.5	1.61	0.968

The *b* values are included in a small interval ranging from 1.2 and 2.1. As for the values of the *a* parameter, they can be directly compared to each other only when the *b* values are identical as the *a* parameter has dimension Viscosity x $Concentration^{-b}$. As stated, the *b* values are all included in a relatively narrow interval, thus a rough comparison can be done as a first approximation evidencing an increase of this parameter as a function of the HA MW, which is also clearly visible from *Figure 11* that reports a progressive increase of the slope of the curves with the increase of the polymer molecular weight.

Preliminary information about the influence of HA concentration on particle precipitation were collected considering the four HA 250kDa solutions previously prepared *(paragraph 4.1.1)*. Ethanol was then added until a light blue opalescence was observed as macroscopic signal of the precipitation of nanoparticles.

Table 3. Size and size distribution (PdI) of particles obtained at different concentrations of HA250 kDa.

HA% (w/v)	Size (nm)	PdI
1%	107.2	0.29
2%	345.8	1
3%	270.7	1
5%	258.3	0.47

Dynamic light scattering (DLS) analyses showed that smaller NP with lower PdI (107 nm; PdI = 0.29) were obtained starting from the polymeric solution at 1% w/v *(Table 3)*. The viscosity of this solution, measured using a rotational viscosimeter, was about 145 cP. In contrast, nanosuspensions obtained starting from HA solutions at 2%, 3% and 5% w/v and presenting higher values of viscosity (880, 3033 and 14053 cP, respectively) led to the formation of nanoparticles above 250 nm in size and with a higher polydispersity. For this reason, the value of viscosity of this solution was fixed as target for the preparation of HA solutions with higher and lower MW, proving to be the more suitable condition for the diffusion and migration of polymeric chains in solution and their entanglement into nanoparticles. For comparison with other HA MW, the viscosity of HA solution at 1% w/v taken as reference was the one measured at 50 rpm, amounting to 126.7 cP.

Values of viscosity of HA solutions, ranging from 0.12% to 1% w/v, are reported in *Table 4*. The target value, corresponding to 126.7 cP, is circled in red to facilitate the comparison with the viscosities of other solutions. For other HA MW, all values of viscosity are reported in the table, and the most suitable ones, chosen for particle production according to the target value 126.7 cP, are marked in bold phase.

Table 4. Viscosities of HA aqueous solutions (cP) with HA MW > 250 kDa. The viscosity taken as approximate target and given by the solution containing HA 100-400 kDa at 1%, is circled in red. Similar values obtained from solutions with higher HA MW are reported in bold phase, corresponding to the more suitable HA concentrations be used for nanoparticle formation for each MW range.

	C_{HA} (% w/v)					
HA MW (kDa)	**0.12%**	**0.15%**	**0.25%**	**0.50%**	**0.75%**	**1%**
100-400	-	-	-	-	-	126.7
750-1000	-	-	83.4	**126.5**	265.8	495.1
1000-1250	-	-	**113.8**	286.9	1182.7	1945.0
1500-1750	**108.6**	140.9	284.7	822.1	1697.2	3001.7
2000-2200	**146.6**	160.5	336.5	1486.0	1958.9	3364.5

As expected, for higher HA MW it was necessary to reduce the concentration to obtain approximately comparable values of viscosity. The most suitable HA concentrations chosen for particle production were 0.5% w/v for HA 750-1000 kDa, 0.25% w/v for HA 1000-1250 kDa and 0.12% w/v for HA 1500-1750 kDa and 2000-2200 kDa.

A similar procedure was employed for HA MW < 250 kDa. For these ranges of HA MW, the values of viscosity were not measurable with a rotational viscosimeter because they were too low and below the detection limit of the instrument; thus, a different method was used as reported in the method section *(paragraph 3.2.1)*. For comparison purpose, the time taken by polymeric solutions to flow between two fixed point of a glass pipette was measured. The values, amounting to few seconds, are reported in *Table 5*. Also in this case the target, represented by the HA 100-400 kDa solution at 1% w/v and corresponding to 11.7 s, is circled in red to facilitate the comparison with other solutions. For other HA MW, all times are reported in the table, and the most suitable ones, chosen for particle production according to the target value 11.7 s, are marked in bold.

Table 5. Time taken by HA solutions (MW < 250 kDa) at different concentrations to flow between two fixed points of a glass pipette (s). The time taken by the solution containing HA 100-400 kDa at 1% and fixed as approximate target is circled in red. Similar values obtained from solutions with lower HA MW are reported in bold phase, corresponding to the more suitable HA concentrations to be used for the particle formation for each MW range.

	C_{HA} % (w/v)							
HA MW (kDa)	**1%**	**2%**	**3%**	**4%**	**5%**	**6%**	**7%**	**8%**
15-30	-	1.2	1.4	2.7	3.5	4.1	5.5	**12.8**
50-90	-	4.2	**9.3**	23.0	-	-	-	-
100-400	11.7	-	-	-	-	-	-	-

This method allowed for the comparison of HA solutions and for getting information about the more suitable polymer concentration for particle formation. This technique, which is based on the theory of the Ostwald viscosimeter, gave just first approximative information about HA solutions. This approximation was due to home-made set-up of the

technique, but also to the fact that the concentration of the polymeric solutions tested were higher than 1% w/v with consequent significant inter-molecular interactions impacting on the viscosity. Nevertheless, all considered, this method was useful for a simple comparison among polymeric solutions, and it worked just as a starting point for the production of nanoparticle with different HA MW thanks to the comparison with the HA 100-400 kDa range already investigated. From this results, the most suitable HA concentrations chosen for particle production were 8% w/v for HA 15-30 kDa and 3% w/v for HA 50-90 kDa.

4.1.2 Volume of anti-solvent

Once fixed the initial HA concentration of the aqueous solutions, ethanol was added to promote the precipitation of the polymer. The formation of nanoparticles was monitored by interspersing the addition of small volumes of ethanol with DLS measurements. This process was carried out for each range of HA MW to assess the optimum volume of anti-solvent needed to precipitate nanoparticles with small size and reduced polydispersion. The volume of the polymeric starting aqueous solution was fixed at 5 mL.

The trend of experimental points collected and reported in *Figures 12-18* was very similar for each range of HA MW. With the increase of the volume of the added ethanol, hydrodynamic diameters of NP showed an initial increase, reaching a maximum immediately followed by a reduction of the size. This trend, quite similar for each HA MW, presented some differences analysed in detail below.

For HA 15-30 kDa, the HA starting concentration at 8% w/v led to the aggregation of particles above 1 μm *(Figure 12, red star)* after passing the maximum point. For this reason, HA concentration was reduced from 8% to 4% w/v to promote the formation of nanoparticle avoiding the precipitation of aggregates due to the excess of polymeric chains. Nevertheless, this condition led to the same event but at higher volume of added ethanol. The HA concentration was therefore reduced to 2% w/v. Hydrodynamic diameters of NP, reported in *Figure 12* with dots, showed the same trend with a slightly

shifted maximum point to higher volume of added ethanol. In contrast to higher HA concentrations, the maximum was followed by a reduction of size until reaching a value no longer influenced by the increase in ethanol.

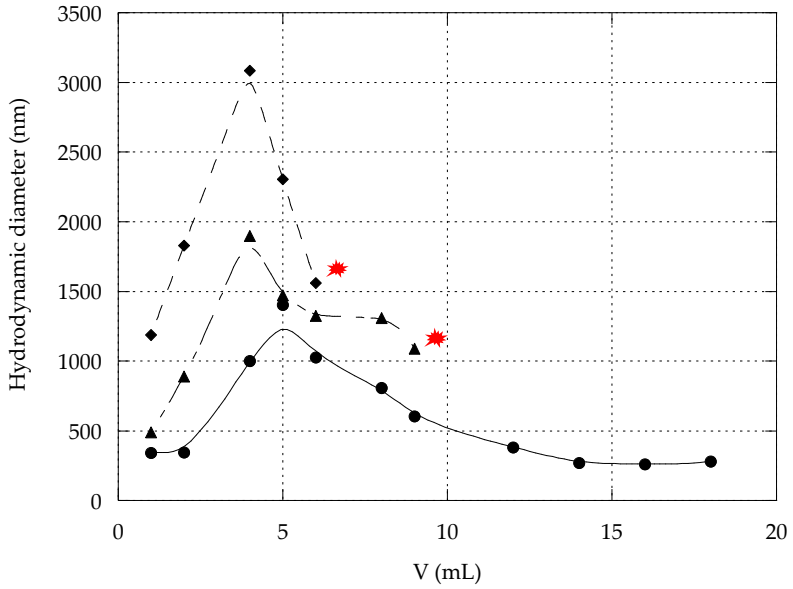

Figure 12. Hydrodynamic diameter (nm) of NP obtained with HA 15-30 kDa at 8% (w/v) —◆— , 4% (w/v) -▲— and 2% (w/v) —●— , as a function of volume of added ethanol (mL); Red stars: particle aggregates above 1 µm.

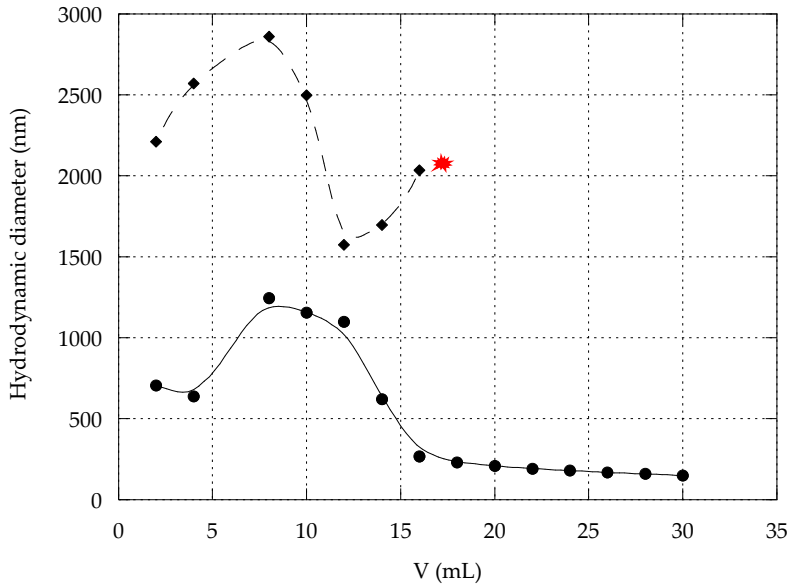

Figure 13. Hydrodynamic diameter (nm) of NP obtained with HA 50-90 kDa at 3% (w/v) —◆— and 1.5% (w/v) —●— , as a function of volume of added ethanol (mL); Red star: particle aggregates above 1 µm.

For HA 50-90 kDa, the same behaviour was observed at high HA concentration (3% w/v), with the formation of aggregates above 1 µm at each volume of added ethanol and the obtainment of visible precipitates after the addition of 17 mL of ethanol *(Figure 13, red star)*.

In contrast, the reduction of HA concentration to 1.5% w/v led to the typical trend already observed for the hydrodynamic diameter with a decrease of the size after the maximum point and the obtainment steady NP with almost constant diameter.

A similar trend was observed also for HA 750-1000 kDa and HA 1000-1250 kDa at the established HA concentrations, amounting to 0.5% and 0.25% w/v, respectively *(Figures 14* and *15)*.

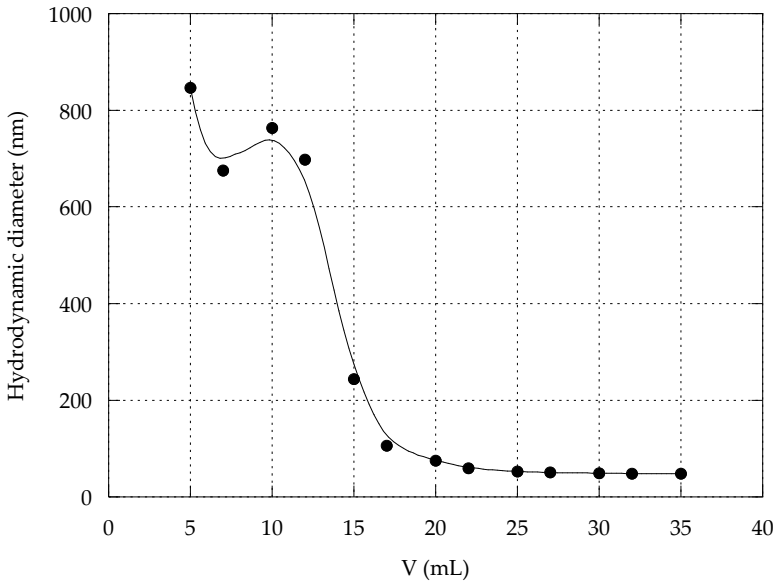

Figure 14. Hydrodynamic diameter (nm) of NP obtained with HA 750-1000 kDa at 0.5% (w/v) as a function of volume of added ethanol (mL).

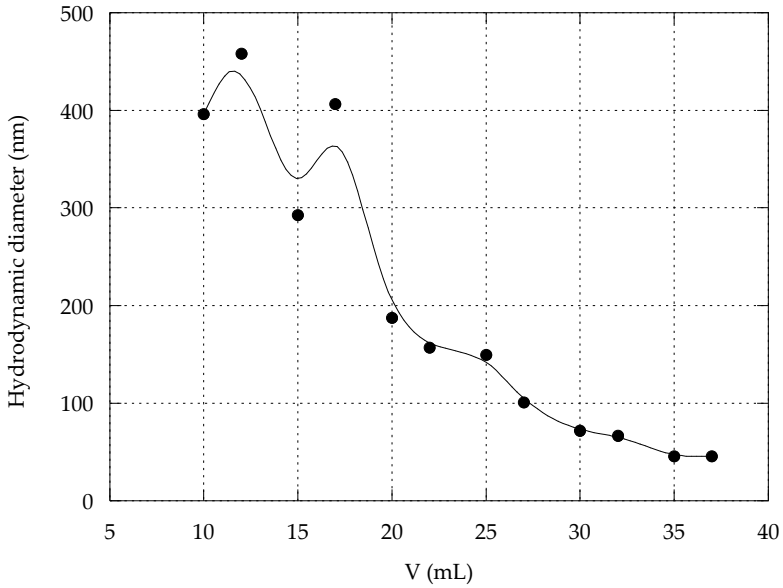

Figure 15. Hydrodynamic diameter (nm) of NP obtained with HA 1000-1250 kDa at 0.25% (w/v) as a function of volume of added ethanol (mL).

In both cases, the maximum value of hydrodynamic diameter was obtained after the addition of higher volume of ethanol (> 10 mL) compared to lower HA MW ranges, as well as the obtainment of steady particles in case of HA 1000-1250 kDa *(Figure 15)*, reached at 87.5% v/v (35 mL) of ethanol.

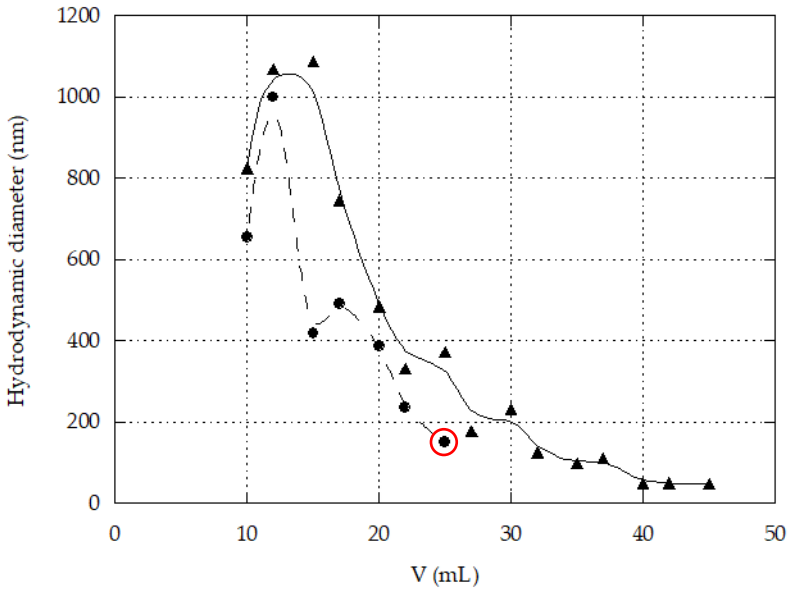

Figure 16. Hydrodynamic diameter (nm) of NP obtained with HA 1500-1750 kDa at 0.12% (w/v) as a function of volume of added ethanol (mL) and precipitated at 25°C —●— and 45°C —▲— . Red circle: PdI > 0.9.

As concern HA 1500-1750 kDa, the initial HA concentration fixed at 0.12% (w/v) led to the precipitation of nanoparticles with a very high polydispersity index (PdI > 0.9) *(Figure 16, red circle)*. For this reason, the temperature was increased during the precipitation process rather than reducing the HA concentration, in order to reduce the solution viscosity and to enhance the mobility of polymeric chains. The temperature, increased from 25°C to 45°C, led to the formation of nanoparticles with a PdI < 0.45. The trend of experimental points observed was the same also at higher temperature, with a maximum point after the addition of more than 10 mL and the achievement of stable particles above 40 mL of added ethanol.

In the case of HA 2000-2200 kDa, the trend of hydrodynamic diameters observed was different compared to lower HA MW. As it can be observed in *Figure 17*, in fact, at the established HA concentration fixed at 0.25% (w/v), the addition of ethanol led to a decrease

of size without reaching a maximum point at low volume of anti-solvent. Values of hydrodynamic diameter decreased until the addition of 30 mL ethanol, that led to the formation of nanoparticles of 100 nm in size and the simultaneous precipitation of some aggregates above 1 μm *(red star)*. The reduction of HA concentration to 0.12% (w/v) led to the same event, with the co-existence of nanoparticles of 500 nm and bigger visible aggregates. Finally, the addition of ethanol to HA aqueous solution at 0.06% (w/v), led to the typical trend of hydrodynamic diameter observed for lower HA MW: the maximum point, reached after the addition of 12 mL of ethanol, was less evident compared to other HA MW, but also in this case it was followed by a reduction of size with the increase of added ethanol.

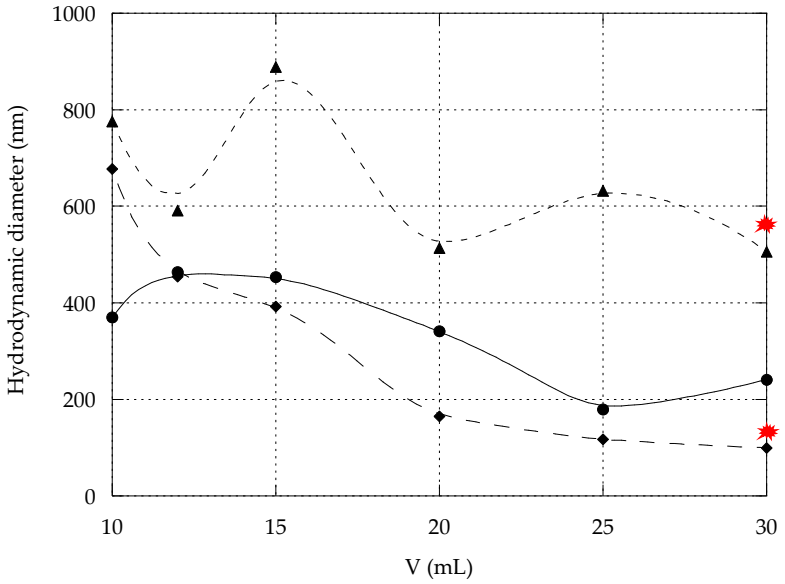

Figure 17. Hydrodynamic diameter (nm) of NP obtained with HA 2000-2200 kDa at 0.25% (w/v) —◆— , 0.12% (w/v) - -▲- - and 0.06% (w/v)—●— , as a function of volume of added ethanol (mL); Red stars: precipitated aggregates above 1 μm.

The reduction of HA concentration, that successfully led to the formation of nanoparticles instead of bigger aggregates, did not positively influence the polydispersion of particles, that presented a PdI > 0.8 also after the addition of 30 mL of ethanol *(Figure 18, red circle)*. For this reason, once again as it was done for HA 1500-1750 kDa, the temperature during the formation of particles was increased from 25°C to 45°C, leading to a reduction of PdI value to 0.55.

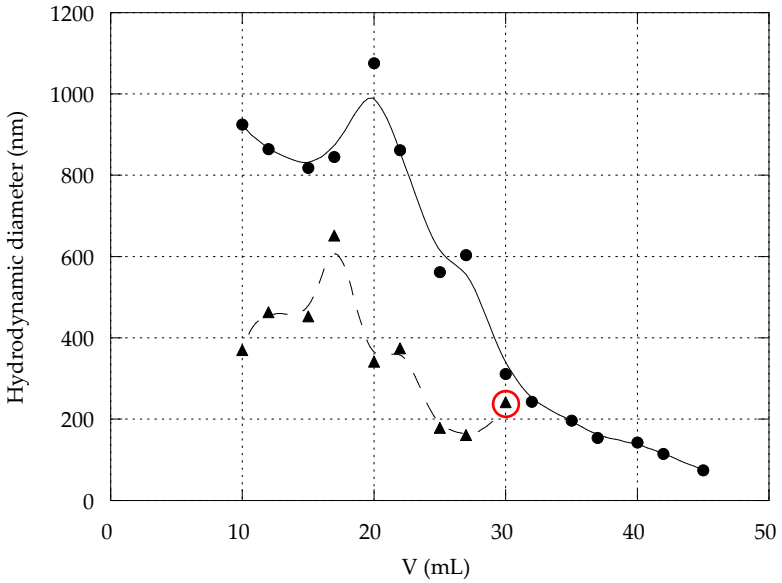

Figure 18. Hydrodynamic diameter (nm) of NP obtained with HA 2000-2200 kDa at 0.06% (w/v) as a function of volume of added ethanol (mL) and precipitated at 25°C —▲— and 45°C —●— . Red circle: PdI > 0.8.

According to what was observed from these studies, the volume of anti-solvent and HA concentration have a significant influence on the size of the particles obtained with each HA MW range, and the temperature on their polydispersion. In addition, with the increase of HA MW, the typical trend characterized by the maximum point, the subsequent decrease of size as well as the achievement of a steady particle size, is shifted to higher volume of ethanol, suggesting its direct dependence on HA MW.

To sum up, *Table 6* reports the optimized conditions for the formation of NP prepared with different HA MW: the initial HA concentration, the temperature, the volume of ethanol, as well as the final particle characteristics in term of size and size distribution. As is it possible to observe, compared to other MW ranges, HA 15-30 kDa nanoparticles exhibited a very low PdI. This behaviour could be due to the higher number of polymeric chains and to the faster replacement of water molecules by ethanol, leading to a faster inter-chain contact and binding. The continuous addition of ethanol could positively affect particles distribution, improving their homogeneity and uniformity. In contrast, NP obtained with HA 750-1000 kDa presented a size distribution comparable to those of lower HA MW, but hydrodynamic diameters like NP obtained with higher HA MW. This different behaviour could be ascribed again to the lower number of polymeric chains that leads to the

formation of smaller nanoparticles but characterized by a lower polydispersity thanks to the quite faster replacement of water molecules by ethanol.

Table 6. Particle size and Polydispersity Index (PdI) of HA NP at different MW obtained in optimized conditions as a function of initial HA concentration (C_{HA} % w/v), volume % of added ethanol ($V_{Ethanol}$ % v/v), and temperature (T). Mean values ± standard deviation (n = 3).

HA MW (kDa)	C_{HA} (% w/v)	$V_{Ethanol}$ (% v/v)	T (°C)	Size (nm)	PdI
15-30	2	76.2	25	482.8 ± 28.8	0.07 ± 0.04
50-90	1.5	85.7	25	121.6 ± 5.9	0.24 ± 0.01
130-300	1	80	25	133.4 ± 17.8	0.25 ± 0.03
750-1000	0.5	87.5	25	47.54 ± 10.4	0.19 ± 0.09
1000-1250	0.25	87.5	25	67.6 ± 3.8	0.57 ± 0.01
1500-1750	0.12	90	45	47.9 ± 7.3	0.45 ± 0.02
2000-2200	0.06	90	45	63.4 ± 12.9	0.37 ± 0.09

These preliminary results led to point out some outcomes.

First of all, the advantages of the anti-solvent precipitation technique, that allows to obtain easily polymeric NP without the addition of other excipients [39] or cross-linking agents [38]. Indeed, the entanglements intra- and inter-chains are stabilized by H-bonds and hydrophobic patches [2] that permit the association of chains despite their negative charge after the addition of the anti-solvent. Second, the different amount of anti-solvent needed for nanoparticle precipitation with different HA MW: a higher volume of ethanol was required for HA HMW compared to HA LMW (90% *vs* 76%, v/v), likely due to the higher degree of hydration of the polymeric chains. Finally, the different characteristics of NP obtained with different HA MW, that presented smaller size and higher polydispersity when prepared with HA HMW compared to HA LMW. This peculiarity was observed also with cross-linked HA NP [63], and it is likely ascribable to a higher amount of intra-chains interactions in case of HA HMW compared to HA LMW. The latter, having a lower number of sites of interaction because of shorter chains, gave rise to the formation of bigger nanoparticles.

4.2 Investigation of the influence of MW on particle size and size distribution of sodium hyaluronate nanoparticles

To better understand the influence of HA MW on the final characteristics of NP, HA concentration and temperature were fixed for each HA MW range (HA 0.06% w/v, 45°C). In contrast, ethanol was added by interspersing DLS measurements to assess the formation of NP. In *Table 7* the volume of anti-solvent employed is reported for each HA MW, together with the size and size distribution of NP obtained.

Table 7. Particle size and Polydispersity Index (PdI) of HA NP at different MW at 45°C starting from a HA concentration of 0.06% w/v as a function of volume of added ethanol ($V_{Ethanol}$ % v/v). Mean values ± standard deviation (n = 3).

MW (kDa)	$V_{Ethanol}$ (% v/v)	Size (nm)	PdI
15-30	28.6	192.4 ± 14.6	0.23 ± 0.05
50-90	50	358.9 ± 1.6	0.42 ± 0.31
130-300	54.5	464.2 ± 8.3	0.28 ± 0.09
750-1000	50	416.8 ± 4.5	0.47 ± 0.03
1000-1250	90	87.9 ± 42.2	0.36 ± 0.14
1500-1750	90	50.6 ± 1.9	0.39 ± 0.03
2000-2200	90	76.6 ± 2.3	0.43 ± 0.18

Data reported in *Table 7* confirm that even in comparable initial conditions of HA concentration and temperature, NP with lower diameter were obtained with high HA MW, being the threshold represented by a MW around 1000 kDa. Below this value, in fact, the NP dimension was of several hundred nm, whereas above the size dropped well below 100 nm. In addition, a quite large particle size distribution (PdI around 0.4) was observed for these small particles. Such polydispersity was due to the presence of 3 main peaks of different intensity ranging from 10-90 nm, 100-600 nm and above 1 μm.

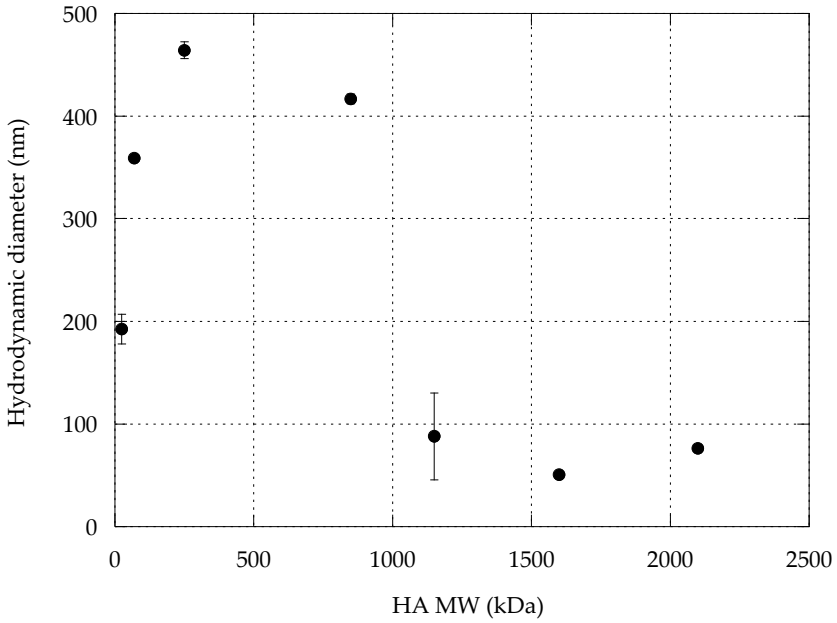

Figure 19. Particle size of HA NP at different MW obtained at 45°C starting from a HA concentration of 0.06% w/v. The bars represent the standard deviation (n = 3).

4.3 Nanoparticles obtained with HA 2000-2200 kDa

In order to reduce the polydispersity of nanoparticles obtained with HA 2000-2200 kDa, the trend of the intensity of different peaks was monitored in greater detail after the addition of small volumes of anti-solvent.

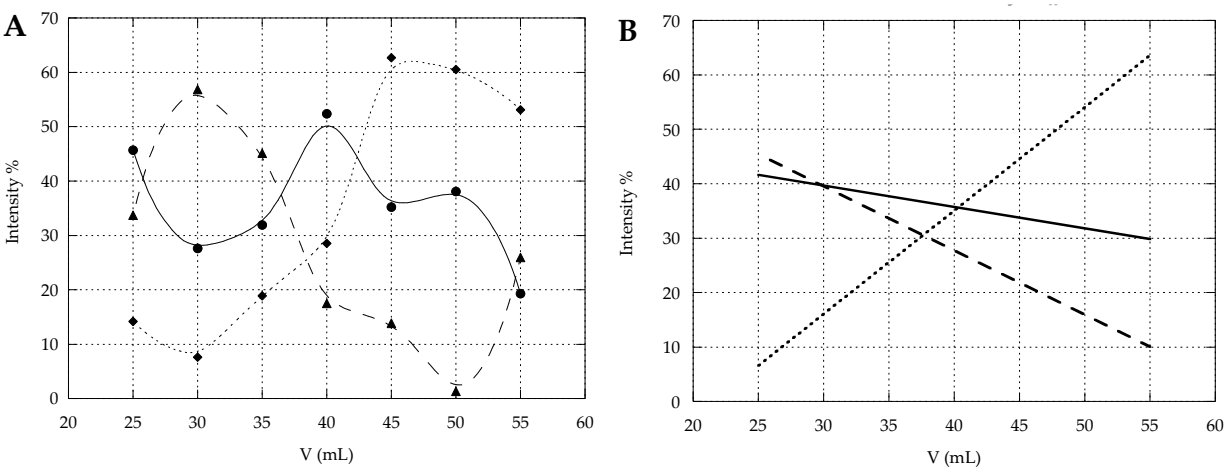

Figure 20. Panel A: Trend of peaks intensity as function of volume of added ethanol (mL): Peak 1 (10-90 nm) ····◆···· , Peak 2 (100-600 nm) —●— and Peak 3 (> 1 µm) –▲– ; Panel B: Fitting of experimental points with linear curves: Peak 1 (10-90 nm) ····· , Peak 2 (100-600 nm) ——— , and Peak 3 (> 1 µm) – – .

The experimental points, simply reported in *Figure 20 (Panel A)* were then interpolated with linear curves to better visualize their trend *(Panel B)*.

The intensity of the peak between 100-600 nm always ranged between 30 - 50% of the relative intensity, indicating that this particle population was substantially independent of the amount of anti-solvent added to the HA aqueous solution. In contrast, the two other peaks showed an opposite trend: an increase of the intensity of the lower peak (between 10 - 90 nm) and a decrease of the intensity of the higher one (aggregates above 1 μm) with the increase of amount of anti-solvent. The amount of ethanol clearly influenced the size of nanoparticles, leading to their reduction with the increase of anti-solvent.

Based on these results, therefore, ethanol at 90% v/v (45 mL added to 5 mL of HA aqueous solution) was fixed as volume of anti-solvent needed to obtained NP with the higher percentage of particle in the 10 - 90 nm range and lower number of aggregates. Given the strict correlation between size and volume of anti-solvent, the further step was to increase the anti-solvent/solvent ratio over time too, adding the whole amount of ethanol in one single shot. The volume was kept fixed at 45 mL (90% v/v).

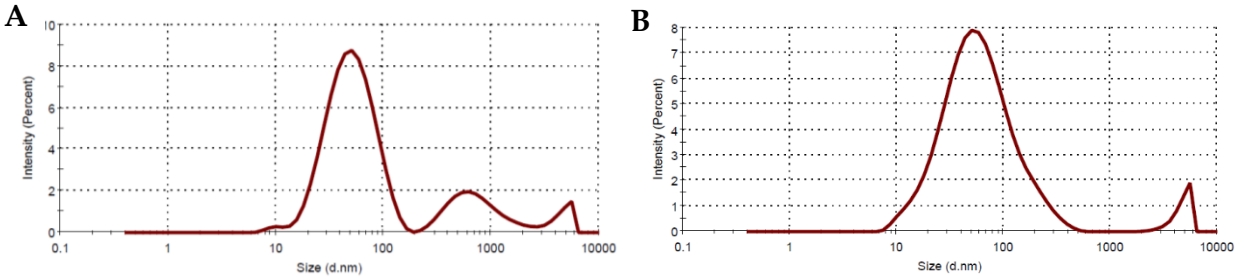

Figure 21. Size distribution of NP obtained with ethanol (90% v/v) added dropwise (Panel A) and in one single shot (Panel B).

The obtained particle size distribution is reported in *Figure 21 (Panel B)* in comparison to the NP size distribution obtained in the same condition but adding the anti-solvent dropwise *(Panel A)*. In both conditions an average particle size around 55 nm was obtained. The size and intensity of the peak > 1 μm was unaffected by the anti-solvent addition mode (about 4.5 μm with intensity around 4.8%) whereas the intensity of the peak < 100 nm increased significantly (from about 75% to about 95%) passing from

dropwise addition to one shot addition. With the one-shot addition the second peak (100-600 nm) was not detected as such. It is worth underling that in this case the particles population classified in the range < 100 nm showed a standard deviation higher than the corresponding one obtained with dropwise addition (62.2 *vs* 26.5) indicating that the change in the addition mode in practice determined the incorporation of the second peak into the first one. However, overall, the particles obtained with the one-shot addition of the anti-solvent presented a narrower size distribution (PdI = 0.35) compared to the nanoparticles obtained by adding ethanol dropwise (PdI = 0.51).

These results highlight the importance of the method employed for the addition of anti-solvent, in addition to its ratio. The increase of anti-solvent/solvent ratio over time, in fact, promotes the reduction of the polydispersion and enhances the precipitation of nanoparticles with a narrower distribution.

4.4 Amphotericin B-loading into HA nanoparticles

4.4.1 Preparation of Amphotericin B-loaded HA nanoparticles

Amphotericin B (AmB), an antifungal drug employed for the treatment of pulmonary infection, was the first active ingredient tested for the production of NP with HA. AmB was selected in order to exploit HA targeting to alveolar macrophages through CD44 binding [64] and thus, to tackle the intracellular fungal infection in the lung.

Different methods were tested for loading AmB into HA nanoparticles and for this purpose, HA 130-300 kDa, a medium HA MW among the investigated ones, was taken as model for preliminary tests.

Method 1

As a first step, the solubility of AmB was investigated. According to the European Pharmacopoeia, AmB is practically insoluble both in water and in ethanol, but soluble in DMSO and propylene glycol (PG). Due to the toxicity of DMSO, propylene glycol was selected as solvent for the drug. In literature, the solubility of AmB in mixture of PG and PEG400 with ethanol (EtOH) has been reported [65]. Deeper information about its solubility in these mixtures was so investigated by HPLC according to the method described in the methods section *(paragraph 3.2.3)* and reported in *Figure 22*.

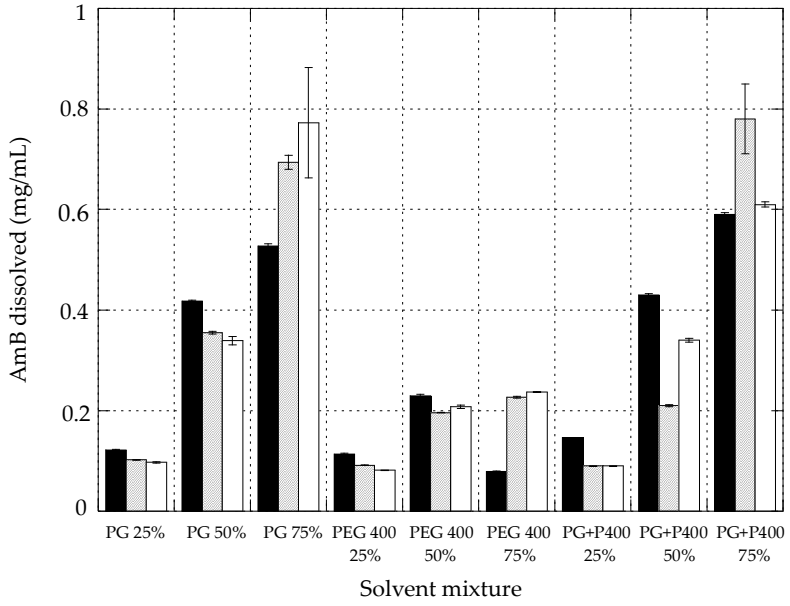

Figure 22. Amount of AmB dissolved in different mixture of propylene glycol (PG), PEG 400 (P400) and PG/P400 in ethanol after 2h ■ , 5h □ and 24h □ . The bars represent the standard deviation (n = 3).

All the mixtures were tested and added to the HA aqueous solution at 1% (w/v) to investigate their ability to precipitate HA nanoparticles. Alcoholic mixtures containing PEG400 75%, PG 25% and PG/PEG400 50% promoted the precipitation of smaller nanoparticles with hydrodynamic diameters in the range 350 - 450 nm. For this reason, they were selected and employed for the preparation of drug loaded particles. AmB was so solubilized in these mixtures at the concentrations established by HPLC, corresponding to 0.2, 0.1 and 0.4 mg/mL in PEG 400 75%, PG 25% and PG/PEG400 50%, respectively. The

mixtures were then added dropwise to the aqueous solutions of HA 1% (w/v) to get a final an alcoholic mixture concentration of 75%, 83% and 86% (v/v, mixture with water). During the process, stirring rate was fixed at 165 rpm and temperature at 45°C. In all cases, nanoparticles with size > 700 nm and relatively high polydispersion (PdI > 0.35) were obtained. For this reason, the method was discarded.

Method 2

The second method based on the preparation of AmB nanoparticles and the promotion of precipitation of polymeric chains onto AmB NP forming AmB-HA nanocapsules. The method employed for the preparation of AmB NP was derived from the one proposed by Zu and colleagues, substituting DMSO with propylene glycol for the solubilization of AmB [66]. 1.5 mL of drug solution was added into 20 mL of ethanol containing 0.15% Tween 80 and left under stirring at room temperature for 30 minutes. AmB nanoparticles with a hydrodynamic diameter around 250 nm were obtained. However, the addition of the AmB nanosuspension into 5 mL of HA solution at 1% w/v promoted a decrease of particle size, although not statistically significant *(Table 8)*.

Table 8. Particle size and size distribution (PdI) of NP obtained with method 2.

	Size (nm)	**PdI**
NP AmB	250.7 ± 8.5	0.382 ± 0.029
NP AmB + HA	194.7 ± 64.6	0.418 ± 0.095

The method was discarded because of the high variability of the particle size as well as of the too high size distribution after the addition of the AmB nanosuspension to the polymeric solution.

Method 3

The third method based on the mixture of AmB and HA before the addition of ethanol, in order to promote the simultaneous precipitation of the drug and the polymer.

For this purpose, 5 mL of aqueous solution containing HA 130-300 kDa at 1% (w/v) was prepared and filtered with a cellulose acetate filter (0.45 μm). AmB was solubilized in PG according to its solubility, assessed by HPLC and confirmed in literature to be 1 mg/mL after 1h30min under stirring [57]. 1.5 mL of drug solution in PG at 1 mg/mL was so added in one shot to the polymeric solution, kept under stirring. 20 mL of ethanol were then added dropwise to the mixture reaching the final AmB concentration of 0.05 mg/mL. During the addition of the anti-solvent, the nanosuspension was kept under stirring at 165 rpm and maintained at 45°C. Nanoparticles, analysed by DLS after dilution (1:20), presented a hydrodynamic diameter of 178.9 nm and a PdI = 0.265.

AmB final concentration was so increased to 0.1 and 0.15 mg/mL, keeping the starting solution in PG at 1 mg/mL and increasing its volume. DLS measurements showed particles with similar characteristics to the nanosuspension at 0.05 mg/mL also at 0.1 mg/mL (132.1 nm; PdI = 0.282) and slightly increased parameters at 0.15 mg/mL (253.2 nm; PdI = 0.438).

To better investigate the process of formation of nanoparticles, the behaviour of AmB was monitored by performing UV scans in the range 200 - 500 nm (here reported in the range 300 - 500 nm for a more detailed view), that highlighted the status of AmB according to the wavelength of maximum absorbance. It has been demonstrated, in fact, that free AmB absorbs at 408 nm, while aggregate AmB at 328 nm [67][68]. UV scan of AmB in PG at 1 mg/mL presented the maximum absorbance at 408 nm *(Figure 23),* that shifted to 328 nm after the addition of water in a volume ratio PG:water of 23:77 *(Figure 24),* thus revealing the passage from a molecular to an aggregate state of AmB.

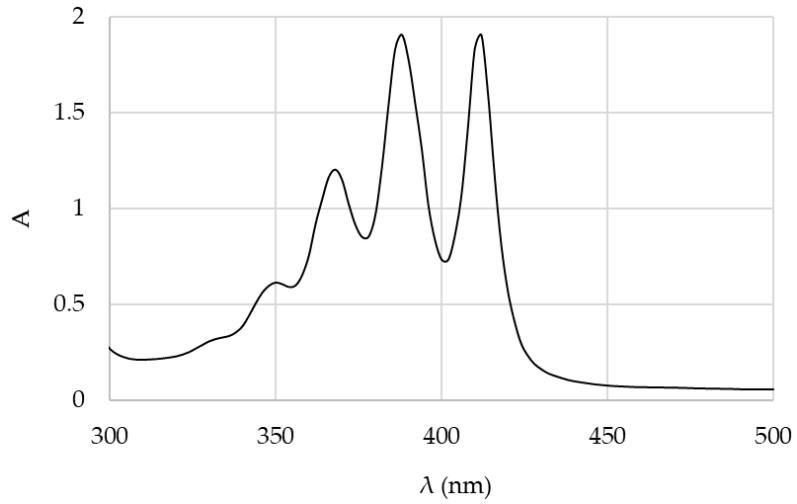

Figure 23. UV Scan of AmB in propylene glycol.

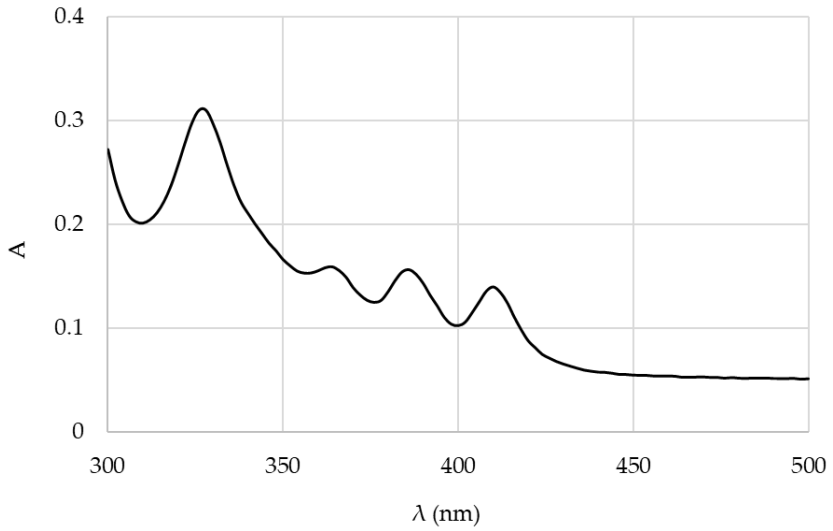

Figure 24. UV Scan of AmB in propylene glycol 23%.

This behaviour can be explained by the effect of water on the drug, that acting as anti-solvent, promotes the precipitation of AmB NP. To better investigate this process, DLS measurement was carried out on the mixture before the addition of ethanol. The result showed the formation of AmB NP with mean size of 61 nm and PdI = 0.34 *(Figure 25)*.

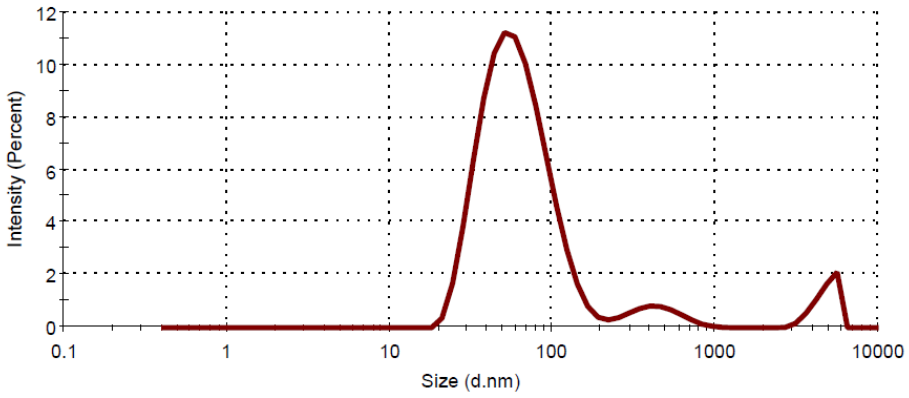

Figure 25. Size distribution of AmB NP in PG 23%.

The subsequent addition of ethanol probably promotes the precipitation of HA chains on AmB NP leading to the formation of nanocapsules, as represented in *Figure 26*.

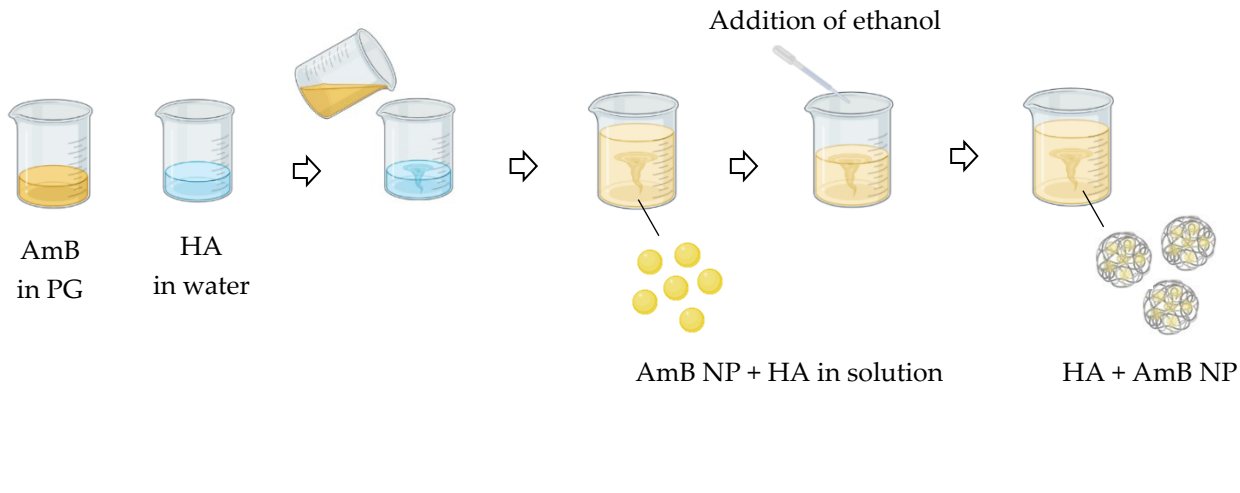

Figure 26. Graphical representation of AmB-loading into HA NP.

4.4.2 Loading of AmB into nanoparticles with different HA MW

AmB-loaded NPs were produced as previously described employing different HA MW and testing three different final concentrations of AmB, C_fAmB: 0.05, 0.1 and 0.15 mg/mL. In *Table 9* size and size distribution of obtained NP are reported for each range of HA MW.

Table 9. Size and size distribution (PdI) of blank and AmB-HA NP obtained with different HA MW. Mean size ± standard deviation (n = 3).

HA MW (kDa)	**15-30**		**50-90**		**130-300**		**750-1000**		**1000-1250**		**1500-1750**		**2000-2200**	
C_fAmB (mg/mL)	**Size (nm)**	**PdI**	**Size (nm)**	**PdI**	**Size (nm)**	**PdI**	**Size (nm)**	**PdI**	**Size (nm)**	**PdI**	**Size (nm)**	**PdI**	**Size (nm)**	**PdI**
0	482.8 ± 28.8	0.0703 ± 0.0353	121.6 ± 5.9	0.242 ± 0.009	133.4 ± 17.8	0.251 ± 0.031	47.5 ± 10.4	0.196 ± 0.085	67.6 ± 3.8	0.565 ± 0.014	47.9 ± 7.3	0.445 ± 0.020	63.4 ± 12.9	0.367 ± 0.087
0.05	461.3 ± 94.6	0.187 ± 0.041	112.5 ± 9.8	0.241 ± 0.004	320.9 ± 75.3	0.338 ± 0.073	50.5 ± 11.6	0.313 ± 0.068	462.83 ± 71.7	0.726 ± 0.011	494 ± 275.9	0.820 ± 0.081	410.1 ± 109.2	0.75 ± 0.065
0.10	514.4 ± 54.7	0.290 ± 0.138	106.3 ± 7.6	0.259 ± 0.026	151.4 ± 31.2	0.517 ± 0.044	130.8 ± 36.2	0.527 ± 0.216	666 ± 27.7	0.805 ± 0.035	800.8 ± 233.0	0.836 ± 0.185	795.3 ± 323.7	0.787 ± 0.245
0.15	628.5 ± 77.8	0.246 ± 0.047	121.6 ± 13	0.316 ± 0.081	249.9 ± 33.3	0.651 ± 0.1	410.7 ± 195.6	0.652 ± 0.162	-	-	-	-	-	-

An increase in particle size and size distribution was observed for each range of HA MW > 1000 kDa with the increase of AmB concentration. In addition, with 0.15 mg/mL of AmB, large aggregates over 1 μm were observed, even at very low ethanol concentrations, thus highlighting the strong influence of AmB concentration on size of particles obtained with HA at high MW. In contrast, for HA MW < 750 kDa, the increase of NP size was not always linear and so not dependent on AmB concentration, as it can be observed in *Figure 27*.

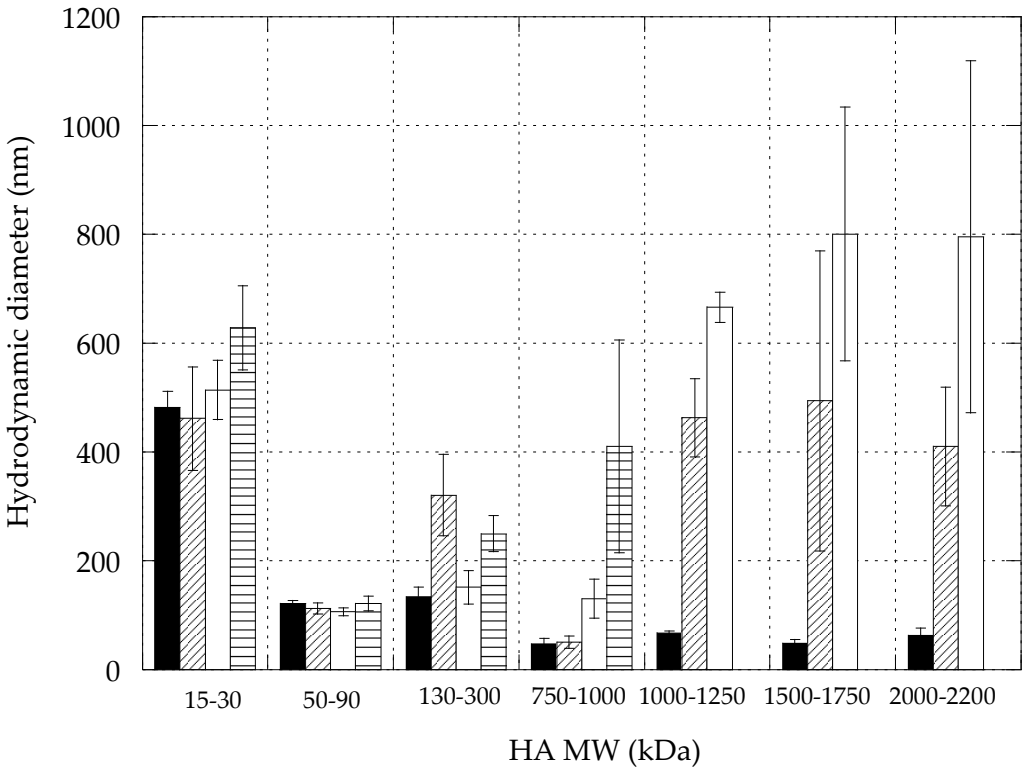

Figure 27. Hydrodynamic diameters of blank ■ and loaded HA NP with AmB at 0.05 mg/mL ▨ , 0.1 mg/mL ▤ and 0.15 mg/mL ▩ . The bars represent the standard deviation (n = 3).

The effect of AmB concentration on particle polydispersion *(Table 9)* could be due to the contribution of propylene glycol on the viscosity of the solution, whose increase (correlated to the increase of drug concentration) promoted an increase of polydispersion index of nanoparticles. In addition, this trend was more pronounced for HA MW > 1000 kDa, for which the viscosity received a significant contribution also from HA chains.

5. CONCLUSIONS

From the data presented in the present chapter, it can be concluded that the molecular weight of sodium hyaluronate plays a key role in the production of nanoparticles obtained by anti-solvent precipitation. In particular, it showed a close correlation with both the size and size distribution of nanoparticles, leading to the formation of particles with different properties according to the HA MW, higher or lower than 1000 kDa. This behaviour is probably due to a different entanglement of HA chains during the particle precipitation, leading to the formation of inter-chain H-bonds for HA MW < 1000 kDa (particle size > 200 nm) and intra-chain H-bonds for HA MW > 1000 kDa (particle size < 100 nm).

The temperature plays an important role during the process of precipitation influencing the polydispersion of particles. In particular, its increase from 25°C to 45°C led to a decrease of PdI values of particles obtained with HA MW > 1000 kDa, reducing the viscosity of the polymeric solutions and improving the interaction of polymeric chains. Together with the temperature, the volume of ethanol, employed as anti-solvent in particle precipitation, significantly affects their size. In particular, lower amount is required for HA MW < 1000 kDa compared to MW > 1000 kDa (76% and 90% v/v, respectively), probably due to the higher degree of hydration to replace, typical of sodium hyaluronate with high molecular weight. In addition, the increase of anti-solvent/solvent ratio over time positively influences the polydispersion of particles obtained with high MW (2000-2200 kDa), leading to a slightly reduction of PdI value from 0.5 to 0.35 when ethanol is added in one shot compared to when it is added drop by drop.

Finally, a method for the production of Amphotericin B-loaded HA nanoparticles was developed. AmB was first precipitated by mixing the propylene glycol drug solution with the polymeric aqueous solution. Ethanol, added dropwise, promoted the precipitation of HA onto the drug particles leading to the formation of AmB-loaded HA nanoparticles. Also in this case, the concentration of AmB presented a direct correlation with the size of nanoparticles when HA MW > 1000 kDa. In contrast, no effect was observed for HA LMW.

CHAPTER 2

HA-Amphotericin B nanoparticles for treatment of cystic fibrosis

1. INTRODUCTION

1.1 Cystic fibrosis

1.1.1 General aspects

Cystic fibrosis (CF) is an autosomal recessive disease caused by mutations in the gene encoding for the cystic fibrosis transmembrane conductance regulator (CFTR). It mainly affects the large and small airways of the respiratory system, but other organs such as pancreas, liver, GI tract can be involved. The lack or mutation of CFTR result in an alteration of the electrophysiological properties across the airway epithelia that leads to several clinical outcomes, including chronic bacterial airway infection, neutrophilic inflammation and accumulation of viscous mucus in the airways (*Figure 28*, [69]).

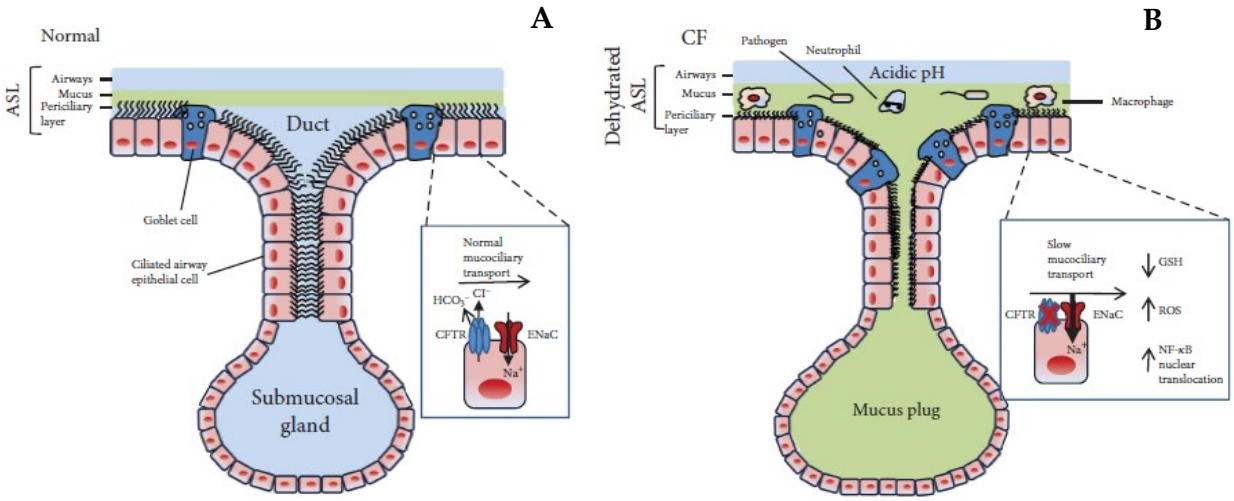

Figure 28. Physio-pathological conditions of healthy (Panel A) and CF (Panel B) lungs. Reproduced with permission from [69].

In detail, CF airways are characterized by:

- **Reduced pH**: CFTR conducts bicarbonate and the loss of CFTR eliminates bicarbonate secretion by airway epithelia, resulting in a reduced pH of the airway-surface liquid of CF patients.

- **Impaired mucociliary transport:** Mucociliary transport, involved in the trapping and removal of invading pathogens and particulates from the airways, results impaired because of the loss of CFTR anion transport and the subsequent lack of water absorption.

- **Chronic bacterial airway infection**: Failure in defence mechanisms results in chronic bacterial pulmonary infections. Species isolated are a variety of gram-positive and gram-negative organisms, including *S. aureus* and *Pseudomonas aeruginosa*. New pathogens are not only *Aspergillus* but also *Trichosporon*, *Scedosporium*, and *Exophiala*. In addition to fungal infections, CF patients also have a higher prevalence of nontuberculous mycobacterial infection, including *Mycobacterium avium complex* and *Mycobacterium abscessus complex*.

- **Chronic inflammation state:** Host-defence defect and eradication of many different types of bacteria lead to a cascade of airway inflammation and airway remodelling.

These processes directly link to the loss of CFTR function. Without CFTR-dependent chloride and bicarbonate secretions, the pH of airway-surface liquid decreases, the antibacterial activity impaired and a chronical bacterial colonization and inflammation state established [70][71].

1.1.2 Current treatments

In CF patients, antibiotics are administered to treat pulmonary infections and mucolytics are employed to improve mucus clearance from the airways, but none of them are resolving treatments. The advent of CFTR modulators has revolutionized the treatment and the life expectancy of CF patients. These molecules, in fact, target specific classes of mutations improving ion movement through the channel at the cell surface, acting on the main cause and not only by treating symptoms. Ivacaftor is the first potentiator

commercially available. In addition, correctors, including Lumacaftor and Tezacaftor, help CFTR fold properly to increase functional protein. Additional CFTR modulators are currently in different phases of clinical trials [71]. The main limitation associated with this new class of drugs is their applicability to a specific mutation. For this reason, after the introduction of the first monotherapy, association of modulators has been marketed. The most recent medicinal product is a combination of three different modulators (Ivacaftor, Elexacaftor and Tezacaftor). In addition, modulators must be taken chronically with a significant cost for the health systems.

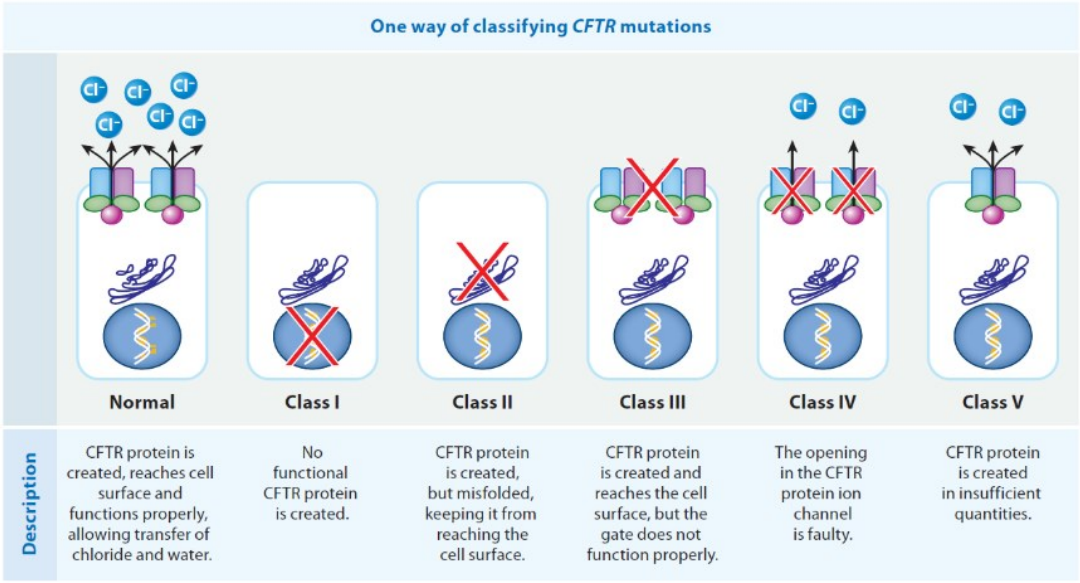

Figure 29. CFTR mutations. Modified with permission from [71].

Nearly 90% of people with CF have at least one copy of the ΔF508 mutation, but there are hundreds of CFTR mutations that result in a range of disease severities *(Figure 29)*. A CFTR gene replacement approach would be more efficacious, acting regardless of the disease-causing mutation. After the discovery of the CFTR gene in 1989, the *in vitro* proof-of-concept for gene therapy for CF was quickly established and the first gene therapy clinical trials attempted to rescue the CF defect in airway epithelia. Nowadays, there is still no FDA or EMA approved gene therapy for CF [72].

Recently, the antifungal drug Amphotericin B, usually employed for the treatment of *Aspergillus* infections in CF patients, was proposed for replacing missing or misfolded

CFTR with the same proof-of-concept of gene therapy, thanks to its ability to form ion channels [73][74].

1.2 Amphotericin B

1.2.1 Clinical applications and toxicity

AmB is one of the oldest and yet most efficient antimycotic agent belonging to the class of polyene antibiotics (*Figure 30*, [57]).

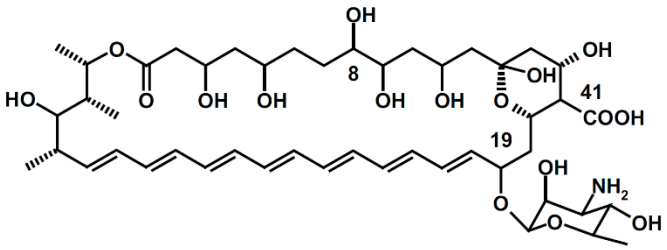

Figure 30. Chemical structure of AmB. Reproduced with permission from [57].

It is the drug of choice against fungal infection due to *Candida albicans* and *Aspergillus fumigatus* species, but it also possesses an antiparasitic activity. It is commercialized as Fungizone®, a colloidal dispersion with sodium deoxycholate, and in lipid-based formulations (Ambisome®, Amphocil® and Abelcet®) for intravenous administration. Nevertheless, the acute and sub-chronic side effects, especially related to its nephrotoxicity, suggested to investigate for new formulations, in order to deliver the drug as efficiently as possible reducing the amount of free drug in the blood and to improve its safety [57]. Liposomes, nanoemulsions, solid-lipid nanoparticles, micelles, polymeric nanoparticles and microparticles for pulmonary delivery have been proposed [75][76][77][78]. Nevertheless, no AmB nanoformulations have still reached clinical trials, probably due to their high degree of complexity.

The mechanism of action of AmB has not been uniquely identified, but it seems to be related to its interaction with ergosterol. The hydrophobic domain of AmB, in fact,

interacts with the lipid essential for the physiology of mycetes, enhancing the formation of a membrane channel *(Figure 31, Panel A)* or extracting ergosterol from the fungal membrane *(Panels B and C)* [79].

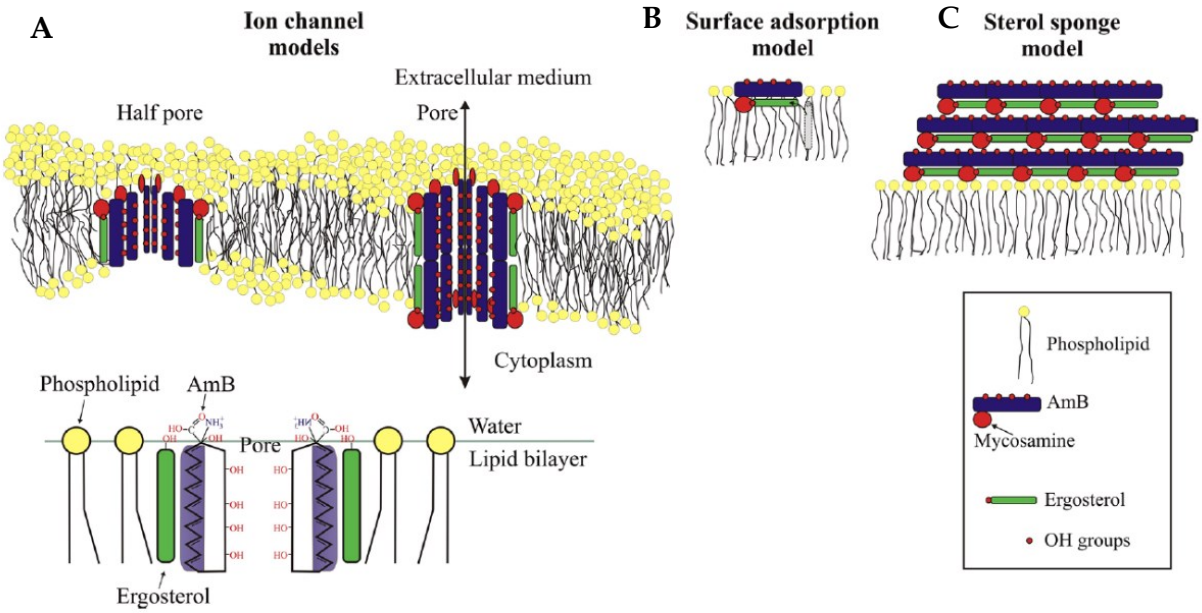

Figure 31. Mechanisms of action of AmB. Reproduced with permission from [79].

The toxicity of AmB could be related to the extraction of cholesterol from human cell membranes, leading to a destabilization of the phospholipid bilayer. The balance between the formation of channels and the extraction of sterols from cell membrane has been demonstrated to be dependent on AmB concentration. In particular, AmB at low concentration ($C_{AmB} < 5$ μM) can create channels without extracting sterols.

1.2.2 Amphotericin B for the treatment of CF

The ability of AmB to create intra-membrane pores suggested the exploitation of the drug for treating disease caused by lacking ion channel, such as cystic fibrosis. In particular, it has been demonstrated that AmB promotes HCO_3^- secretion restoring airway surface liquid pH, viscosity and antibacterial activity in primary cultures of airway epithelia [73]. The same authors recently reported the benefits of treating CF patients with AmB

(Fungizone®), by increasing transepithelial Cl^- current and hyperpolarized calculated transepithelial voltage in primary cultures of CF airway epithelia from people with two nonsense mutations [74]. Both studies represent an innovative and possible repositioning of a drug already on the market that could allow to restore host defences in cystic fibrosis airway epithelia via a mechanism that is independent of CFTR and genotype, and so valuable for all types of patients and mutations.

The co-administration of AmB with HA HMW could act against the chronic inflammation state of CF patients thanks to the anti-inflammatory effect of the polymer (Chapter 1, *paragraph 1.1.3*), together with the restoration of the anion channel.

2. AIM

The first aim of the present part of the thesis was to develop amphotericin B-loaded nanoparticles aimed to target pulmonary epithelial cells for the treatment of cystic fibrosis. Sodium hyaluronate with proper molecular weight was chosen and used for drug loading, exploiting its targeting to CD44 receptors and its possible anti-inflammatory effect on the hyper-inflamed state of CF lungs.

Secondly, powders for inhalation were obtained by spray drying AmB-HA nanosuspensions. These powders were characterized by scanning electron microscopy, laser diffraction, FT-IR and HPLC. Aerodynamic performance was investigated using a dry powder inhaler connected to impactors for aerosolization *in vitro*. Nanoparticle redispersion upon contact of the dried powders with aqueous solutions was assessed by dynamic light scattering.

Finally, preliminary *in vitro* data were collected on NCI-H441 and Calu-3 pulmonary cell lines, investigating particle cytotoxicity and particle dissolution on bronchial epithelial cells, growth at air-liquid interface to reproduce physiological conditions with mucus.

3. MATERIALS AND METHODS

3.1 MATERIALS

Sodium Hyaluronate 130-300 kDa and 750-1000 kDa were obtained from *Contipro*, Czech Republic. Amphotericin B was supplied by *Dayangchem*, China. Leucine was purchased from *A.C.E.F.* (Italy), CELDEX A-100® α-cyclodextrin from *Nihon Shokuhin Kako* (Japan) and KLEPTOSE® β-cyclodextrins from *Roquette* (France). Ultrapure water was purified by reverse osmosis with Purelab Pulse flex, *Elga-Veolia*, Italy. Cyclohexane, acetonitrile, methanol, dimethyl sulfoxide and tetrahydrofuran were of analytical grade.

3.2 METHODS

3.2.1 Preparation of AmB-loaded HA NP

AmB-loaded nanoparticles were obtained by anti-solvent precipitation using ethanol as anti-solvent. AmB was first solubilized in propylene glycol at a concentration of 1 mg/mL; HA was dissolved in water adjusted at pH = 7 with NaOH 0.1% w/v and filtered with a cellulose acetate syringe filter Minisart® 0.45 μm (*Sartorius*, Germany). The AmB solution was added in one shot to the HA solution under stirring and ethanol was then added dropwise to the mixture acting as the anti-solvent and promoting the deposition of HA chains onto AmB nanoaggregates. The process was carried out at room temperature and under stirring at 165 rpm.

The volumes of solutions, the concentrations of the components and the HA MW used are summarized in *Table 10*.

Table 10. Amount of HA, AmB and respective solvents and anti-solvent for particle production.

HA MW (kDa)	HA (% w/v)	Water (mL)	PG (mL)	Ethanol (mL)
130-300	1	5	1.5	20
750-1000	0.5	5	2.25	35

AmB NP and HA NP with propylene glycol (HA PG) were also produced with the above-described procedures, avoiding the addition of HA or AmB, respectively.

3.2.2 Dynamic Light Scattering

Size, size distribution and Z-potential of AmB-loaded nanoparticles were assessed by Dynamic Light Scattering (Zetasizer Nano ZS, *Malvern Panalytical*, UK). One mL of nanosuspension was loaded into a DTS0012 cuvette for size measurements and 0.8 mL of nanosuspension into a DTS1070 cuvette for Z-potential. Parameters were set as follow:

1. Material: RI = 1.59; Absorption = 0.010
2. Dispersant: Viscosity (25°C) = 1.3022 cP; RI = 1.354 (Ethanol mixture)
   Viscosity (25°C) = 0.8872 cP; RI = 1.33; ε = 78.5 (Water and PB)
   Viscosity (25°C) = 0.8894 cP; RI = 1.33; ε = 78.5 (NaCl 10mM)
3. Temperature = 25°C
4. Angle of detection = 173° Backscatter
5. Equilibration time = 60s
6. Number of measurements = 3

Nanosuspensions containing AmB and HA 750-1000 kDa were analysed at their actual concentration, while for AmB-HA 130-300 kDa nanosuspensions a dilution 1:20 was done before DLS measurement.

3.2.3 Addition of bulking agents to the nanosuspension before spray drying

Addition of bulking agents before spray drying is a common practice aimed to prevent the irreversible aggregation of nanoparticles and to enhance their release after inhalation [80]. For this purpose, different excipients have been proposed, most of them belonging to the class of polyols or sugars such as mannitol and lactose, but also leucine and α-cyclodextrin [81][82][83][84]. In particular, leucine has been widely employed thanks to its action as dispersion enhancer and its ability to improve the aerosol behaviour of powders influencing particle morphologies and reducing moisture sorption [85]. Nevertheless, problems related to the solubility of these excipients in ethanol/water mixture limited their choice, leading to the discard of mannitol [86] for the present application. Leucine, α- and β-cyclodextrins (α- and β-CD) were chosen for this purpose and added to the nanosuspension according to two different methods.

- **Leucine**

Solubility of leucine in ethanol/water mixtures was obtained from the article published by Boraey and colleagues, whose graph is reported in *Figure 32* [87]. The values of solubility, based on the ethanol fraction in ethanol/water mixtures in the range of interest for the present application, were extrapolated and summarized in *Table 11*.

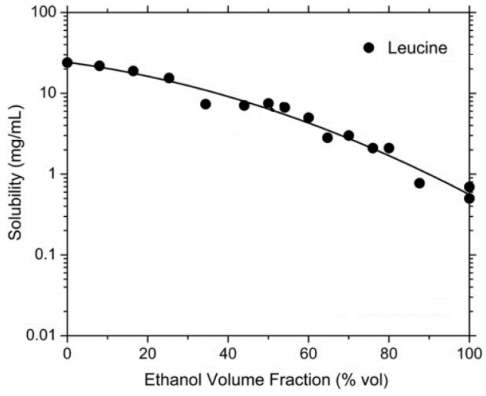

Figure 32. Leucine solubility in ethanol/water mixtures. Modified with permission from [87].

Table 11. Leucine solubility in ethanol/water mixtures in the range 75-95% v/v of ethanol, extrapolated from Figure 32 [87].

Ethanol %	Solubility (mg/mL)
75	2.15
80	1.67
85	1.33
90	0.982
95	0.744

Based on data reported in *Table 11*, leucine was added to the nanosuspension at a concentration of 0.97 mg/mL, with a NP/leucine ratio of 1:1.5 w/w. The nanosuspension was kept under stirring in dark conditions for 3 days before spray drying, to allow the complete dissolution of leucine *(Figure 33)*.

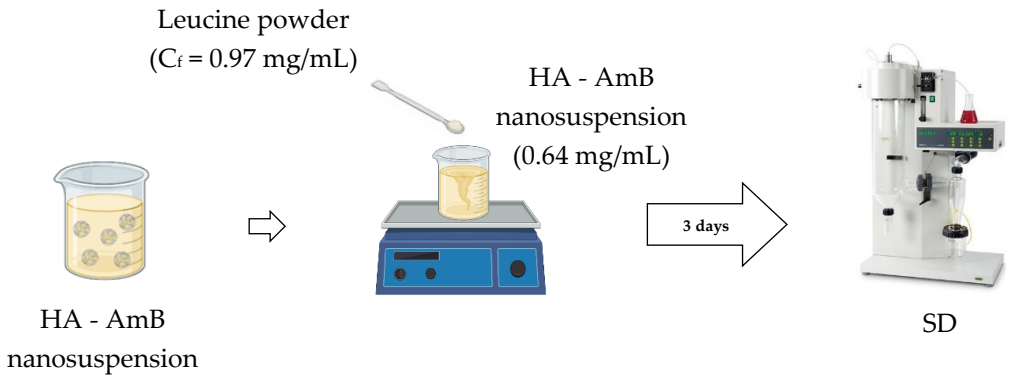

Figure 33. Method of the addition of leucine to the nanosuspension.

- **α- and β-cyclodextrins**

In literature, the solubility of β-cyclodextrin in water/ethanol mixtures has been demonstrated to be dependent on the fraction of the components *(Figure 34)*. Nevertheless, after its addition to the nanosuspension (water 12%, ethanol 83% and PG 5% v/v), β-cyclodextrin did not dissolve within three days under stirring, even at lower concentration (0.064% w/v) compared to the one reported in literature [88], probably due to the presence of other components in suspension.

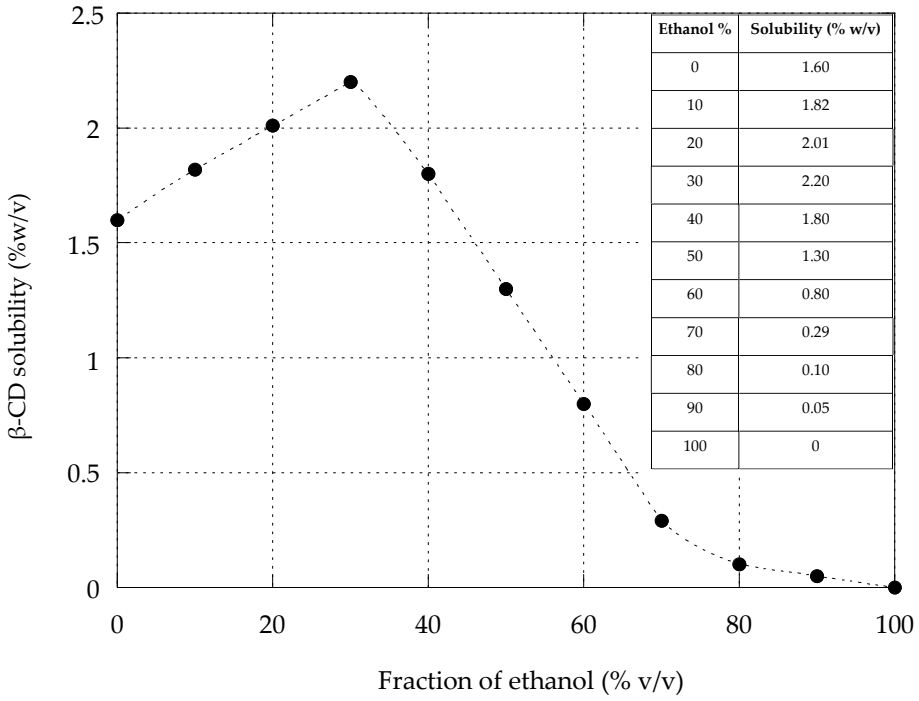

Ethanol %	Solubility (% w/v)
0	1.60
10	1.82
20	2.01
30	2.20
40	1.80
50	1.30
60	0.80
70	0.29
80	0.10
90	0.05
100	0

Figure 34. Solubility of β-CD in ethanol/water mixtures. Modified with permission from [88].

For this reason, β-CD was first dissolved in water (solubility 18.5 mg/mL) and then added to the nanosuspension. α-CD was added with the same method. In particular, α-CD, that presents a higher water solubility (145 mg/mL), was dissolved in 7.2 mL of ultrapure water at a concentration of 75.7 mg/mL and then added to the nanosuspension reaching a NP/α-CD ratio of 1:5. β-CD was dissolved in 7.2 mL of ultrapure water at a concentration of 15 mg/mL and then added to the nanosuspension reaching a NP/β-CD ratio of 1:1. The nanosuspensions were kept under stirring during the addition of the excipients, and then immediately spray dried *(Figure 35)*.

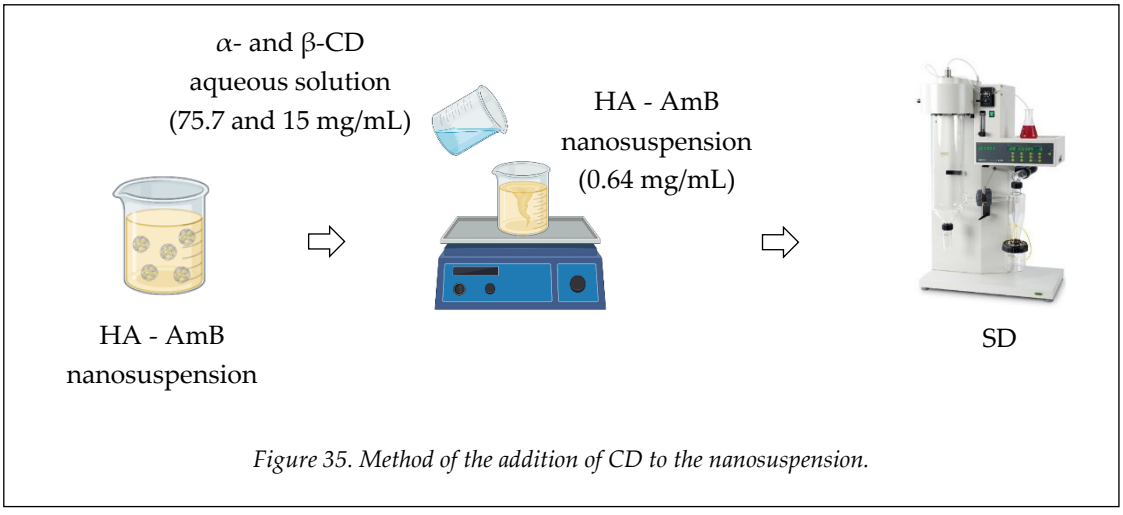

Figure 35. Method of the addition of CD to the nanosuspension.

3.2.4 Spray Drying

To obtain dry powders for inhalation, nanosuspensions were dried using a Mini Spray Dryer B-290 (*Buchi*, Switzerland) connected with an Inert loop B-295 for organic solvent condensation. Nitrogen was used a nebulizing gas and the process was carried out at the following conditions:

1. Needle diameter = 0.7 mm
2. T_{inlet} = 80° C (T_{outlet} recorded = 56°C)
3. Aspiration = 35 m^3/h (100%) - HA 130-300 kDa; 32 m^3/h (80%) - HA 750-1000 kDa
4. Nitrogen flux = 473 L/h (40 mm)
5. Feed rate = 2 mL/min (7%)
6. T_{cond} = 10° C

The yield % of the process was calculated according to the following equation:

$$\text{Yield \%} = \frac{\text{Collected dry mass}}{\text{Solute mass}} \times 100 \qquad \textit{(Eq. 5)}$$

3.2.5 Differential Scanning Calorimetry

A DSC 821e (*Mettler Toledo*, Switzerland) driven by STARe software (*Mettler Toledo*) was employed to investigate the thermal behaviour of AmB in the range between 25 - 150°C at the heating rate of 10°C/min. A sample of about 4 mg was placed in a 40 µL aluminium pan with a pierced cover and heated under a flux of dry nitrogen (100 mL/min).

3.2.6 Laser Diffraction

Particle size distribution of powders was measured by laser diffraction (*Spraytec, Malvern*, UK). Powders were suspended in cyclohexane at a concentration of 1 mg/mL with the

addition of 0.1% w/v SPAN 85 and then sonicated for two minutes to improve the homogeneity of the suspension.

Measurements were carried out with an obscuration level between 8 - 10% at the following conditions:

1. Path Length: 2.7 mm
2. Particulate RI = 1.50 + 0.500i
3. Dispersant RI = 1.43

Data were expressed in terms of volume-weighted diameter (D_v) for 10^{th}, 50^{th} and 90^{th} percentiles of the distribution, corresponding to $D_v(10)$, $D_v(50)$, and $D_v(90)$ respectively.

3.2.7 Scanning Electron Microscopy

The morphology of the powders obtained by spray drying was analysed by scanning electron microscopy (SEM) using a FESEM SUPRA™ 40 microscope (*Carl Zeiss*, Germany). Each powder sample was deposited on adhesive black carbon tabs pre-mounted on aluminium stubs to allow the dispersion of the charge and coated with a gold film of about 60 nm. The particles in excess were gently removed with a nitrogen flow. The samples were analysed under high vacuum conditions (1.33×10^{-2} Pa for 30 min) and the images were collected at different magnifications (5k, 7.4k, 10k and 20k X) using an accelerating voltage of 1 kV.

3.2.8 Fourier-Transform Infrared Spectroscopy

The presence of new bonds between the drug and the polymer after the formation of the particles was assessed in the powders by Fourier-Transform Infrared Spectroscopy (FT-IR). An Agilent Cary 630 (*Agilent,* USA) was employed for this purpose at the following set parameters:

1. Clean scan: 4
2. Threshold: 0.002
3. Y-axis units: Transmittance
4. Clamp max y value: 2 Abs
5. Minimum y threshold: 1^{-5}

Acquired spectra were analysed using MicroLab® software.

3.2.9 High Pressure Liquid Chromatography: drug content and drug loading

AmB content in the powders and the amount of drug loaded in the nanoparticles was assessed by liquid chromatography using an HPLC Agilent 1200 (*Agilent,* USA). The method was set basing on the one proposed by Y. Chang and colleagues [89]:

1. Column = Supelcosil LC-18, C_{18}, 250 mm x 4.6 mm, 5μm
2. Flux rate = 1 mL/min
3. Temperature = 30 °C
4. Injection volume = 20 μL
5. Detection λ = 383 nm
6. t_{run} = 35 minutes (t_{rit} = 23 minutes)
7. Mobile phase = 55% v/v Organic phase (Methanol 60%, Acetonitrile 26%, Tetrahydrofuran 14%); 45% v/v Aqueous phase (Ultrapure water with EDTA 2.5 mmol/L)

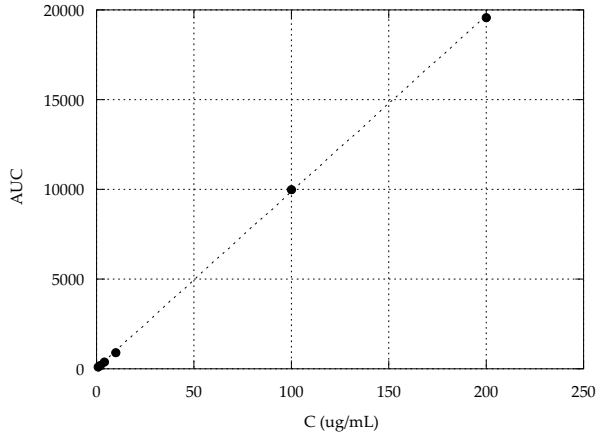

Figure 36. Calibration curve of AmB in DMSO: y = -2.2361 + 98.313x, R^2 = 0.99988.

The analytical method was assessed in terms of linearity of response (Area Under the Curve, AUC, of the peak at 23 minutes *vs* concentration) in the concentration range 1 - 200 μg/mL *(Figure 36)*. Limit of Quantification (LOQ) and Limit of Detection (LOD), calculated as reported in *paragraph 3.2.3* (Chapter 1, *Eq. 2-3)*, were LOQ = 0.151 μg/mL and LOD = 0.0498 μg/mL.

- **Drug content %**

To quantify the drug content in the powders, a predefined amount of powder was dissolved in 1.5 mL of mobile phase to reach a theoretical concentration of AmB amounting to 110 μg/mL. The solution was left under stirring at least for 2h to obtain the complete dissolution of both AmB and sodium hyaluronate and then analysed by HPLC to quantify the total amount of drug in the powder sample.

- **Encapsulation efficiency % (EE%)**

To quantify the amount of AmB loaded in the nanoparticles, 10 mg of powder were suspended in 1.5 mL of DMSO (C = 6.67 mg/mL) and then filtered with polytetrafluoroethylene syringe filters Minisart® 0.20 μm (*Sartorius*, Germany). DLS measurements were then performed to verify the elimination of nanoparticles from the filtrate before injection in HPLC. The amount of encapsulated drug was quantified indirectly according to the following equation:

$$EE\% = \frac{AmB_{tot} - AmB_{free}}{AmB_{tot}} \times 100 \qquad (Eq.\ 6)$$

where AmB_{tot} is the drug content in the powder determined as previously described, and AmB_{free} is the amount of drug found in solution after filtration and quantified by HPLC.

3.2.10 Powder redispersions

Powders containing HA 130-300 kDa and AmB were dissolved at 0.5, 0.75, 1 and 1.5 mg/mL in ultrapure water and in phosphate buffer pH = 6.15, prepared according to the European Pharmacopeia (6.8 g NaH_2PO_4 in 1000 mL of water and adjusted to pH = 6.15 with NaOH 0.1% w/v). DLS analysis were then performed according to *paragraph 3.2.2*.

Powders containing HA 750-1000 kDa and AmB were dissolved in NaCl 10 mM, obtained by diluting a 0.9% w/v sodium chloride solution (*Fresenius Kabi*, Italy). Powder suspensions at 0.5 and 1 mg/mL were tested and analysed by DLS after 0, 5, 15, 30 and 60 minutes of sonication.

3.2.11 In vitro aerosolization

Aerodynamic properties of the dry powders were assessed *in vitro.* 10 mg of powder were loaded into a V-Caps® (*Capsugel*, Switzerland), size 3, and then located in a RS01® inhaler (*Plastiape*, Italy). The device was connected using a rubber adaptor to a Fast-Screening Impactor (FSI) (*Coplay scientific*, UK), composed by an induction port (IP), a course fraction collector (CFC) and a fine fraction collector (FFC). The aerosolization was carried out for 4s with an air flow of 60 L/min. The amount of powder remaining in the capsule and in the device (Cps + Dev), the course powder deposited in the IP, in the rubber adaptor and in the CFC (IP+CFC), and the fine powder reaching the FFC (FPD) were determined by weight difference before and after aerosolization.

The emitted dose (ED) was obtained by subtracting the amount of powder found in the capsule and in the device from the loaded one. The emitted fraction (EF%) was then calculated as the percentage of the ED on the total amount of loaded powder. The fine particle fraction (FPF%) was finally calculated as the percentage of the Fine Particle Dose, FPD, the amount of powder with an aerodynamic diameter lower than 5 μm found in the FFC, on the ED.

3.2.12 Cell culture

The human distal lung epithelial cell line NCI-H441 (ATCC HTB-174) was purchased from LGC *Promochem* (UK) and used at the passages 65 - 78. Cells were cultured in Gibco RPMI Medium 1640 1X (*Biosciences*, Ireland) supplemented with 5% Fetal Bovine Serum (FBS; *Sigma-Aldrich*, Ireland) and 1% Sodium Pyruvate (solution 100 mM; *Sigma-Aldrich*, Ireland). Cells were growth in 75 cm^2 flasks Cellstar® (*Greiner BioOne*, Germany) and maintained in a humidified atmosphere at 37°C and 5% CO_2 with media changes every 2/3 days.

Calu-3 cells (passage 23 - 33) were cultured in Gibco Advanced MEM 1X (Reduced serum medium; *Thermo Fisher Scientific*, Ireland) supplemented with 2% Gibco GlutaMAX® (L-Glutamine 100X; *Thermo Fisher Scientific*, Ireland) and 5% FBS, according to the method proposed by Kreft and colleagues [90][91]. Cells were growth in flasks Cellstar® 75 cm^2 (*Greiner BioOne*, Germany) and maintained in a humidified atmosphere at 37°C and 5% CO_2 with media changes every 2/3 days.

Both cell lines were passaged when reaching 80 - 90% confluency, washed with Dulbecco's Phosphate Buffered Saline (PBS, 10 mM phosphate buffer, 2.7 mM potassium chloride and 0.137 M sodium chloride; *Sigma-Aldrich*, Ireland) and detached with Trypsin 1X (Trypsin/EDTA; *Sigma Aldrich*, Ireland) for 10 minutes at 37°C.

3.2.13 Cytotoxicity (Alamar-Blue assay)

Alamar-Blue assay is a cytotoxicity assay based on the detection of resorufin, a fluorescent substance that results from the reduction of resazurin by viable cells [92]. For this study, H441 and Calu-3 cells were seeded in 96-well Corning® plates (*Thermo Fisher Scientific*, Ireland) at a density of 16500 cells/well and 15000 cells/well, respectively, in 200 μL of complete media. Cells were incubated at 37°C in 5% CO_2 atmosphere for a week, changing the medium every two days. At 8^{th} day, the medium was replaced with 200 μL of FBS-free

medium to stop the cell growth and to allow cell differentiation. The day after, the medium was removed and cells were treated with AmB raw material (at concentrations 0.125, 0.25, 0.5, 1, 5, 10, 50 and 100 μg/mL) and spray dried powders (AmB at concentrations 1, 5, 10, 50 μg/mL) dispersed in FBS-free medium, 200 μL per well. Cells treated with medium alone were used as positive control. After 4h and 24h of incubation the samples were removed, the cells were washed with 100 μL FBS-free medium and 100 μL of Alamar Blue 10% in FBS-free medium was added to each well. Cells were incubated for 3h at 37°C in 5% CO_2 atmosphere and the fluorescence intensity was read using FLUOstar Optima plate reader (*BMG Labtech*, Germany) equipped with Optima® Software. Excitation and emission wavelength were set at 544 nm and 590 nm, respectively (Gain = 1250). Cell viability% was calculated as follow:

$$\text{Cell viability \%} = \frac{F_{sample} - F_{blank}}{F_{control} - F_{blank}} \times 100 \qquad (Eq.\ 7)$$

where F_{sample} is the fluorescence of the tested sample, F_{blank} is the fluorescence of medium alone and $F_{control}$ the fluorescence of positive control. Alamar Blue alone was employed as negative control.

3.2.14 Culture at air-liquid interface

For the growth of Calu-3 cell line at air-liquid interface (ALI), cells were cultured on Transwell Clear® inserts (Corning 3460®, 12 mm in diameter, 0.4 μm pore size; *Thermo Fisher Scientific,* Ireland) in a 12-wells Corning® plate (*Thermo Fisher Scientific*, Ireland). On day -1, rat-tail collagen type I (*Thermo Fisher Scientific*, Ireland) was added into each insert at 25 μg/cm² after dilution with FBS-free medium (described in *paragraph 3.2.10*), 500 μL per well. On day 0, medium was removed from the apical side, and collagen was let wetting for some minutes in sterile conditions. Medium containing FBS was supplemented with 1% Insulin-Transferrin-Sodium selenite (ITS premix universal culture supplement; *Thermo Fisher Scientific*, Ireland) and 1 μM Dexamethasone (*Sigma-Aldrich*, Ireland) to improve cell growth and the formation of tight junction, respectively [93]. Cells were then

seeded at a density of 5 x 10^5 cells/cm^2 adding 170 µL in the apical side, while 700 µL of medium were added in the basolateral side. On day 1, it was replaced with 700 µL of fresh medium, while medium in the apical side was removed to let cells growing in ALI conditions. From day 3, medium was changed daily until formation of a confluent monolayer.

For TEER measurements, 800 µL and 500 µL medium were added in the basolateral and apical side, respectively. Cells were let stabilizing at 37°C in 5% CO_2 atmosphere for ten minutes and TEER values were recorded using a Millicell® ERS-2 Epithelial Volt-Ohm Meter (*Millipore,* USA). Cells were employed for experiments when presenting TEER values between 900 - 1000 $cm^2 \cdot \Omega$.

3.2.15 Assessment of particle deaggregation by light microscopy

Particle deaggregation was assessed using an Olympus IX81 light microscope and recorded with the OLYMPUS Cell Sens Dimension software. A small amount of powder was loaded with a spatula into the mouthpiece of a needle, which fits over the syringe tip, and then attached to a 1 mL syringe. Particles were then aerosolized on the monolayer of Calu-3 cells cultured at ALI and their redispersion was followed over time (until 90 or 120s), observing the complete release of nanoparticles not detectable by light microscopy.

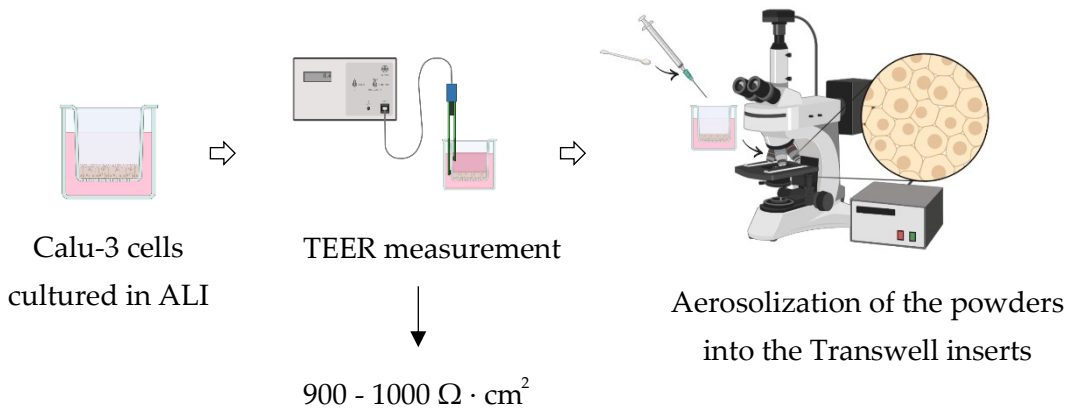

Figure 37. Experimental steps for the assessment of particle dissolution in vitro.

4. RESULTS AND DISCUSSION

4.1 Nanoparticles containing AmB and HA 130-300 kDa

4.1.1 Dynamic Light Scattering

HA, HA (PG), AmB and AmB-loaded nanoparticles with HA 130-300 kDa were obtained according to the method developed and described in Chapter 1, and then summarized in *paragraph 3.2.1* of Chapter 2. Nevertheless, to obtain dry powders for inhalation by spray drying, it was necessary to increase the volume of the nanosuspensions because of their low mass content (C_f < 2 mg/mL, V_f = 26.5 mL). For this reason, the volume was tripled, starting from 15 mL of polymeric aqueous solution and keeping the solvent/anti-solvent ratio previously established for 5 mL. In case of AmB NP, the volume was further increased because of the low drug concentration (0.05 mg/mL), thus starting from 100 mL of aqueous solution.

The increase of the volume led to the formation of nanoparticles with size and size distribution reported in *Table 12*.

Table 12. Size and size distribution (PdI) of obtained HA, HA (PG), HA + AmB and AmB NP at increased volumes.

Sample	**HA**	**HA (PG)**	**HA + AmB**	**AmB**
Size (nm)	150.6	247.9	-	936.3
PdI	0.47	0.245	-	0.435

In case of HA + AmB nanosuspension, the increase of volume led to the precipitation of bigger aggregates and white particles visible to the naked eye. The effect was probably due to the change of the macro-, meso- and micro-mixing, that led to different polymer-polymer, drug-polymer as well as antisolvent-polymer interactions, with the obtainment of large aggregates instead of nanoparticles.

For this reason, three different batches of HA + AmB nanosuspension at low volume (26.5 mL) were prepared and spray dried in sequence (Size ~ 300 nm and PdI = 0.3).

This method was then discarded because of the problems related to the increase of the scale of production.

4.1.2 Spray drying and powder characterization

To select the most proper temperature for spray drying, the melting point of AmB was first assessed. For this purpose, an analysis by DSC was carried out on AmB raw material investigating thermal events in the range of 25 - 150°C. The endothermal peak, reported in *Figure 38*, showed an onset temperature at around 85°C and the peak at 105°C.

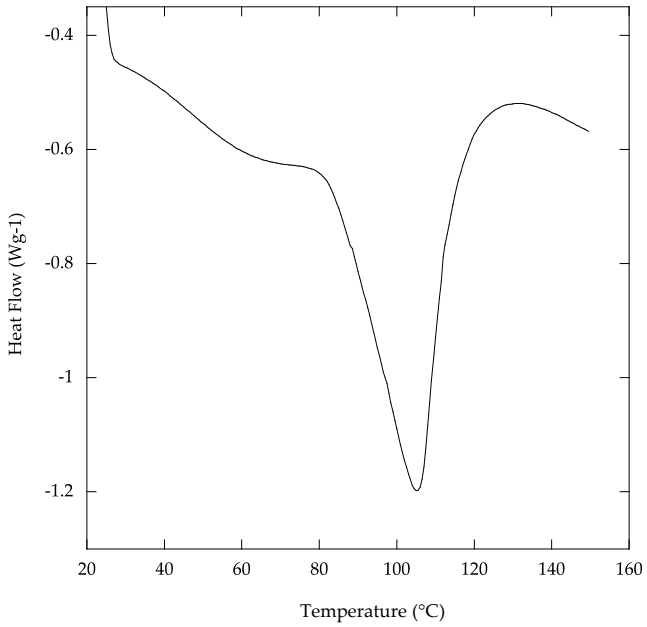

Figure 38. DSC analysis on AmB raw material.

The evaporation temperature of the solvents was then assessed, considering the percentage of each component in the mixture: 19% v/v water, 75% v/v ethanol and 6% v/v propylene glycol. Water, ethanol and propylene glycol have a boiling point at 100°C, 78.4°C and 188°C, respectively. Nevertheless, mixtures of these solvents present lower evaporation temperature depending on the fraction of each one as reported in *Figures 39* and *40* [94][95].

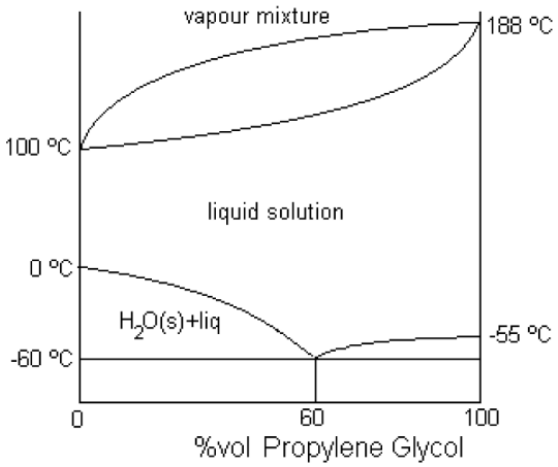

Figure 39. Phase diagram of PG/water mixture. Reproduced with permission from [87].

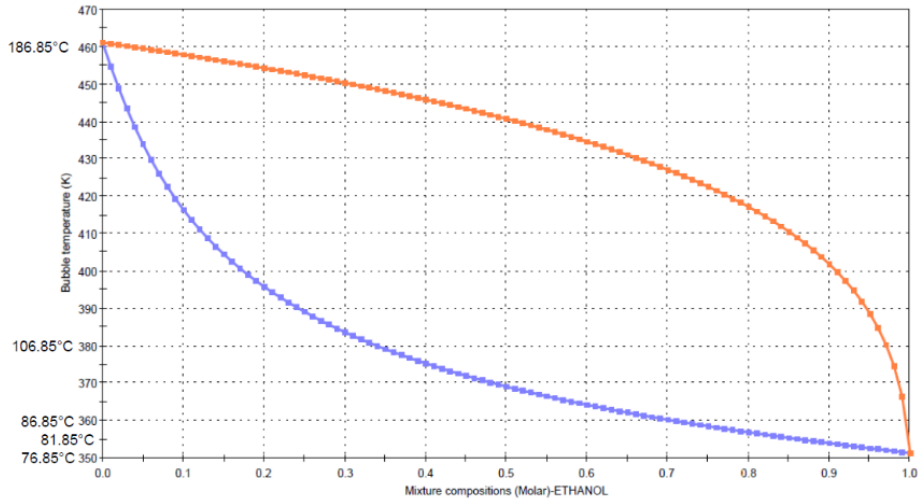

Figure 40. Phase diagram of PG/ethanol mixture. Reproduced with permission from [88].

Based on these data, considering the fraction of each solvent and the onset temperature of melting of AmB, the temperature for spray drying was fixed at 80°C.

The yields % of the process, calculated as described in *paragraph 3.2.4 (Eq. 5)*, are reported in *Table 13*. The values highlighted the role of sodium hyaluronate during spray drying in increasing the amount of powder collected at the end of the process compared to the powder containing only AmB.

Table 13. Yield% of spray drying process of nanosuspensions.

Nanosuspension	Yield %
HA - AmB	69
HA	67
HA (PG)	57
AmB	37

This result could be due first to the concentration of the nanosuspensions, that plays an important role in the yield of the process of SD. HA-containing nanosuspensions, in fact, presented higher concentrations (C > 1.8 mg/mL) compared to the one containing only AmB (C = 0.05 mg/mL), positively influencing the final yield of the process. In addition, the entrapping effect of the polymer on AmB molecules or nanoparticles, enhancing their aggregation forming HA-AmB microparticles, could avoid the loss of smaller AmB particles due to the aspiration effect of the spray drier.

Powder obtained by spray drying were then analysed by laser diffraction. Analyses were carried out on blank microparticles obtained from water/ethanol *(Figure 41)* and water/ethanol/PG *(Figure 42)* mixtures as well as on AmB-loaded HA microparticles *(Figure 43).*

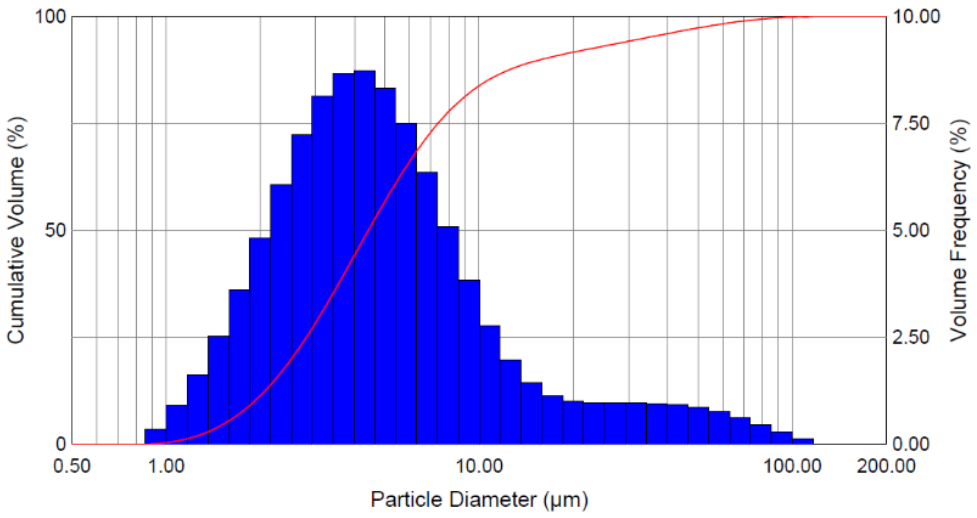

Figure 41. Frequency and cumulative size distribution of HA powder (obtained from water/ethanol mixture).

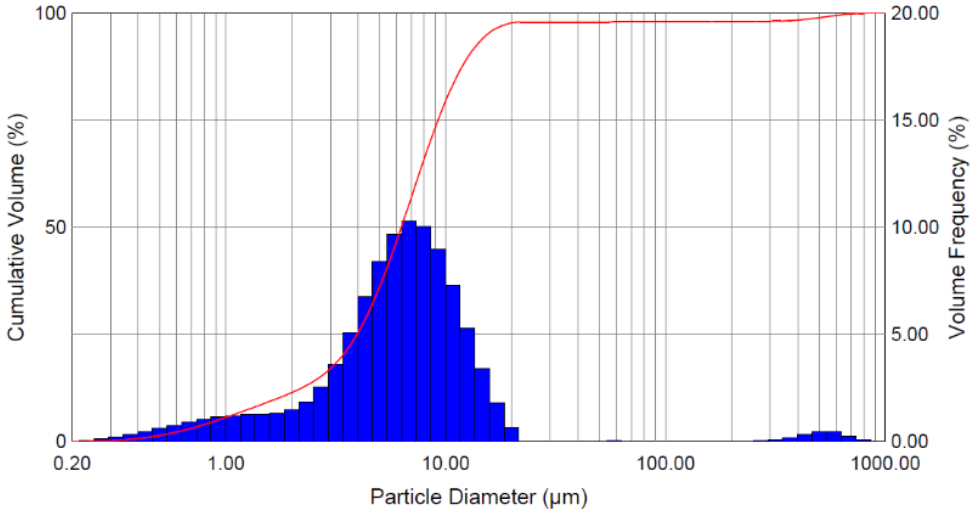

Figure 42. Frequency and cumulative size distribution of HA powder (obtained from water/ethanol/PG mixture).

As it can be observed in *Figures 42* and *43*, size distribution of powders obtained by water/ethanol/PG mixture containing blank and AmB-loaded particles presented a higher $D_v(50)$ characterized by the presence of a small tail at lower sizes. In contrast, HA powder distribution reported in *Figure 41*, displayed the main peak below 10 µm and a smaller tail at higher values. The peak around 500 - 600 nm in the HA powder size distribution *(Figure 42)* could be ascribed to the presence of a small population of particle aggregates.

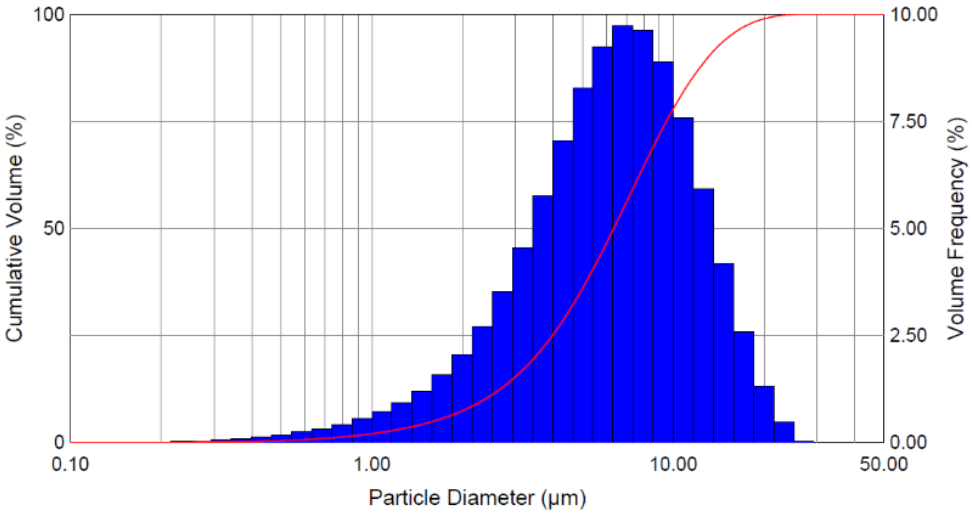

Figure 43. Frequency and cumulative size distribution of HA + AmB powder.

D_v values of all powders are summarized in *Table 14*. Powders obtained by water/ethanol/PG mixture (blank and AmB-loaded microparticles) presented quite higher

volume-weighted diameters compared to the one obtained by water/ethanol mixture, presenting a $D_v(50) < 5$ μm. On the contrary, no differences between blank and AmB-loaded microparticles were observed, highlighting that PG but not AmB influences size of microparticles obtained by spray drying.

Table 14. Volume-weighted diameters of HA nano-embedded microparticles (μm).

	$D_v(10)$	**$D_v(50)$**	**$D_v(90)$**
HA	1.88	4.37	15.17
HA (PG)	1.7	6.29	12.73
HA + AmB	2.36	6.35	13.05

These results suggest the important role of PG during spray drying, although it evaporates, and it is not found in the powder collected at the end of the process. For this reason, deeper information about microparticles were sought by scanning electron microscopy.

SEM acquisitions revealed the strong influence of PG on particle morphology in addition to their particle size. HA blank microparticles obtained from water/ethanol mixture, in fact, presented a quite spherical shape with a smooth surface *(Figure 44)*.

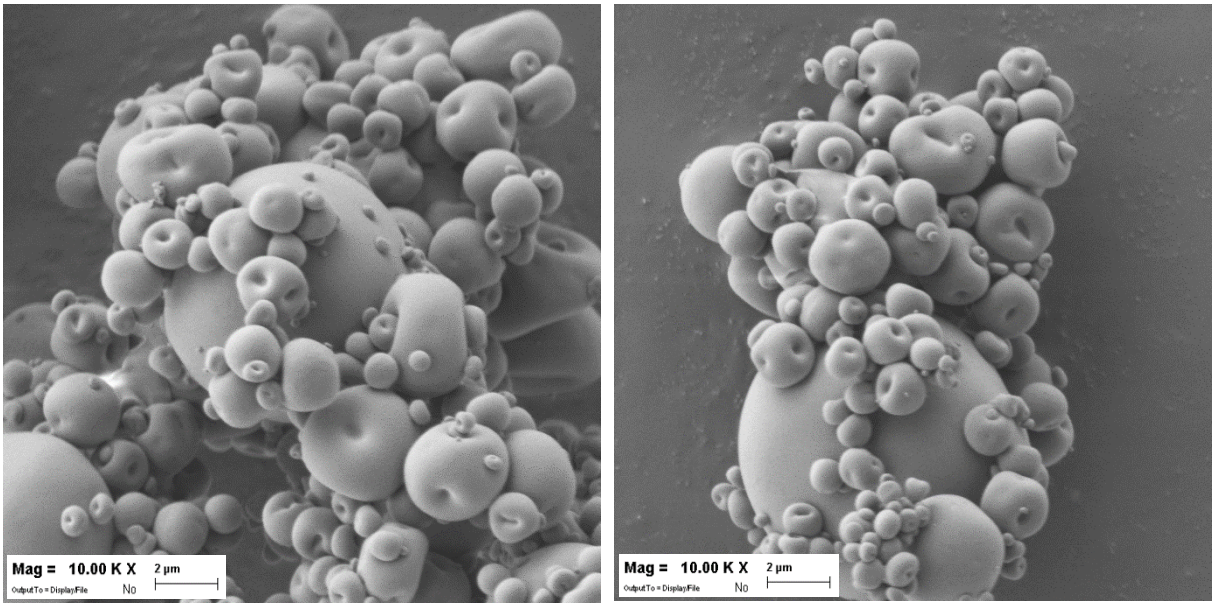

Figure 44. Morphology of SD powder containing HA NP (obtained from a water/ethanol mixture).

In contrast, HA blank microparticles obtained from water/ethanol/PG mixture displayed collapsed and concave shapes *(Figure 45)*, even if both powders (depicted in *Figures 44* and *45*) contain only HA and were produced with the same spray drying process parameters.

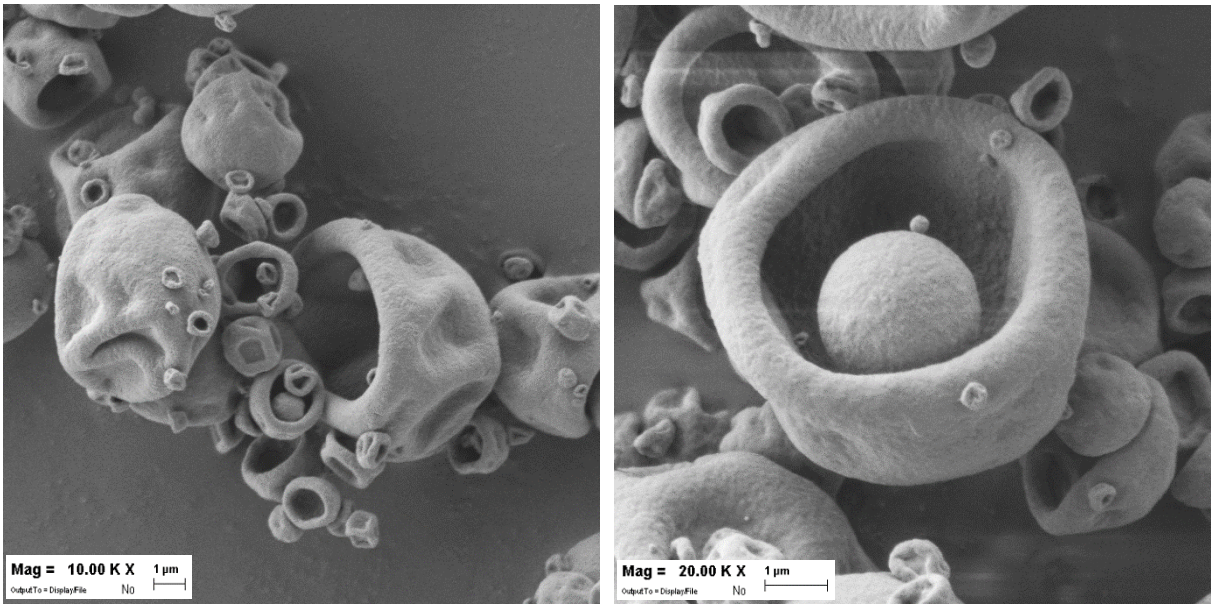

Figure 45. Morphology of SD powder containing HA NP (obtained from a water/ethanol/propylene glycol mixture).

This effect could be explained by the increase of viscosity of the nanosuspension due to the presence of PG, even if in small concentration, that influences the driving forces during the evaporation impairing the separation of components and therefore modifying the final morphology of particles. The process of spray drying, in fact, is based on a balance between heat and mass transport, in which the rate of evaporation is determined by the energy required to vaporize the solvent and the energy transported to the surface of the droplet [96].

When the diffusional motion of the solutes is fast compared to the radial velocity of the retreating droplet surface (Peclet numbers < 1), in absence of other driving forces the solutes remain fairly evenly distributed in the droplet during the evaporation and the surface enrichment is small [96]. It is the case of HA microparticles obtained by water/ethanol mixture, that present spherical shapes.

On the contrary, if the surface moves faster than the suspended components (Peclet numbers > 1), the surface becomes enriched of components. The resulting particles can have a range of different morphologies, depending on their size and the properties of their shells in the final stages of the drying process. Solid hollow spheres can be formed, but if the shell does not become rigid quickly, it can buckle or fold forming wrinkled particles, such as in case of HA microparticles obtained by water/ethanol/PG mixture. Similar morphology was observed for powder containing AmB-loaded NP, with concave surface and folded particles among some bigger and spherical ones *(Figure 46)*.

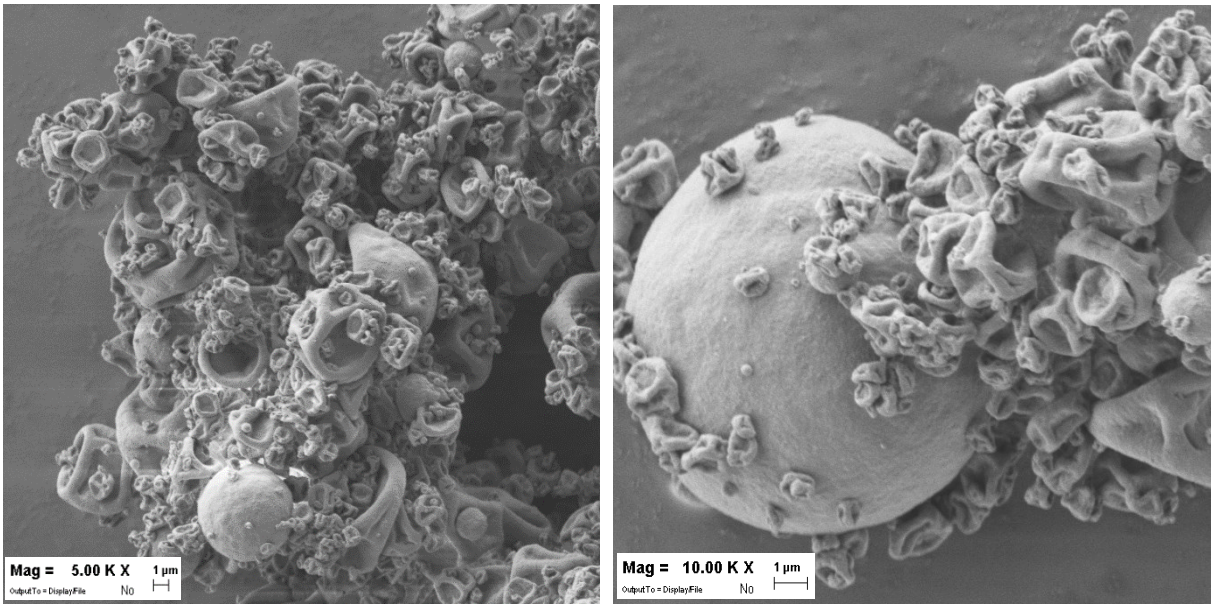

Figure 46. Morphology of SD powder containing HA + AmB NP.

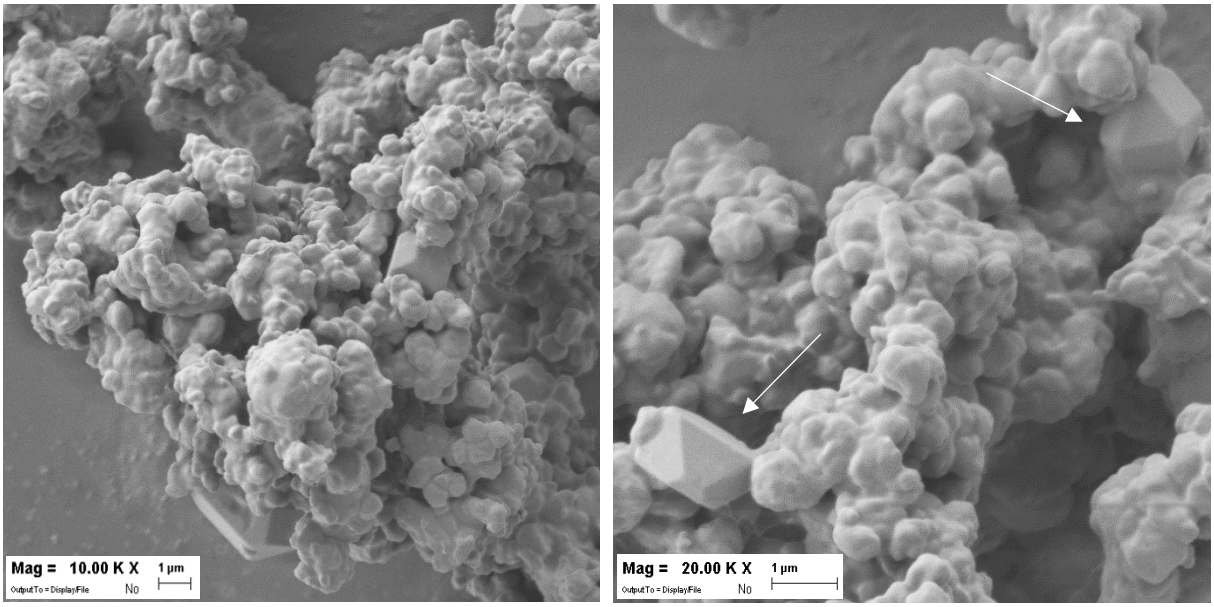

Figure 47. Morphology of SD powder containing AmB NP.

Powder containing AmB NP presented a completely different morphology, characterized by fused aggregates and by the presence of isolated crystals (white arrows, *Figure 47*). Its different morphology, compared to the powder containing AmB + HA NP, may suggest the successful loading/embedding of the drug into the polymeric nanoparticles.

4.1.3 Aerodynamic performance

The aerodynamic performance of the powders was assessed *in vitro* using a Fast-Screening Impactor (FSI). The powder distribution after aerosolization of 10 mg was then assessed by weight difference and reported in *Table 15*.

Table 15. Powder distribution in FSI and derived EF% and FPF% values. Mean ± standard deviation (n = 2).

Powder	Cps + Dev (mg)	IP + CFC (mg)	FPD (mg)	EF%	FPF%
HA	0.30 ± 0.01	8.75 ± 0.67	1 ± 0.71	97 ± 0.002	10.2 ± 7.21
HA (PG)	0.08 ± 0.09	7.73 ± 0.39	2.3 ± 0.5	99.2 ± 0.84	22.9 ± 4.8
HA + AmB	0.16 ± 0.22	8.37 ± 0.77	1.5 ± 0.57	98.4 ± 2.2	15.3 ± 6.1

All samples presented a high amount of powder in the IP and in the CFC, where more than 7.5 mg of the loaded powders deposited. In contrast, a lower amount reached the FFC, where less than 2.5 mg were found.

All the powders presented similar behaviour. Nevertheless, the distribution of the powder in the FSI revealed a better aerodynamic performance for powders with collapsed morphology (HA PG and HA + AmB), probably due to the lower density of particles that decreases their aerodynamic diameter (Chapter 1, *paragraph 1.2.3*). The presence of AmB seems to slightly affect the performance of the powder reducing the FPF% from 22% to 15% (w/w).

4.1.4 Powder redispersion in phosphate buffer pH 6.15 and water

Particles containing HA-AmB were redispersed at different concentrations reported in *Table 16*, simulating the administration of 10 mg and 20 mg of powder with a DPI. The concentrations were calculated basing on the volume of lung fluid in the conductive airways (CA) and in the alveolar region (AR), amounting to mean values of 20 mL and 13 mL, respectively [50].

Table 16. Theoretical powder concentration in the lung fluid after administration of 10 and 20 mg of powder.

	10 mg	**20 mg**
C_{CA} (mg/mL)	0.5	1
C_{AR} (mg/mL)	0.74	1.5

Particle size, assessed by DLS, presented quite similar values ranging from 500 nm to 600 nm at the tested concentrations [0.5 - 1.5 mg/mL] *(Figure 48)*.

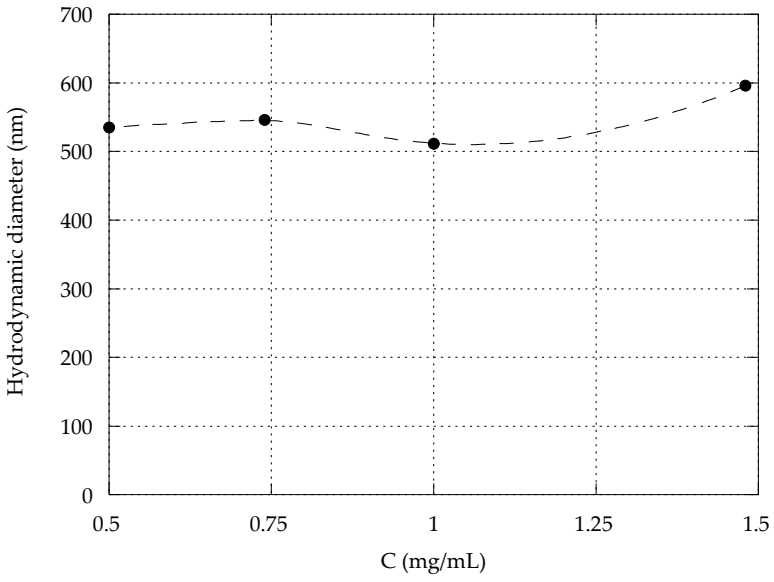

Figure 48. Hydrodynamic diameter of released nanoparticles in PB (pH = 6.15) at different concentrations.

Size of nanoparticles resulted in almost 2-folds their size before spray drying (about 300 nm), highlighting a strong aggregation during the evaporation process not influenced by dilution.

Powder redispersion was assessed also at 1.48 mg/mL to compared HA, HA (PG) and HA-AmB powders both in water and in phosphate buffer (PB) at pH = 6.15, to simulate the acidic environment found in CF lungs. Hydrodynamic diameter, PdI and Zeta-potential values are reported in *Table 17*.

Table 17. Size, size distribution (PdI) and Z-potential (ζ) of particles redispersed in water and in PB at 1.48 mg/mL. Mean ± standard deviation (n = 3).

Sample	Water			PB (pH 6.15)		
	Size (nm)	**PdI**	**ζ (mV)**	**Size (nm)**	**PdI**	**ζ (mV)**
HA	444.1 ± 35.5	0.559	-46.6 ± 2.3	511.5 ± 74.0	0.656	-35.1 ± 1.6
HA + AmB	439.8 ± 23.3	0.496	-46.7 ± 3.39	754.9 ± 321	0.542	-31.6 ± 1.41
AmB	Aggregate > 1 μm		-31.1 ± 3.46	Aggregate > 1 μm		-24.5 ± 3.39

No deaggregation of microparticles was observed from AmB powder after spray drying. In contrast, blank and AmB-loaded HA NP were released both in water and in PB, presenting similar hydrodynamic diameters (around 440 nm) in water, but not in PB. Nevertheless, all particles showed a high polydispersion in each condition, with PdI > 0.5. The differences observed between particles redispersed in water and in PB could be due to the influence of pH on the protonation of HA. The acidic environment, in fact, could impair the release of particles that display HA chains on the surface by reducing the net charge of the polymer protonating HA acetamido groups [97]. This explanation is supported by Zeta-Potential values, that presented a greater reduction for HA and HA-AmB NP when they were in water or in PB (with a reduction of at least 11 mV) compared to AmB NP. In addition, no significant differences were observed between HA and HA-AmB NP Z-potential, once again suggesting a successful loading of AmB into the NP and a display of HA chains on the surface.

4.2 Nanoparticles containing AmB and HA 750-1000 kDa

4.2.1 Increase of stirring rate

The effect of the stirring rate on characteristics of nanoparticles containing AmB and HA 750-1000 kDa was assessed during particle production. The stirring rate, previously fixed at 165 rpm (Chapter 1, *paragraph 4.4.2*), was increased to 280 and 400 rpm to evaluate its effect on the final characteristics of nanoparticles. DLS measurements showed an increase of size and size distribution of particles produced at 280 rpm and the formation of aggregates in the micrometre range at 400 rpm *(Table 18)*.

Table 18. Size and size distribution (PdI) of particles obtained at different stirring rates.

Stirring rate (rpm)	Size (nm)	PdI
165	68.94	0.511
280	113.4	0.641
400	85.53 + visible aggregates	0.42

As reported in *Table 18*, particle distribution was quite wide in all cases, with PdI > 0.4. In contrast, hydrodynamic diameter of particles was largely affected by the effect of stirring rate, with an increase from 69 nm at 165 rpm, to 113 nm at 280 rpm, to aggregates above 1 μm at 400 rpm. This effect was probably due to faster interaction between ethanol-polymer and polymer-polymer chains, with the subsequent precipitation of polymeric aggregates instead of nanoparticles.

Basing of these results, 165 rpm was kept as stirring rate for particle production.

4.2.2 Increase of volume

As described in *paragraph 3.2.1*, the first batch was produced starting from 5 mL of HA aqueous solution at 0.5% (w/v), 2.25 mL of PG with AmB at 1 mg/mL and 35 mL of ethanol, resulting in a nanosuspension of 42.25 mL at 0.64 mg/mL. For spray drying, the volume of the nanosuspension was increased to obtain a higher amount of powder at the end of the process. For this purpose, it was increased by 3- (V3) and 4- (V4) folds reaching the final volumes of 126.75 mL and 169 mL, respectively. In each case, particle characteristics analysed by DLS did not present significant differences with the increase of volumes of the batches, presenting size around 70 nm and a PdI value around 0.5 *(Table 19).*

Table 19. Size and size distribution (PdI) of NP obtained in different volumes. Mean ± standard deviation (n = 2).

	Size (nm)	**PdI**
V1	72.2 ± 4.6	0.58 ± 0.1
V3	65.5 ± 2.7	0.46 ± 0.02
V4	71.3 ± 13.5	0.47 ± 0.09

Given the similar characteristics of nanosuspensions and the higher amount of powder collectable at the end of the process, V4 was considered for further studies of spray drying.

4.2.3 Addition of bulking agents

Before spray drying, bulking agents were added to the nanosuspension to avoid the irreversible aggregation of nanoparticles during the drying process and to improve their redispersion in aqueous media. Leucine was added directly to the nanosuspension, while α- and β-CD were first dissolved in water, as described in *paragraph 3.2.3*. Bulking agents were added to the nanosuspensions in different proportions *(Table 20, NP : Bulking agent)*.

Table 20. Size and size distribution (PdI) of particles before (NP) and after (NP + excipient) the addition of bulking agent. Numbers in brackets represent the NP : excipient weight-ratio. Mean ± standard deviation (n = 2).

	Size (nm)	**PdI**
NP	60.9 ± 6.9	0.4 ± 0.06
NP + α-CD (1 : 5)	80.8 ± 25.0	0.49 ± 0.19
NP + β-CD (1 : 1)	62.4 ± 8.1	0.37 ± 0.02
NP + Leu (1 : 1.5)	66.7 ± 23.1	0.25 ± 0.04

The slight increase of particle size observed after the addition of the excipients was not significant, and appeared to be related to the excipient concentration, with a higher increase for the nanosuspension containing α-CD.

4.2.4 Spray drying and powder characterization

Spray drying allowed to obtain dry powders for inhalation starting from nanosuspensions. The process was employed for HA NP and AmB-loaded HA NP dried with or without bulking agents (α-, β-cyclodextrin and leucine) to prevent nanoparticles aggregation. The yield% of the process, calculated as reported in *paragraph 3.2.4*, was similar for each sample with higher value for NP dried in presence of α-CD, although the observed differences were not statistically significant *(Table 21)*.

Table 21. Yield % of SD process of nanosuspensions containing HA NP and AmB-loaded nanoparticles with (NP + excipient) or without (NP HA + AmB) excipients. Mean ± standard deviation (n = 2).

Sample	NP HA	NP HA + AmB	NP + α-CD	NP + β-CD	NP + Leu
Yield%	67.5 ± 9.2	73.4 ± 9	78.3 ± 6.9	67 ± 5.7	74 ± 1.3

Laser diffraction analysis carried out on SD powders showed similar overlapped size distributions when cyclodextrins were added to the nanosuspensions, with $D_v(50)$ ~ 6 μm and $D_v(90)$ ~ 12 μm *(Table 22)*. Powder containing leucine presented lower values with $D_v(50) < 5$ μm and $D_v(90) < 9$ μm.

Table 22. Volume-weighted diameters of microparticles (μm). Mean ± standard deviation (n = 3).

	$D_v(10)$	$D_v(50)$	$D_v(90)$
NP HA + AmB	1.91 ± 0.1	4.52 ± 0.29	16.70 ± 3.23
NP + α-CD	1.84 ± 0.04	6.07 ± 0.43	13.48 ± 1.81
NP + β-CD	1.65 ± 0.06	5.44 ± 0.14	11.35 ± 0.12
NP + Leucine	1.95 ± 0.06	4.42 ± 0.81	8.91 ± 2.19

Among all the samples, powders obtained from nanoparticles without the addition of excipients presented the highest polydispersion, with a small population below 1 μm and a $D_v(90)$ = 16 μm *(Figure 49)*.

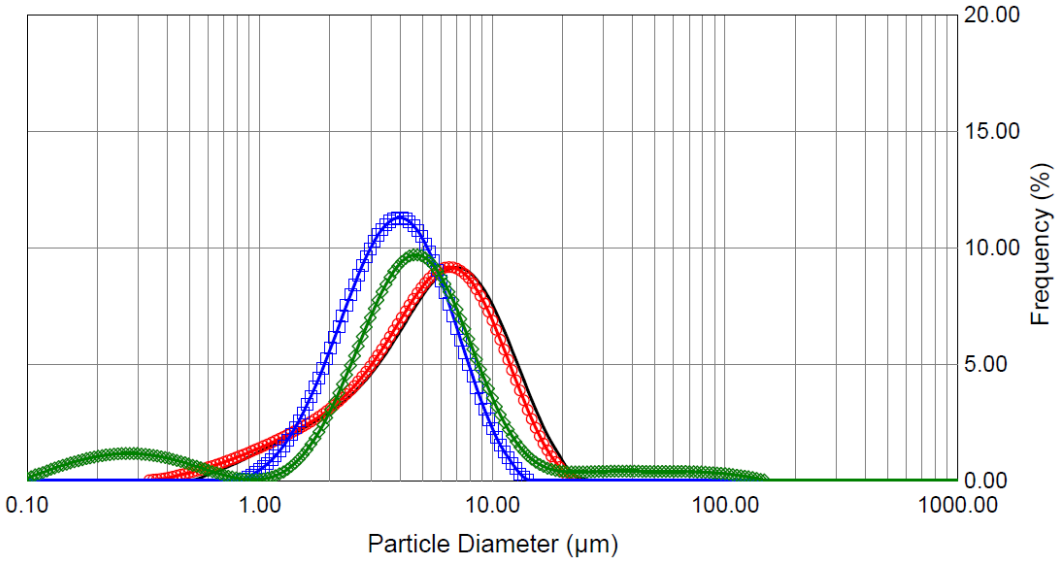

Figure 49. Particle size distribution of AmB nano-embedded HA microparticles SD without excipients (green line), or in presence of α-CD (black line), β-CD (red line) and leucine (blue line).

SEM acquisitions allowed to appreciate the differences among powders in term of morphology *(Figures 50 - 54)*.

All powders presented folded shapes, thus confirming the effect of PG during SD process *(paragraph 4.1.2)*. Significant differences were not observed between HA and HA-AmB containing microparticles, suggesting the loading of the drug in the nanoparticles *(Figures 50* and *51)*. Particles containing HA-AmB NP *(Figure 51)* displayed quite more wrinkled surface, but this effect could be also due to the electronic beam of the microscope.

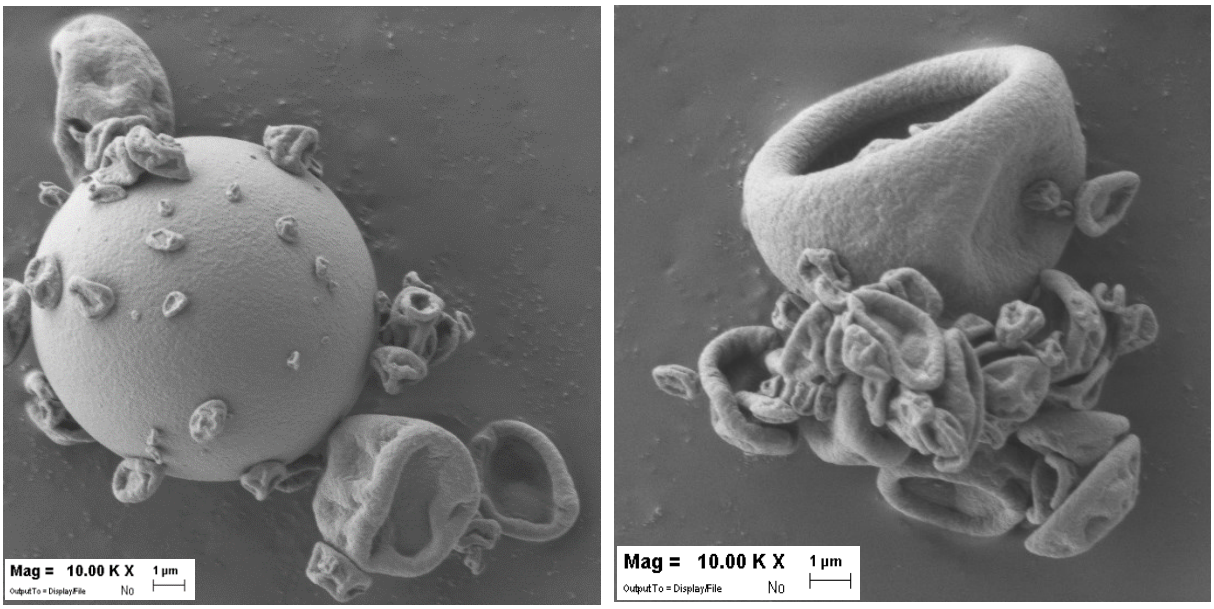

Figure 50. SEM images of HA microparticles obtained by the nanosuspension containing water/ethanol/PG mixture.

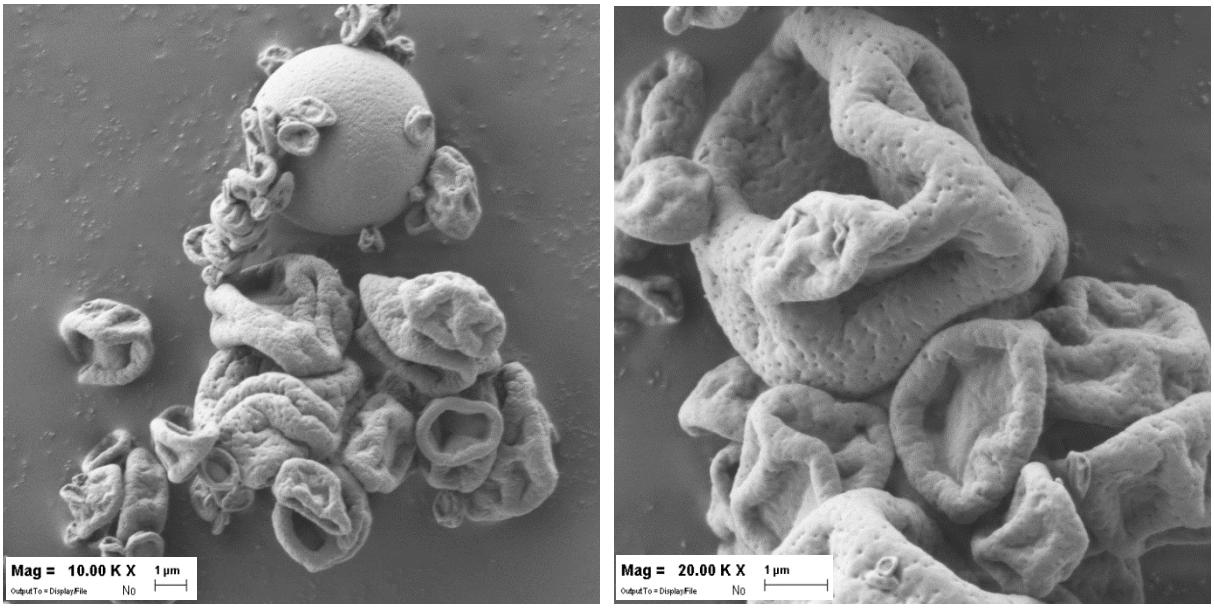

Figure 51. SEM images of microparticles containing HA-AmB NP.

In contrast, powders containing cyclodextrins presented smooth surfaces compared to the others. Their shapes were concave and similar to those of red blood cells *(Figures 52* and *53)*, with particles smaller than 1 μm attached to the outer surface or embedded in the pockets formed by the folding.

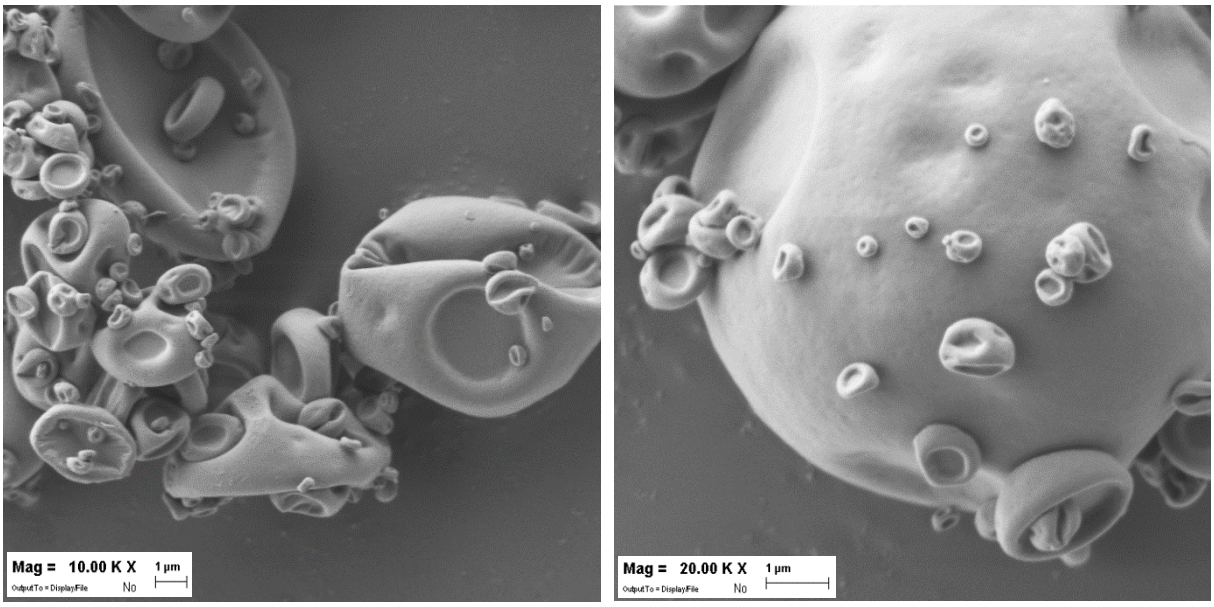

Figure 52. SEM images of microparticles containing HA-AmB NP + α-CD.

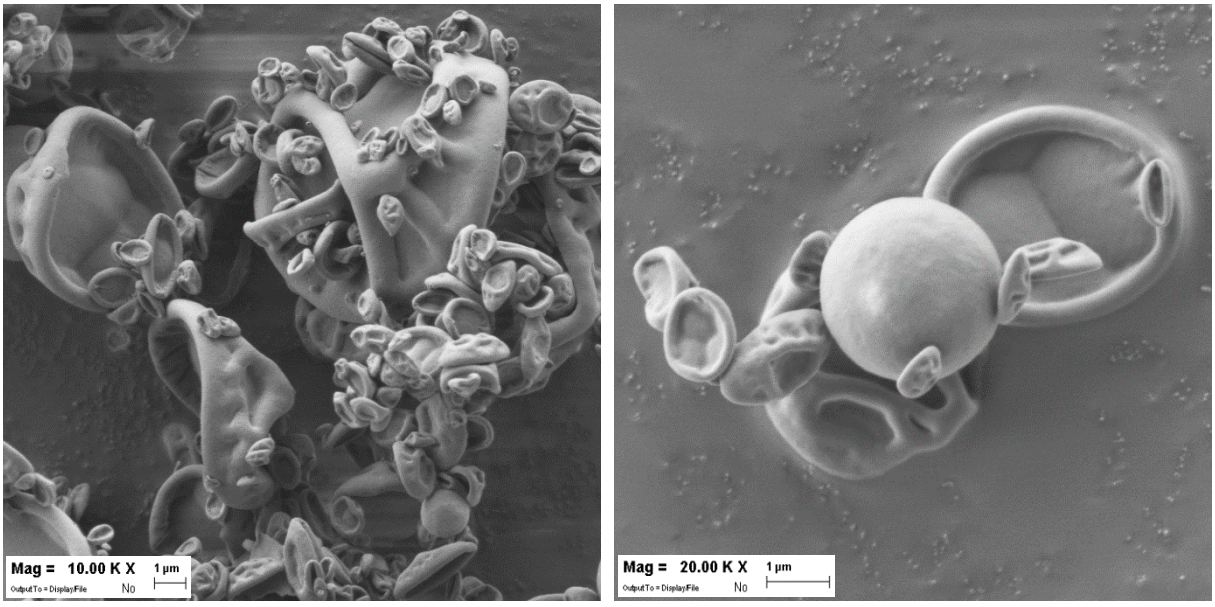

Figure 53. SEM images of microparticles containing HA-AmB NP + β-CD.

Powder containing leucine presented more evident differences compared to the others, due to the presence of small needles attached on the surface of folded particles and confirming the lower results obtained by laser diffraction *(Figure 54).*

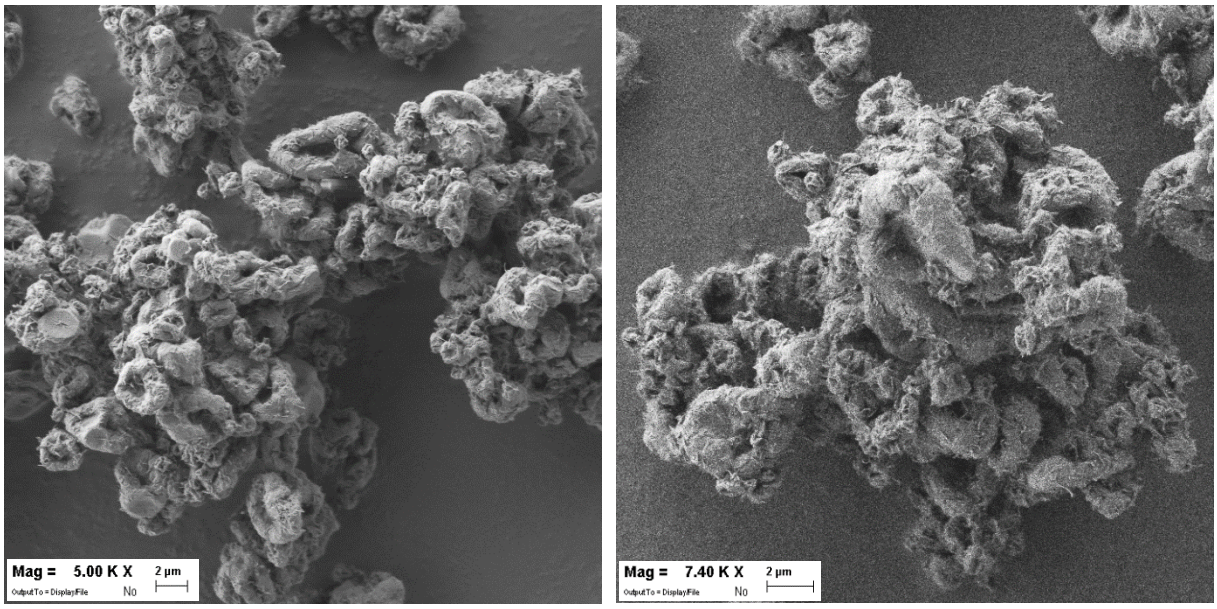

Figure 54. SEM images of microparticles containing HA-AmB NP + leucine.

4.2.5 Fourier Transform - Infrared Spectroscopy

IR spectra acquired from HA and AmB raw materials presented characteristic peaks due to the stretching of C = O bond. The peaks corresponded to the C = O of the ester and of the carboxylic acid in AmB molecule *(Figure 55)*, and of the amide and of the carboxylic acid in the polymer *(Figure 56)*, at wavelength values reported in the figures.

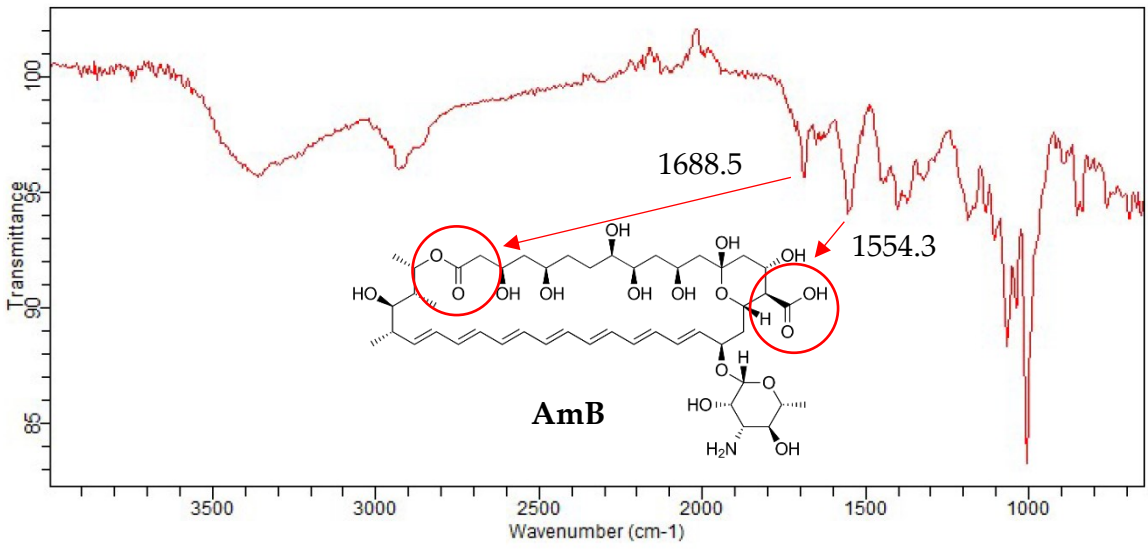

Figure 55. IR spectra of AmB raw material.

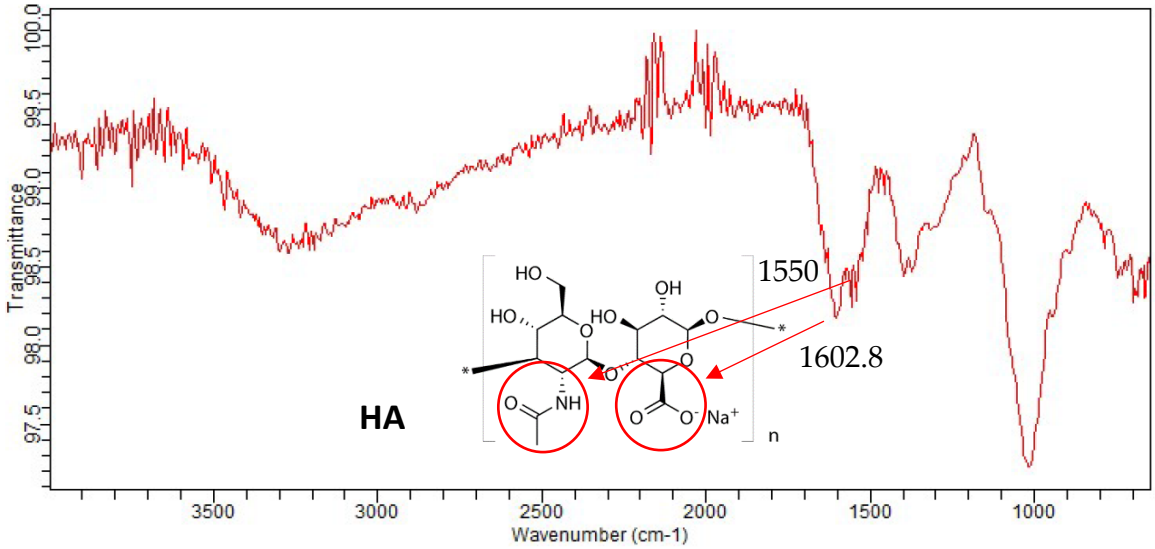

Figure 56. IR spectra of HA raw material.

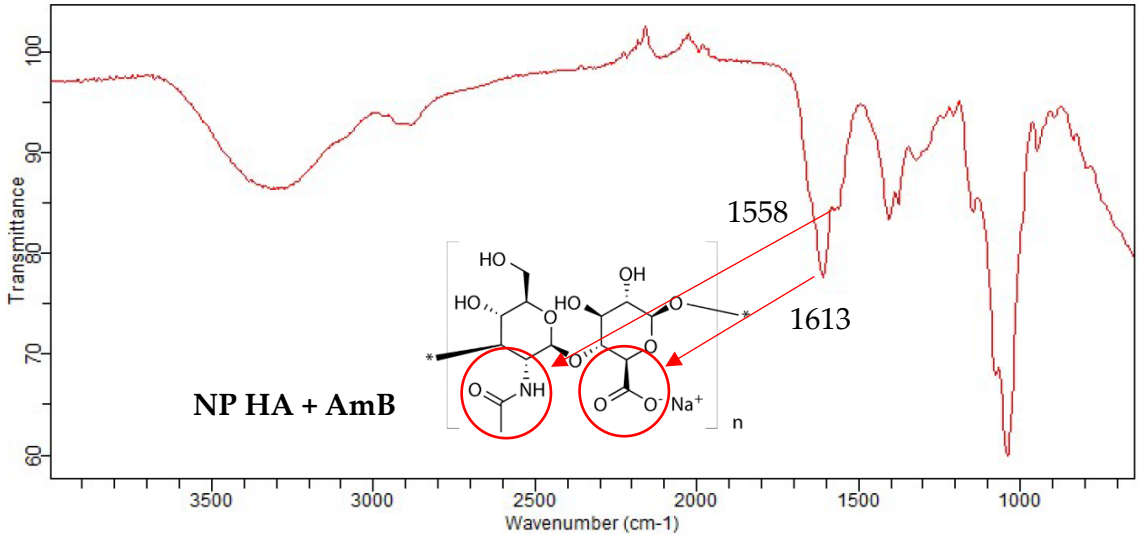

Figure 57. IR spectra of the powder containing AmB-loaded HA NP.

The IR spectrum acquired from the powder containing AmB-loaded HA nanoparticles was comparable to the one of HA raw material, which was the component present in greater quantity. Nevertheless, a slight increase of the wavenumber of C = O bonds stretching revealed a change in polymeric H-bonds, suggesting a change from inter-molecular HA-HA bonds to the instauration of new HA-AmB H-bonds *(Figure 57)*.

4.2.6 Drug content and drug loading efficiency of particles

The drug content of the powders was obtained after their solubilization and analysis by HPLC, as described in *paragraph 3.2.9*. Results revealed a lower drug content compared to the theorical one, with the detection of 65.3 ± 3.9% of the expected AmB (100%) in all samples. The loss of ~35% AmB could be due to the drug degradation or to the entrapment of smaller particles in the filter during the process of spray drying. The analysis of the chromatograms obtained by HPLC, compared to the one obtained by AmB raw material, did not present an increase of AUC of the characteristic peaks of impurities, thus supporting the hypothesis that smaller drug particles could be lost in the filter of the spray dryer for the aspiration effect.

Basing on this result, the real composition of the powders was re-calculated and reported in *Table 23*.

Table 23. Theoretical (Th%) and actual (Act%) composition of powders.

Component	**NP HA + AmB**		**NP + α-CD**		**NP + β-CD**		**NP + Leucine**	
	Th%	Act%	Th%	Act%	Th%	Act%	Th%	Act%
HA	91.7	94.7	15.3	15.4	45.8	46.5	36.7	37.2
AmB	8.3	5.3	1.4	0.91	4.2	2.7	3.3	2
Excipient	-	-	83.3	83.7	50	50.8	60	60.8

The amount of loaded AmB in HA nanoparticles was calculated as the difference of AmB actual content with free AmB, found in solution after dispersion of the powder in DMSO and subsequent filtration trough a 0.20 μm filter. Loading efficiency % amounted to 80.5 ± 2.4 %.

4.2.7 Powder redispersion

The behaviour of microparticles after redispersion in sodium chloride 10 mM was investigated at 0.5 and 1 mg/mL. The suspensions were sonicated and DLS measurements

carried out at different sonication times to assess its effect on nanoparticle redispersion. In contrast to other samples, before sonication nanoparticles spray dried without the addition of bulking agents presented doubled size *(Table 24, Figure 58)*. These results highlight the important effect of excipients, able to prevent nanoparticles aggregation and to improve their release in aqueous medium. Nevertheless, all sample presented a higher particle size compared to the starting nanosuspensions, which was below 80 nm.

Table 24. Size (nm) of nanoparticles redispersed at 0.5 mg/mL. Mean ± standard deviation (n = 3).

t_{sonic} (min)	NP HA + AmB	NP + α-CD	NP + β-CD	NP + Leucine
0	844.3 ± 345.8	473.8 ± 148.5	363.9 ± 49.4	394.9 ± 71.3
5	335.2 ± 98.8	183.1 ± 57.8	364.1 ± 192.6	356.6 ± 83.8
15	280.7 ± 68.5	187.4 ± 10.1	314.2 ± 216.4	358.5 ± 159.2
30	270.6 ± 80.6	189.0 ± 28.7	253.4 ± 172.2	258.2 ± 159.2
60	225.8 ± 16.9	237.7 ± 93.7	153.5 ± 49	167.1 ± 90.1

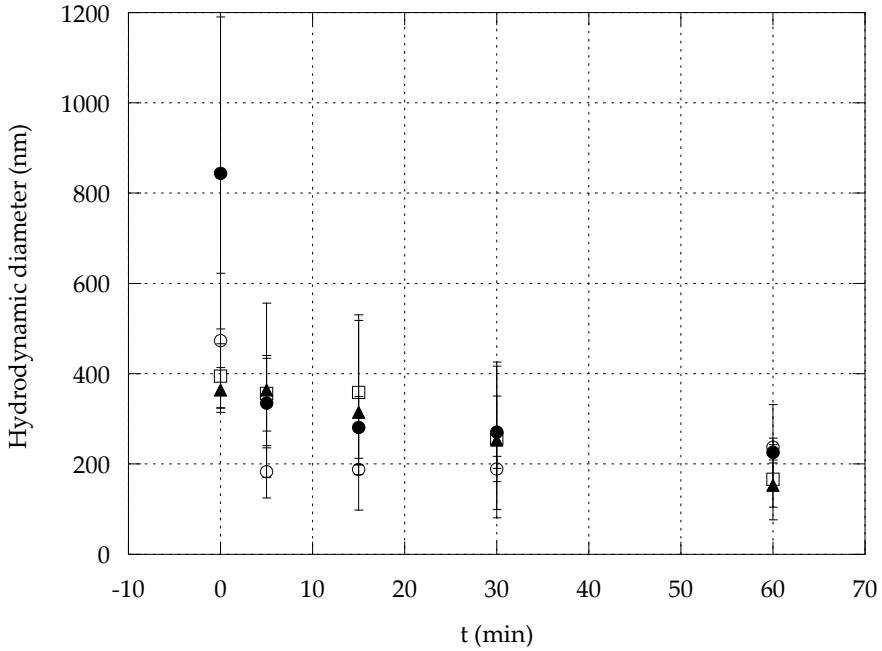

Figure 58. Hydrodynamic diameter of released particles at 0.5 mg/mL before and after 5, 15, 30 and 60 minutes of sonication. NP HA + AmB (●), NP + α-CD (○), NP + β-CD (▲) and NP + Leu (□). The bars represent the standard deviation (n = 3).

Sonication improved the redispersion of nanoparticles, leading to hydrodynamic diameters below 200 nm in presence of bulking agents. In particular, microparticles containing α-CD *(empty dot)* led to the release of smaller NP after 5 minutes of sonication.

After resuspension at the concentration of 1 mg/mL, microparticles showed a similar behaviour after sonication, but with higher size, always above 200 nm *(Table 25, Figure 59)*.

Table 25. Size (nm) of nanoparticles redispersed at 1 mg/mL. Mean ± standard deviation (n = 3).

t_{sonic} (min)	NP HA + AmB	NP + α-CD	NP + β-CD	NP + Leucine
0	1159.2 ± 206.1	604.5 ± 86.8	584.4 ± 126.6	748.3 ± 230.3
5	371.4 ± 98.6	384.3 ± 187	541.2 ± 206.2	580.2 ± 361.9
15	325.4 ± 117.7	367.6 ± 221.2	441.9 ± 134.9	360.5 ± 70
30	319.7 ± 156.9	265.9 ± 64.5	348.2 ± 138.7	292.7 ± 76.2
60	345.7 ± 178	224.2 ± 90.6	253.7 ± 123.8	200.7 ± 63.1

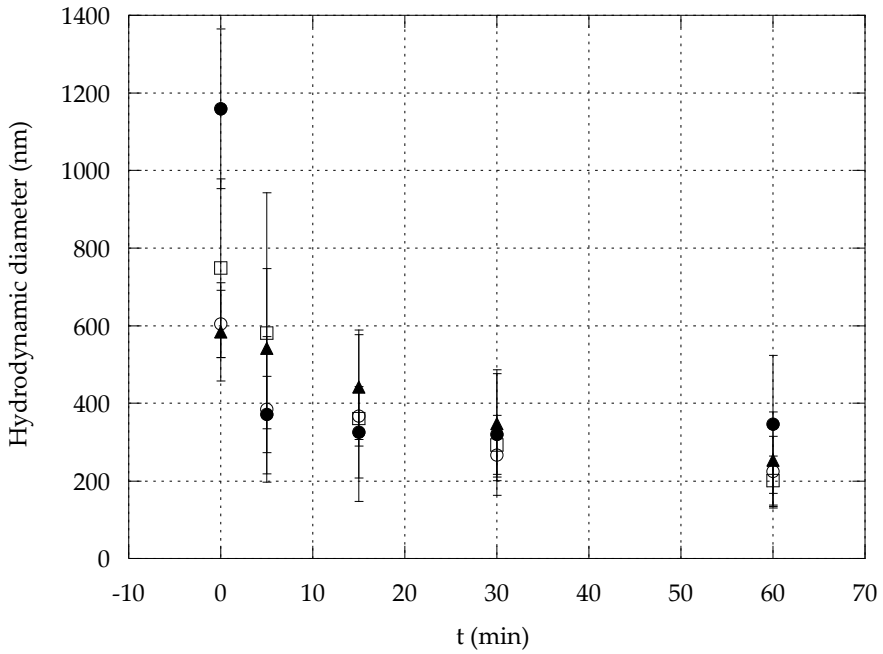

Figure 59. Hydrodynamic diameter of released particles at 1 mg/mL before and after 5, 15, 30 and 60 minutes of sonication. NP HA + AmB (●), NP + α-CD (○), NP + β-CD (▲) and NP + Leu (□). The bars represent the standard deviation (n = 3).

At both concentrations, sonication enhanced the release of nanoparticles, but without restoring their original sizes before spray drying. Nevertheless, in more diluted conditions (0.5 mg/mL), particle presented lower dimensions, especially those obtained with α-CD. Finally, all samples had similar values of zeta potential, with negative charge around -42.2 ± 5.4 mV.

4.2.8 Aerodynamic performance

Preliminary information about the aerodynamic performance of powders were collected using a FSI and reported in *Table 26*.

Table 26. EF% and FPF% of powders. Mean ± standard deviation (n = 2).

	EF%	**FPF%**
NP HA	74.7	35.1
NP HA - AmB	74 ± 16.8	57.9 ± 34.4
NP + α-CD	68.8 ± 1.4	31.3 ± 0.3
NP + β-CD	88.1 ± 4.5	36.2 ± 1.5
NP + Leu	91.4 ± 1.2	27.3 ± 1.1

Powders containing leucine presented the higher value of EF%, amounting to 91% compared to the others. In contrast, a lower fraction (27%) was able to reach the fine particle collector. Powder containing α-CD had the lower EF%, but an FPF% quite similar to the powder containing β-CD and to the HA blank microparticles. A better aerodynamic performance was observed for powder SD without the addition of excipient, with an FPF% higher than 57%. Nevertheless, results showed a wide distribution with high value of standard deviation.

4.2.9 Cytotoxicity assay

Tables 27 and *28* report the cytotoxicity assay data on H441 cell line which presented a viability above 97% at all tested concentrations, for both AmB raw material (RM) and AmB nano-embedded microparticles. AmB at 100 μg/mL, the higher concentration tested, was already assayed in H441 cell line without cytotoxicity [98][99].

Table 27. Cell viability% of H441 treated with AmB RM for 4h and 24h. Mean ± standard deviation (n = 3).

C_{AmB} (μg/mL)	0.125	0.25	0.5	1	5	10	50	100
4h	98.6 2.4	99.5 ± 1.6	99.5 ± 1.2	98.8 ± 0.9	98.6 ± 2.0	99.6 ± 1.9	100.2 ± 0.9	99.8 ± 2.2
24h	98.9 ± 2.3	99.3 ± 1.2	99.3 ± 0.8	99.5 ± 0.9	98.0 ± 1.4	98.9 ± 1.2	99.6 ± 1.1	97.9 ± 2.1

Table 28. Cell viability% of H441 treated with AmB-loaded NP for 4h and 24h. Mean ± standard deviation (n = 3).

C_{AmB} (μg/mL)		1	5	10	50
NP AmB - HA	**4h**	100.1 ± 2.6	100.1 ± 0.5	97.9 ± 1.5	99.7 ± 1.1
	24h	101.8 ± 1.0	100.2 ± 0.2	99.3 ± 2.9	98.7 ± 2.2
NP + Leucine	**4h**	100.1 ± 1.1	98.5 ± 0.4	99.7 ± 0.8	96.4 ± 2.8
	24h	101.1 ± 0.4	99.6 ± 1.7	99.2 ± 0.2	99.0 ± 2.5
NP + α-CD	**4h**	98.1 ± 0.7	98.8 ± 2.0	100.1 ± 1.2	98.8 ± 0.6
	24h	98.4 ± 0.4	99.5 ± 0.5	100.0 ± 1.0	99.6 ± 1.1
NP + β-CD	**4h**	98.1 ± 0.8	99.1 ± 1.3	100.9 ± 2.1	99.9 ± 2.4
	24h	97.0 ± 1.0	97.5 ± 0.1	100.0 ± 0.9	100.3 ± 1.5

Cytotoxicity assay on Calu-3 cells, showed a cell viability% above 99% when treated with AmB RM at all tested concentrations *(Table 29)*. In contrast, Calu-3 cells treated with AmB-loaded nano-embedded microparticles presented a slight reduction of cell viability%, that however remained always above 71% *(Table 30)*. The reduction was observed only after 24h of treatment, and it resulted more marked with microparticles containing HA-AmB NP spray dried without excipients or in presence of α-CD.

Table 29. Cell viability% of Calu-3 treated with AmB RM for 4h and 24h. Mean ± standard deviation (n = 3).

C_{AmB} (μg/mL)	**0.125**	**0.25**	**0.5**	**1**	**5**	**10**	**50**	**100**
4h	100.7 ± 7.4	101.1 ± 1.6	99.0 ± 3.5	99.8 ± 1.5	100.9 ± 1.4	105.0 ± 5.8	109.4 ± 9.1	109.3 ± 7.7
24h	99.6 ± 10.4	108.0 ± 4.5	109.1 ± 9.2	105.9 ± 6.3	109.9 ± 5.9	114.0 ± 3.0	126.3 ± 0.8	126.2 ± 1.2

Table 30. Cell viability% of Calu-3 treated with AmB-loaded NP for 4h and 24h. Mean ± standard deviation (n = 3).

C_{AmB} (μg/mL)		**1**	**5**	**10**	**50**
NP AmB - HA	**4h**	101.3 ± 12.6	97.4 ± 7.7	100.8 ± 9.2	100.3 ± 11.1
	24h	105.6 ± 4.7	98.8 ± 1.6	90.9 ± 4.0	71.7 ± 6.6
NP + Leucine	**4h**	102.8 ± 12.0	104.6 ± 5.4	108.1 ± 1.4	103.1 ± 1.0
	24h	106.5 ± 6.8	102.6 ± 12.4	101.3 ± 14.3	82.6 ± 15.1
NP + α-CD	**4h**	97.9 ± 11.2	100.0 ± 5.6	105.7 ± 2.8	105.2 ± 0.8
	24h	94.0 ± 1.5	92.9 ± 0.0	93.9 ± 8.4	74.1 ± 5.4
NP + β-CD	**4h**	99.0 ± 6.4	96.1 ± 3.8	102.1 ± 3.5	105.8 ± 0.2
	24h	99.0 ± 3.4	96.4 ± 3.5	96.7 ± 10.2	86.9 ± 17.7

Based on these results, all nano-embedded microparticles can be considered substantially harmless for both cell lines in the range of AmB concentration tested.

4.2.10 Particle deaggregation assessed by light microscopy

Calu-3 cells cultured at air-liquid interface (ALI) allowed to obtain a polarized monolayer more morphologically representative of the airway epithelium compared to cells cultured in liquid-liquid interface conditions [100]. In particular, it presents physiologically similarities of both cellular and noncellular components including mucus secretions, better simulating CF conditions [101]. Calu-3 cells were cultured on Transwell® inserts until confluence (*Figure 60*).

Figure 60. Image of Calu-3 monolayer cultured at ALI taken with an Olympus IX81 microscope.

When TEER value was between 900 - 1000 $cm^2 \cdot \Omega$, about 10 days after seeding, cells were placed onto an Olympus IX81 microscope to monitor particle dissolution. Four samples, including AmB-HA nanoparticles spray dried with or without the addition of excipients, were compared each other's and with AmB RM.

Microparticles presented very different behaviour when in contact with the cell monolayer. In particular, all nano-embedded microparticles SD with or without excipients *(Figure 61, Panels A - D)*, presented a faster de-aggregation compared to AmB RM *(Panel E*), suggesting the important role of sodium hyaluronate as well as of bulking agents in enhancing AmB presentation to the cells. Powder containing α-CD *(Panel A*) was the fast-dispersing one, with a quite completely release of nanoparticles within 60s. Powder containing leucine *(Panel C)* presented a similar behaviour, but slightly slower, taking more than 90s for the redispersion of particles.

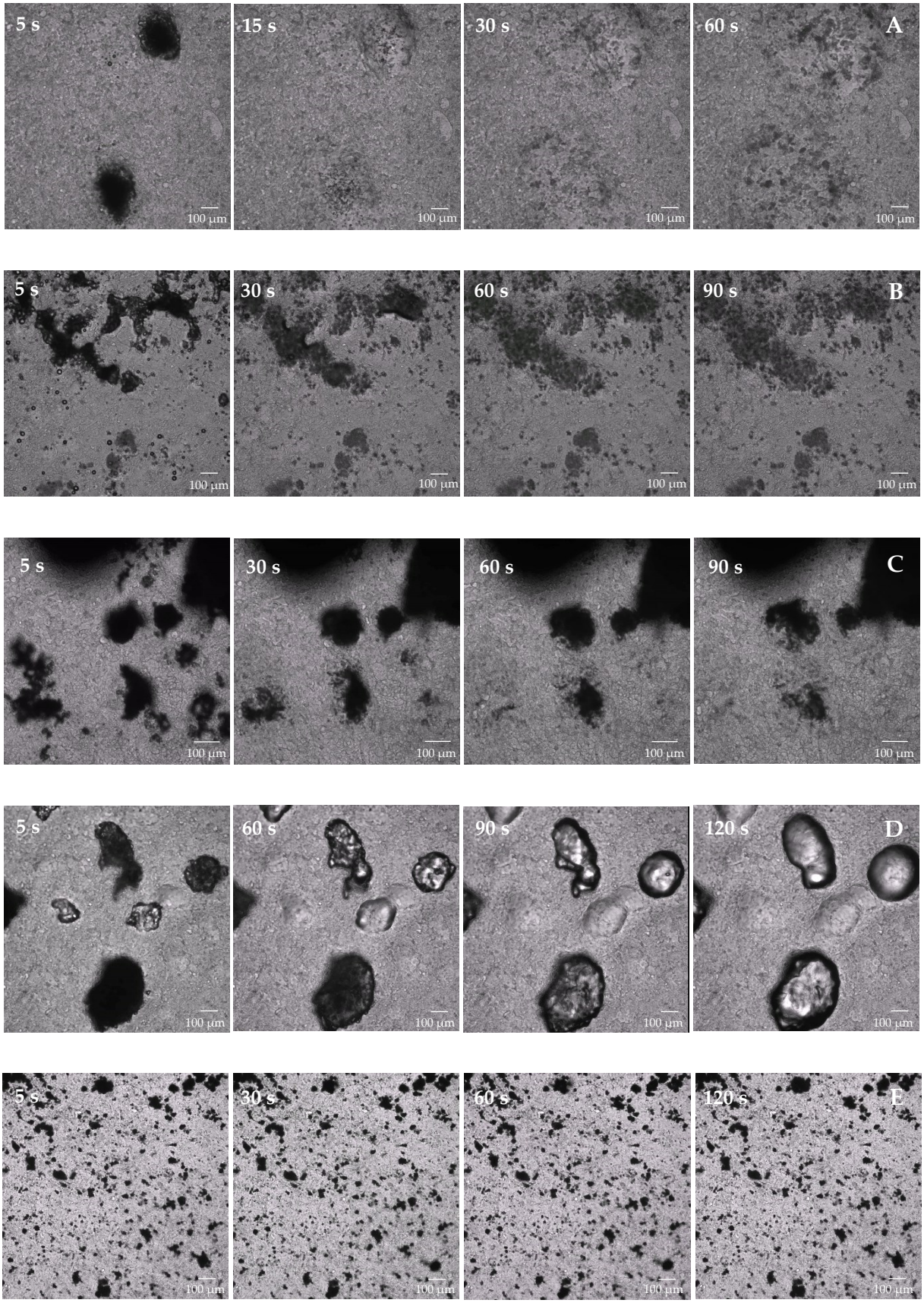

Figure 61. Particle dissolution over time. Panel A: NP + α-CD; B: NP + β-CD; C: NP + leu; D: NP AmB - HA; E: AmB RM.

Powder containing β-CD *(Panel B)*, displayed a particular behaviour when in contact with mucus. After aerosolization, in fact, it released smaller and stable crystals that did not dissolve after 90s. Finally, powder containing HA-AmB NP spray dried without the addition of excipients *(Panel D)*, dispersed quite fast but with a different mechanism compared to the others. Deeper information about solid state of particles were obtained by x-ray powder diffraction (XRPD), that revealed a higher degree of crystallinity for powders spray dried without excipients (23.4%) and in presence of β-CD (20.3%) (*Figure 62, Panel A* and *C*, respectively), compared to powders containing α-CD (9.6%) and leucine (17.9%), thus partly explaining their different behaviour when in contact with mucus.

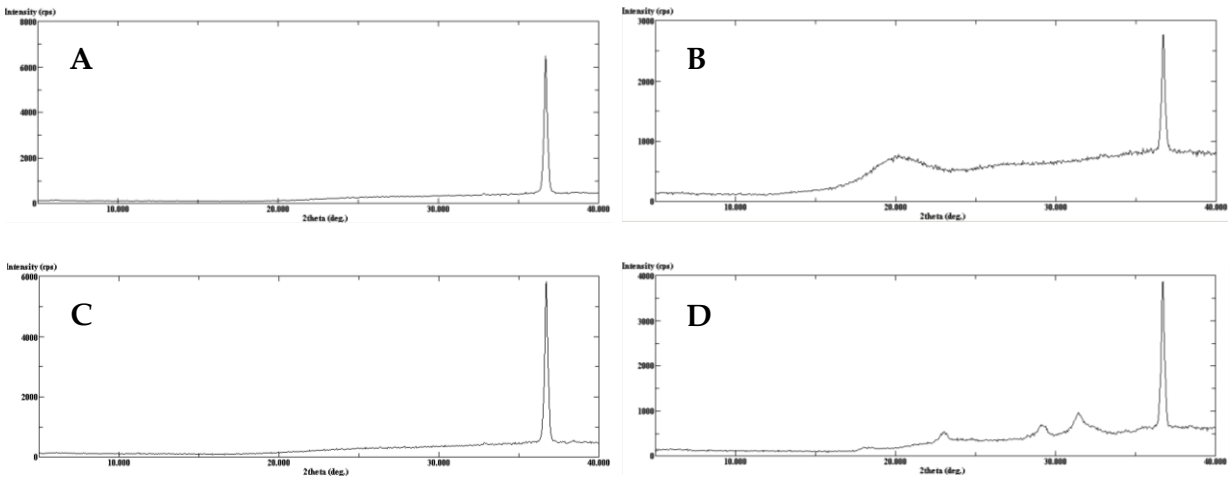

Figure 62. XRPD of microparticles containing NP AmB - HA (Panel A); NP + α-CD (Panel B); NP + β-CD (Panel C); NP + leu (Panel D).

5. CONCLUSIONS

The present chapter aimed to develop nano-embedded microparticles for AmB pulmonary delivery. The research started with the employment of a medium-low MW range of HA (130-300 kDa), that led to the production of loaded-nanoparticles around 300 nm in size. Blank, AmB and AmB-loaded HA nano-embedded microparticles were obtained by spray drying. Powder characterization by SEM highlighted the effect of PG on particle morphology, with folded structures compared to the spherical ones obtained from nanosuspension without PG. In addition, AmB SD presented completely different fused aggregates that suggested the successful encapsulation of the drug in presence of HA. The folded morphology of particles guaranteed a better aerodynamic performance with FPF% > 15%. Particle redispersion assessed by DLS presented a slight particle aggregation during SD with increased aerodynamic diameters above 400 nm. Therefore, produced particles present sizes that could lead them to macrophage engulfment, thus impairing their activity for the treatment of CF. In addition, it is important to remind the problems encountered during the increase of the scale of production of nanoparticles, that led to the precipitation of visible aggregates.

For this reason, a higher HA MW was chosen for particle production (750-1000 kDa), to exploit also the polymer anti-inflammatory effect which may be beneficial in CF patients. In this case, the increase of volume of produced nanosuspensions was successfully carried out for spray drying, without significant changes of size, that was between 60 - 80 nm. Dry powders for inhalation were obtained by spray drying starting from nanosuspensions, also in presence of bulking agents (α-, β-CD and leucine). HPLC analyses revealed a loss of 35% AmB during the process, probably due to the aspiration effect on smaller particles during the drying process. The AmB encapsulation in HA nanoparticles was successful, with an encapsulation efficiency of 80%. Powders, observed by SEM, displayed folded particles that resulted in acceptable aerodynamic performances with FPF% > 27%. In NaCl 10 mM, the presence of bulking agents enhanced the release of nanoparticles compared to powders spray dried without excipients, thus confirming their advantages of avoiding

irreversible aggregation during drying. Nevertheless, hydrodynamic diameters resulted about 200 nm for all samples, corresponding to more the 2-fold the size of particles before drying. *In vitro* studies on Calu-3 and NCI-H441 pulmonary cell lines guaranteed the safety of 4h and 24h of treatment with microparticles containing 1 - 50 μg/mL of AmB, and the fast release of nanoparticles upon contact with mucus compared to AmB RM.

CHAPTER 3

HA-Fluconazole nanoparticles for treatment of lung infections

1. INTRODUCTION

1.1 Pulmonary fungal infections

1.1.1 General aspects

Fungi are eukaryote organisms constituting a distinct kingdom. Their cells are much larger than bacteria and their molecular processes closely similar to those of plants and animals. Fungi can exist in the form of independent single cells, usually called *yeasts*, or as cylindrical cells (hyphae) called *moulds.* In humans, fungi establish endemic or opportunistic mycoses. Besides, since only few fungi pathogenic for humans are sufficiently virulent to infect healthy host (endemic mycoses), most of the fungal infections are opportunistic. Under normal circumstances, in fact, the epithelial surfaces prohibit invasion of micro-organisms and the mucociliary barrier of the respiratory tract prevents aspiration of fungal cells and spores in contrast to damaged tissue or immunocompromised hosts [102]. Most of systemic fungal infections begin in the lungs after inhalation of the aerosolized fungi. Once established in the lungs, the infection can spread to other organs by the hematogenous or lymphatic route [103].

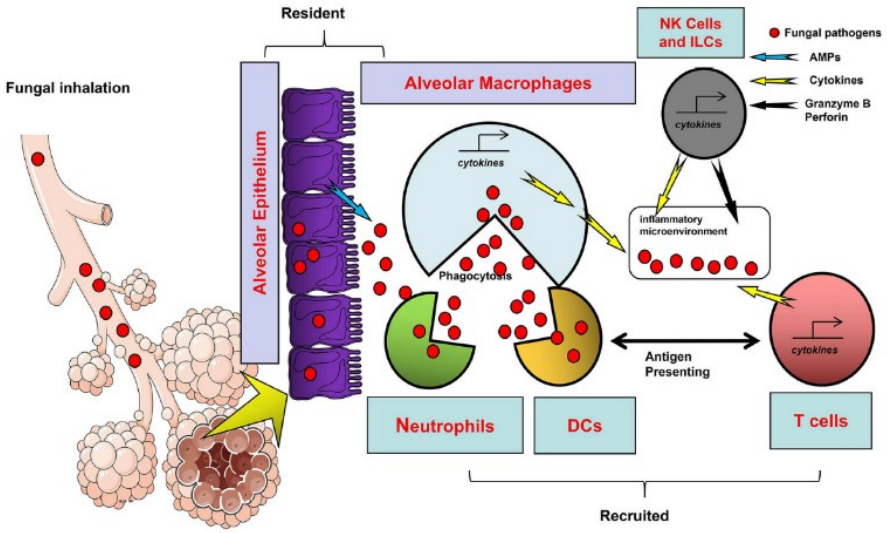

Figure 63. Macrophages involvement against pulmonary fungal infection. Reproduced with permission of [64].

For this reason, pulmonary macrophages and innate immune cells are the first host cells after fungi inhalation and play a critical role in the progression of the disease *(Figure 63)* [104][64]. In view of this, macrophages represent a dense site of fungi in the lungs and a remarkable target for antifungal drugs and inhaled formulations.

1.1.2 Fluconazole

Fluconazole is the most common drug employed for the treatment of fungal infection diseases, presenting reduced costs and good tolerability. It belongs to the class of azoles that acts by inhibiting the synthesis of the ergosterol, a constituent of the fungal membrane, in contrast to other antifungal drug classes that operate on membrane integrity (polyenes and echinocandins) and on the synthesis of nucleic acids (pyrimidine analogues) *(Figure 64)* [105].

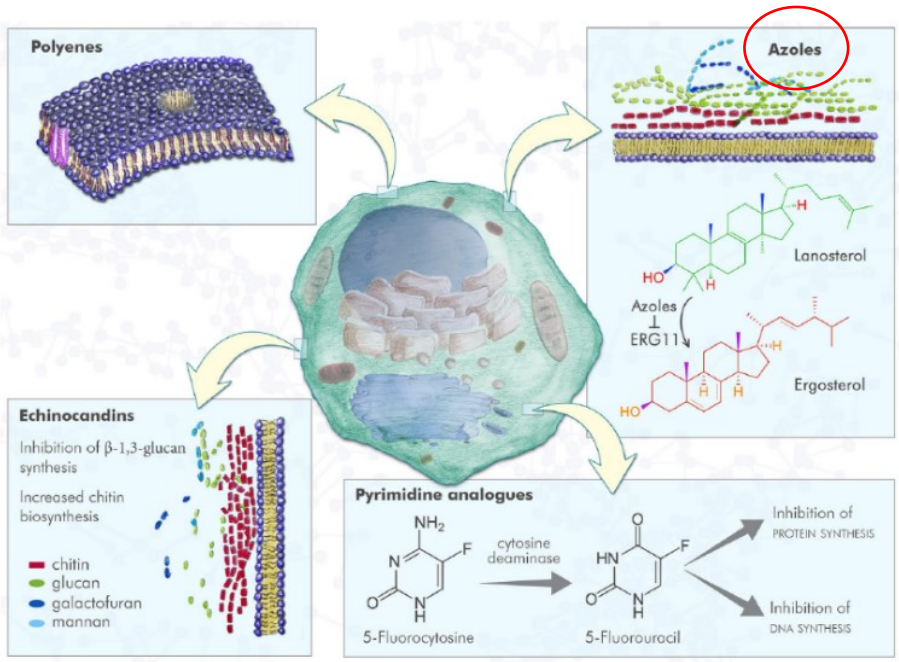

Figure 64. Antifungal drug mechanisms. Reproduced with permission of [105].

Antibody therapy has been also investigated, developing mAb for the opsonization of fungal cells, complement activation and toxin neutralization enhancing host defence [106][107].

Azoles have been classified as *imidazole* and *triazole*, according to the number of nitrogen atoms in the five-membered ring. Fluconazole belongs to the *triazole* class (*Figure 65*, [108]).

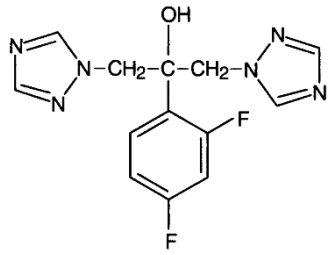

Figure 65. Chemical structure of fluconazole.
Reproduced with permission from [108].

Azole mechanism is based on the inhibition of *lanosterol 14α-demethylase (Erg11)*, a microsomal enzyme involved in the biosynthesis of ergosterol from lanosterol. The subsequent accumulation of methylsterols leads to the disturbance of the phospholipid packing altering and inhibiting the fungal growth acting as fungistatic. From the first generation of azoles in the late 1970s to the third one in the first decade of the 2000s, activity, safety and pharmacokinetics have been improved [105].

Azoles are active against different fungal species, including *Candida* (*albicans*, *tropicalis*, *glabrata*, *parapsilosis*), *Cryptococcus neoformans*, *Coccidioides* spp. and also possess anti-protozoal effect against *Leishmania major*. In contrast, *Aspergillus* spp. are resistant to fluconazole. Fungal resistance is keeping more and more attention and has led to the investigation of chemical modifications of drug molecules in order to make them effective also against fungal resistant strains. Secondary resistance to fluconazole of *Candida* spp., and in particular of *C. albicans*, appears to be emerging issue due to increased drug efflux, alteration or increase in the drug target and development of compensatory pathways for producing the target ergosterol [108][109][110][111].

Fluconazole is on the market as tablet and suspension for oral administration and in solution for intravenous administration. In addition, nanoparticle formulations have been developed, in form of liposomes [112], solid lipid nanoparticles [113] and nanocomposite [114].

1.2 Nanoparticles to target alveolar macrophages

Formulations designed for antifungal drugs delivery to alveolar macrophages enhance the efficacy of the treatments, increasing the amount drug to the site of action with a reduction of the doses and side effects. Nanocarriers could be employed for this purpose if particular characteristics are guaranteed. Targeting to alveolar macrophages, in fact, can be passive, involving physicochemical properties of nanoparticles such as size, surface charge and composition, or active, exploiting binding with specific ligands. Greater macrophage uptake is observed for nanoparticles bigger than 200 nm and even more for particles between 1 - 6 μm, thanks to a better contact with macrophage membrane [45]. Size represent one of the main factors that influences macrophage uptake, but some studies demonstrated that shape also plays an important role in the uptake of particles by macrophages, suggesting the spherical one as the favoured for uptake. As concern surface charge, positively charged particles interact more readily with negatively charged sialic acid present on the surface of macrophages enhancing the phagocytosis, even if it has been noted that positively charged particles are more toxic because of generation of reactive oxygen species and induction of apoptosis. It has been also proved that harder and stiffer particles are internalized more efficiently by macrophages than their softer counterpart. Finally, the coating of particle surface with hydrophilic materials facilitates the recognition by alveolar macrophages, even if surface coating with polyethylene glycol makes particles stealth and resistant to opsonization by serum proteins delaying their recognition by macrophages. Nevertheless, for nanocarriers to be preferentially taken up by macrophages, active targeting results as the optimal method to increase recognition and internalization enhancing the uptake. Particle surface can be decorated with ligands able to recognize macrophage receptors including Fc receptors, complement factor receptors, mannosyl, galactosyl, lipoprotein, folic acid and fibronectin receptors [45][56][115]. Macrophages express also CD44 receptor for hyaluronic acid, whose binding have been demonstrated to increase 2-fold ofloxacin-containing microparticle uptake upon incubation [116]. Hyaluronic acid, together with intrinsic targeting, presents other advantages including biodegradability and biocompatibility.

2. AIM

The aim of the present part of the thesis was to develop fluconazole-loaded nanoparticles aimed to target alveolar macrophages for the treatment of fungal infections. Sodium hyaluronate with proper molecular weight was chosen and employed for drug loading, exploiting its targeting to CD44 receptors. HA NP obtained by anti-solvent precipitation were then compared to HA-Chitosan NP produced by ionic gelation, investigating their size, size distribution and encapsulation efficiency%.

Finally, powders for inhalation were obtained by spray drying fluconazole-HA nanosuspensions and characterized by scanning electron microscopy and laser diffraction.

3. MATERIALS AND METHODS

3.1 MATERIALS

Sodium Hyaluronate 15-30 kDa and 130-300 kDa were obtained from *Contipro* (Czech Republic). Fluconazole was supplied by *Dayangchem*, China. Chitosan ChitoClear® (MW = 252 kDa; deacetylation degree = 93%) was purchased from *Primex* (Island) and chitosan lactate (MW = 40 kDa; deacetylation degree = 87%) from *Heppe Medical Chitosan* (Germany). Ultrapure water was purified by reverse osmosis with Purelab Pulse flex, *Elga-Veolia*, Italy. Acetonitrile was of analytical grade.

3.2 METHODS

3.2.1 Preparation of fluconazole-loaded chitosan/HA NP

Aqueous solution of chitosan (CS) and HA at different concentrations were separately prepared. Acetic acid was added at 1% (v/v) to improve the solubilization of chitosan Chitoclear®, while chitosan lactate was soluble in water at neutral pH. HA solution was added dropwise to CS solution at a volumetric ratio 1:1. Different chitosan and polymer molecular weights and concentrations were tested and reported in *paragraph 4.1.1*. For drug-loaded NP, fluconazole (Flz) was dissolved in CS aqueous solution at a concentration of 3 mg/mL at 30°C. HA solution was then added at room temperature under Ultra Turrax®-homogenisation at 5000 rpm.

3.2.2 Preparation of fluconazole-loaded HA NP

Fluconazole-loaded nanoparticles were obtained by anti-solvent precipitation using ethanol as the anti-solvent in water, in a volumetric ratio 80:20 (ethanol:water). HA 130-

300 kDa was first dissolved in ultrapure water at a concentration of 1% (w/v). Two different approaches were assessed for Flz: it was solubilized in water with HA at 3 mg/mL or in ethanol at 0.75 mg/mL, to obtain in both cases a final nanosuspension concentration of 0.6 mg/mL. Ethanol was added dropwise, acting as anti-solvent for the polymer and promoting the precipitation of HA on the drug. The process was carried out at room temperature and under magnetic stirring at 165 rpm.

3.2.3 Dynamic Light Scattering

Size, size distribution and Z-potential of Flz-loaded nanoparticles were assessed by Dynamic Light Scattering (Zetasizer Nano ZS, *Malvern Panalytical*, UK) as described in *paragraph 3.2.2* (Chapter 2). Different dispersant properties were fixed according to the nanosuspension in water/ethanol mixture (Viscosity = 1.3022 cP; RI = 1.354) or in HBSS for powder redispersion (Viscosity = 0.8894 cP; RI = 1.33; ε = 78.5).

Dilution 1:20 was performed on Flz-HA nanosuspensions before DLS measurements.

3.2.4 Spray Drying

To obtain dry powders for inhalation, nanosuspensions were dried using a Mini Spray Dryer B-290 (*Büchi*, Switzerland) connected with the inert loop B-295. Set process parameters are reported in *paragraph 3.2.4* (Chapter 2). Aspiration was fixed at 32 m^3/h (80%) and T_{outlet} recorded amounted to 55°C. The yield% of the process was calculated according to the *Eq. 5*, reported in the same paragraph.

3.2.5 Laser Diffraction

Analyses by laser diffraction were carried out as described in Chapter 2, *paragraph 3.2.6*.

Data were expressed in terms of volume-weighted diameter (D_v) for 10^{th}, 50^{th} and 90^{th} percentiles, corresponding to $D_v(10)$, $D_v(50)$ and $D_v(90)$ respectively.

3.2.6 Scanning Electron Microscopy

The morphology of the powders was assessed by scanning electron microscopy (SEM) at different magnifications (2, 5, 10 and 20k X). Samples were prepared as described in Chapter 2, *paragraph 3.2.7*.

3.2.7 High Pressure Liquid Chromatography: Encapsulation Efficiency

The amount of Flz loaded in the nanoparticles (Encapsulation Efficiency %, EE%) was quantified indirectly by liquid chromatography using an HPLC Agilent technologies 1200 (*Agilent,* USA). The nanosuspensions were filtrated by tangential filtration using a MidiKros Hollow Fiber Filter Module® with length = 41.5 cm, diameter = 0.5 mm and surface area = 235 cm^2 (cut-off = 50 kDa for Flu-HA/chitosan NP and cut-off = 100 kDa for Flu-HA NP). Two cycles of filtration were performed. The obtained solution containing free Flz was then injected and analysed by HPLC according to the following method [117]:

1. Column = Discovery C_{18} Supelco, 150 mm x 4.6 mm, 5µm
2. Flux rate = 1 mL/min
3. Temperature = 25 °C
4. Injection volume = 20 µL
5. Detection λ = 210 nm
6. t_{run} = 10 minutes (t_{rit} = 2.9 minutes)
7. Mobile phase = 70% Water, 30% Acetonitrile

The analytical method was assessed in terms of linearity of response (Area Under the Curve, AUC, of the peak at 2.9 minutes *vs* concentration) in the concentration range 8 - 800 µg/mL *(Figure 66)*. Limit of Quantification (LOQ) and Limit of Detection (LOD), calculated

as reported in *paragraph 3.2.3* (*Eq. 2-3,* Chapter 1*)*, were 1.38 μg/mL and 0.457 μg/mL, respectively.

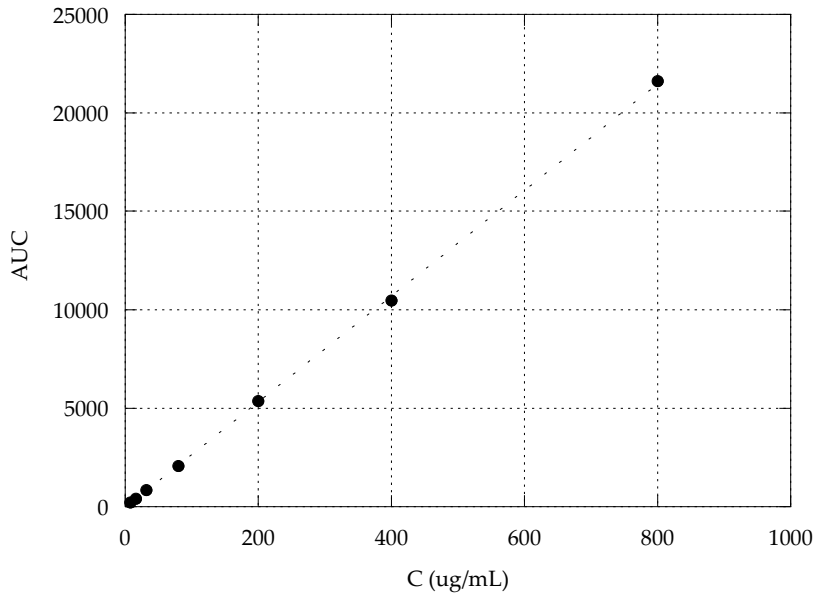

Figure 66. Calibration curve of Fluconazole: y = -60.111 + 26.927x, R^2 = 99976.

The amount of encapsulated drug was quantified indirectly according to the *Eq. 6* (Chapter 2, *paragraph 3.2.9*).

3.2.8 Powder redispersions

Powders were resuspended in diluted Hanks' Balanced Salt Solution (HBSS) at 0.5 and 1 mg/mL. Size and size distribution of released nanoparticles were assessed by DLS before and after 5, 15 and 30 minutes of sonication.

4. RESULTS AND DISCUSSION

4.1 Flz-loaded CS/HA nanoparticles

Two HA MW, 25 and 250 kDa, were compared in particles production, while CS was fixed at 252 kDa. Different concentrations of the two polymers were tested and combined as reported in *Table 31*, in order to obtain nanoparticles by ionic interaction of the positive-charged chitosan and the negative-charged hyaluronate.

Table 31. Size of NP obtained by combining different HA MW with CS 252 kDa at different concentrations.

<table>
<tr><th>HA 250 kDa</th><th>CS 252 kDa</th><th colspan="2">Size (nm)</th></tr>
<tr><td>0.1%</td><td rowspan="2">0.1%</td><td colspan="2" rowspan="5">Aggregates > 1 μm</td></tr>
<tr><td rowspan="2">0.25%</td></tr>
<tr><td rowspan="2">0.5%</td><td rowspan="2">0.5%</td></tr>
<tr><td rowspan="2">1%</td><td rowspan="2">1.0%</td></tr>
<tr><td></td></tr>
<tr><th>HA 25 kDa</th><th></th><th>Size (nm)</th><th>PdI</th></tr>
<tr><td>0.1%</td><td>0.1%</td><td>331.1</td><td>0.402</td></tr>
</table>

HA 250 kDa led always to the formation of visible aggregates at each concentration tested. In contrast, HA 25 kDa combined with CS, both at low concentrations, promoted the formation of particles with a hydrodynamic diameter around 330 nm and a quite high PdI value of 0.4. Given the significant influence of the length of polymeric chains on the dimension of particles, chitosan lactate at low molecular weight (40 kDa) was also tested. The aqueous solutions of both polymers were fixed at a concentration of 1% (w/v).

As reported in *Table 32*, nanoparticles with similar size around 350 nm were obtained employing HA 25 and 250 kDa. A higher polydispersion index was highlighted for the higher HA MW.

Table 32. Size and size distribution (PdI) of NP obtained by the combination of different HA MW with CS 40 kDa. Mean ± standard deviation (n = 3).

	CS 40 kDa	**Size (nm)**	**PdI**
HA 25 kDa	1%	346.6 ± 21.9	0.153 ± 0.022
HA 250 kDa	1%	357.7 ± 22.1	0.395 ± 0.009

In addition, nanoparticles obtained employing HA 250 kDa and CS 40 kDa presented a lower stability compared to the others, leading to phase separation after two days from preparation. For this reason, formulation with HA 25 kDa and CS 40 kDa was chosen for further step of drug loading. Fluconazole-containing NP were obtained as previously described, after solubilization of the drug in the chitosan solution. DLS measurements afforded a slight, although not statistically significant, increase of both size and size distribution of nanosuspensions (Size = 355 ± 8.6; PdI = 0.163 ± 0.006).

The encapsulation efficiency% was only of 49.3 ± 0.012%, somehow justifying the slight increase of size from blank to drug-loaded nanoparticles.

4.2 Flz-loaded HA nanoparticles

4.2.1 Dynamic Light Scattering

For fluconazole-containing HA NP production, a medium-low range of HA MW was employed, with an average molecular weight of 250 kDa. Two different approaches were investigated, based on the solubilization of the drug in ethanol or in water with HA, at a final concentration of 0.6 mg/mL. Drug-loaded nanoparticles were obtained as described

in *paragraph 3.2.2*. Nanoparticles analysed by DLS presented very similar hydrodynamic diameters and polydispersion, with a slightly higher PdI when fluconazole was in solution with HA (0.43 vs. 0.41) *(Table 33)*.

Table 33. Size and size distribution (PdI) of blank HA NP and Flz-HA NP obtained solubilizing the drug in water and in ethanol. Mean ± standard deviation (n = 3).

	Size (nm)	**PdI**
HA NP	134.4 ± 22.9	0.379 ± 0.129
Flz-HA NP (water)	197.1 ± 19.3	0.437 ± 0.027
Flz-HA NP (ethanol)	196.2 ± 14	0.410 ± 0.055

Compared to blank HA NP obtained at the same conditions, drug-loaded NP presented an increase of both size and size distribution. The amount of drug loaded into NP was similar for both approaches, with an average value of 98.8 ± 1.3%, thus justifying the increase of size observed for fluconazole-loaded NP.

For spray drying, the nanosuspension obtained by solubilizing the drug in water was employed. The size distributions of blank and Flz-loaded NP, determined by DLS, are reported in *Figure 67*. Results confirmed the slight increase of polydispersion for drug-loaded NP, with the appearance of a small tail around 20 nm, together with a small particle population above 1 μm.

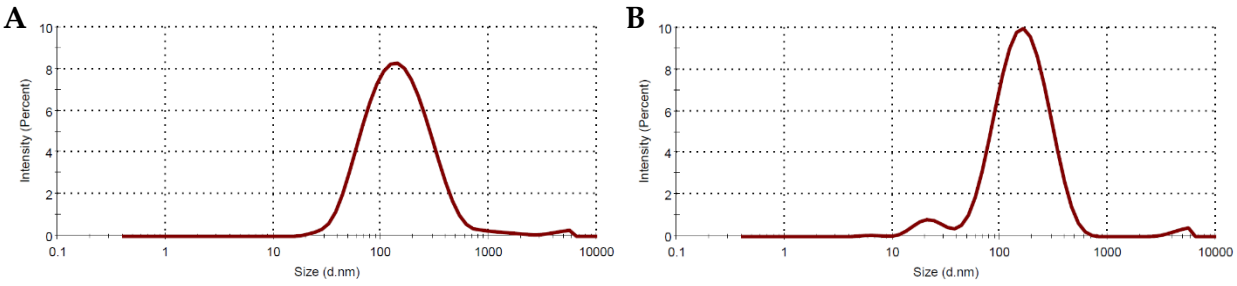

Figure 67. Size distribution of HA NP (Panel A) and Flz-loaded HA NP (Panel B) before SD.

4.2.2 Spray drying and powder characterization

Spray drying process presented a yield% of 62.3 ± 16.7%. The morphology of the powders was assessed by SEM, comparing blank and drug-loaded nano-embedded microparticles.

As it can be observed in *Figure 68*, HA powder presented particles with smooth surface and quite spherical shape. The slight collapses appreciable in each particle could be due to an effect of the electron beam on the sample.

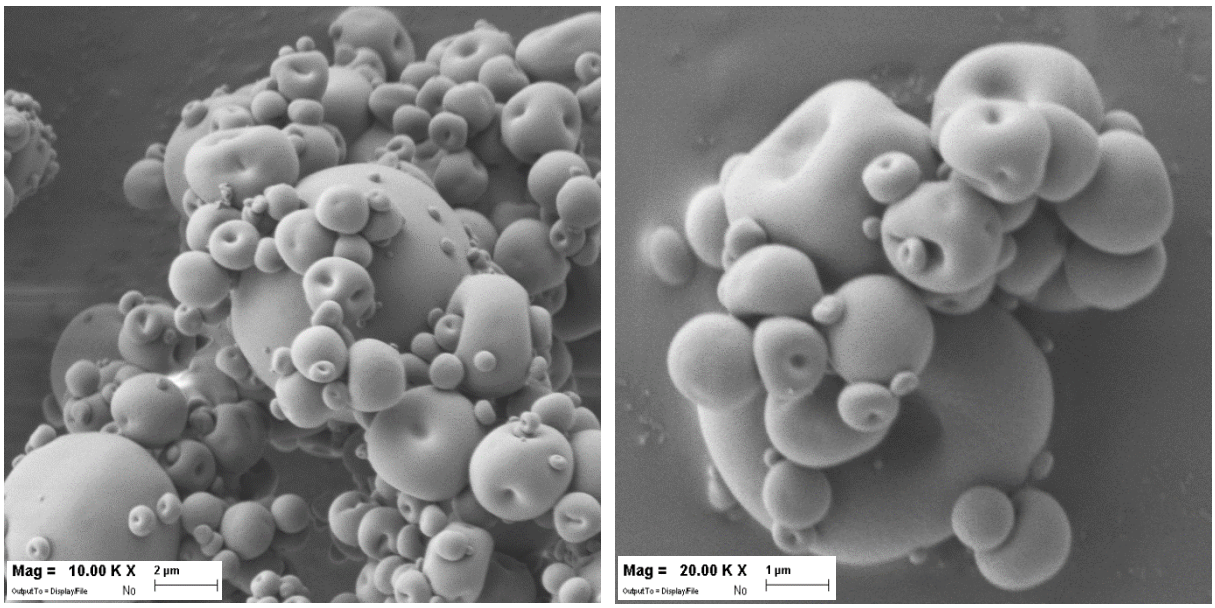

Figure 68. Morphology of powder containing HA NP.

In contrast, powder containing drug-loaded nanoparticles *(Figure 69)*, presented particles with irregular shapes, including spherical, collapsed and needle-like particles. In addition, the surface appeared more corrugate and wrinkled. These differences were found also by Rivera and colleagues, that produced Fluconazole-loaded PLGA microparticles by spray drying [118]. The authors observed the production of spherical microparticles with smooth surfaces at a low drug content. While, with the increase of the nominal drug loading, particles become deformed, less spherical and with needle-like crystals of fluconazole.

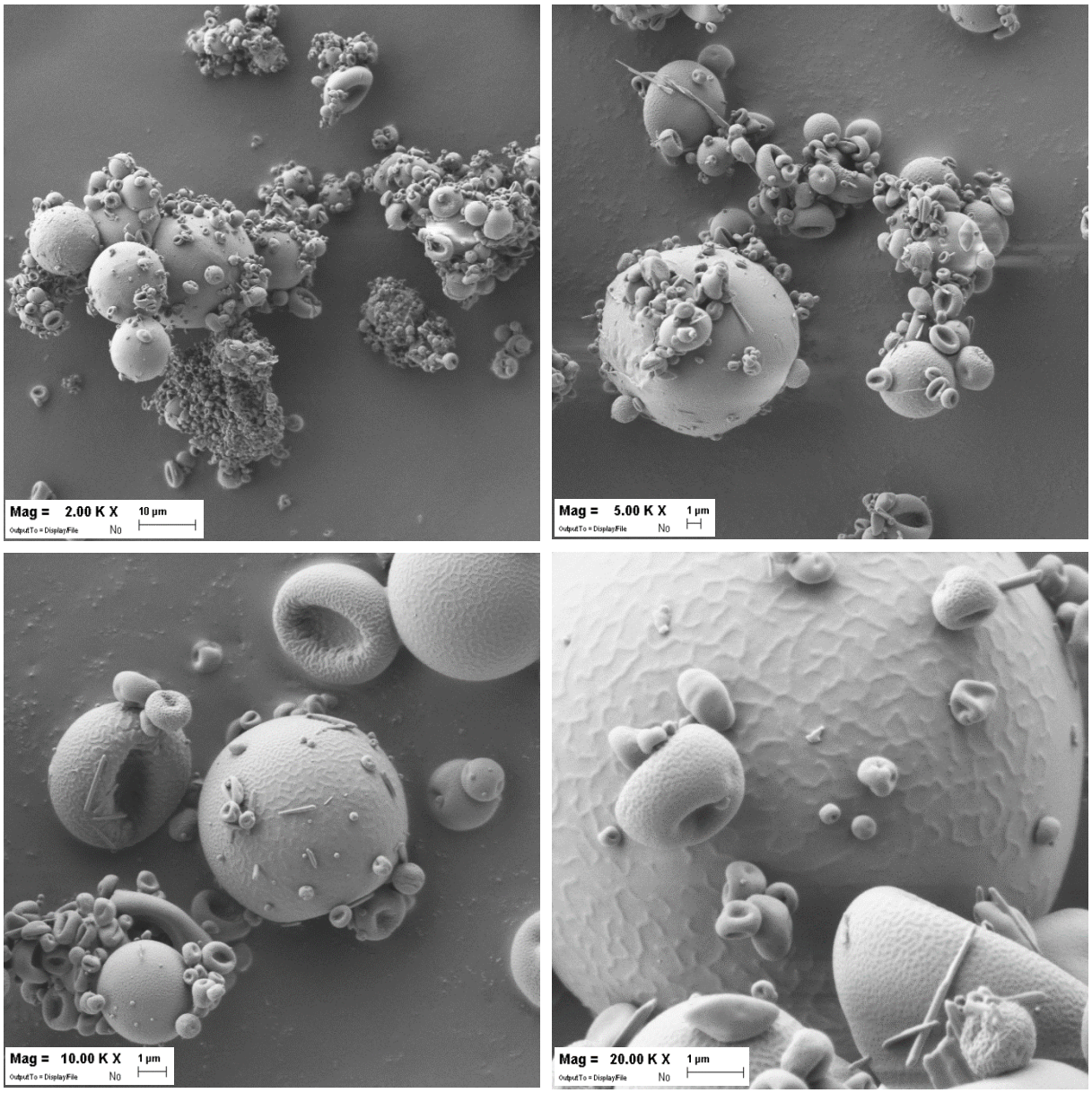

Figure 69. Morphology of powder containing Flz-HA NP.

4.2.3 Laser Diffraction

The volume-weighted diameters of microparticles obtained by laser diffraction are reported in *Table 34*. Powders presented some differences, with an increase of both $D_v(50)$ and $D_v(90)$ when Flz was loaded in the nanoparticles.

Table 34. Volume-weighted diameters of HA and Flz/HA microparticles. Mean ± standard deviation (n = 3).

	$D_v(10)$	$D_v(50)$	$D_v(90)$
HA (μm)	1.88 ± 0.05	4.37 ± 0.08	15.17 ± 1.07
Flz-HA (μm)	1.30 ± 0.09	7.08 ± 0.49	18.50 ± 1.46

The differences between blank and drug-loaded powders were appreciable also in the graphs reported in *Figures 70* and *71*, that presented a tail in particle distribution at higher and lower values, respectively.

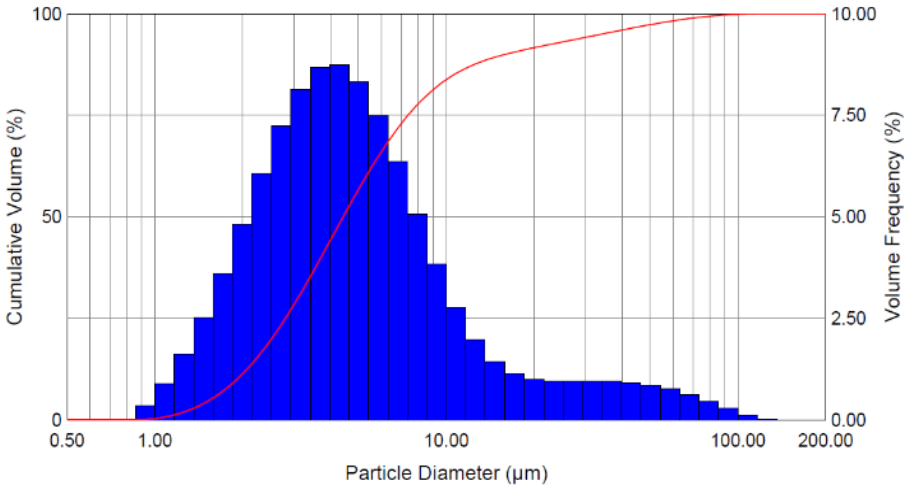

Figure 70. Frequency and cumulative size distribution of HA powder.

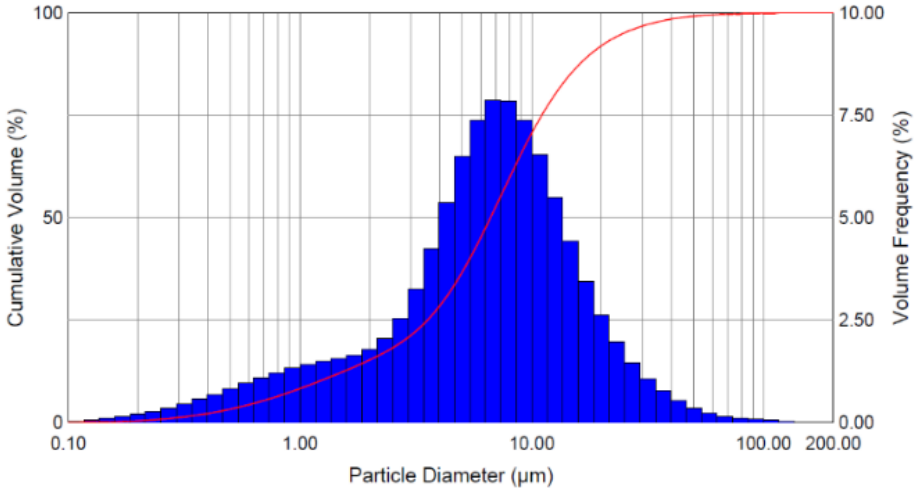

Figure 71. Frequency and cumulative size distribution of Flz-HA powder.

These results are confirmed by the pictures acquired by SEM, that highlighted the presence of bigger particles with smaller needles attached on the surface in powders containing Flz-HA nanoparticles.

4.2.4 Powder redispersion

Powder containing Flz-HA nanoparticles was redispersed in HBSS medium at 0.5 and 1 mg/mL to assess nanoparticles release after 5 minutes under magnetic stirring (corresponding to 0 min of sonication in *Tables 35* and *36*) and after 5, 15 and 30 minutes of sonication.

Table 35. Size, size distribution (PdI) and Z-potential (ζ) of NP redispersed at 1 mg/mL after 5 min under stirring (0 min of sonication) and after 5, 15 and 30 min of sonication. Mean ± standard deviation (n = 3).

t (min)	Size (nm)	PdI	ζ (mV)
0	354.2 ± 105.2	0.814 ± 0.081	-41.2 ± 2.2
5	415.4 ± 207.6	0.503 ± 0.026	-45.3 ± 1.1
15	414.3 ± 103.1	0.567 ± 0.029	-42.4 ± 1.9
30	435.2 ± 19.8	0.662 ± 0.163	-40.6 ± 2.4

Compared to nanoparticles before spray drying (196.2 ± 14 nm; PdI = 0.410 ± 0.055), bigger particles were released after redispersion at both concentrations *(Tables 35* and *36).*

Table 36. Size, size distribution (PdI) and Z-potential (ζ) of NP redispersed at 0.5 mg/mL after 5 min under stirring (0 min of sonication) and after 5, 15 and 30 min of sonication. Mean ± standard deviation (n = 3).

t (min)	Size (nm)	PdI	ζ (mV)
0	257.5 ± 61.7	0.734 ± 0.095	-41.0 ± 6.2
5	270.9 ± 53.4	0.524 ± 0.09	-39.9 ± 7.3
15	293 ± 109.9	0.461 ± 0.049	-44.4 ± 9
30	232.9 ± 29.5	0.509 ± 0.099	-39.4 ± 7.9

Nevertheless, the increase of particles size was lower at 0.5 mg/mL, with the release of particles of 250 nm in diameters after only 5 minutes under stirring. Sonication did not impact on particle size, even after 30 minutes, with quite stable hydrodynamic diameters at both concentrations. These results suggest a good redispersion of microparticles into nanoparticles after contact with aqueous medium, even if with quite high polydispersion.

Redispersed nanoparticles presented similar surface charge, with quite stable negative Z-potential around -40 mV at both concentrations. This observation suggests the presence of HA chains on the outer surface of released particles.

5. CONCLUSIONS

The aim of the present chapter of the thesis was to develop fluconazole-loaded HA nanoparticles to target alveolar macrophages through CD44 binding. For this purpose, two methods for particle production were developed.

The first method, consisting in HA-CS ionic gelation, based on mixing polymeric aqueous solutions at 1% (w/v) with polymers at low MW (HA 25 kDa and CS 40 kDa). This method led to the formation of blank and drug-loaded nanoparticles around 350 nm in size and a quite low value of EE%, amounting to 49%.

The second method based on the anti-solvent precipitation of HA with ethanol, employing a medium-low MW range of 130-300 kDa. Blank nanoparticles of 135 nm in diameter were obtained, with an increase to 200 nm for Flz-loaded NP. Nanosuspensions presented a quite high polydispersion with PdI value around 0.4 but a successful drug encapsulation with an EE% = 98%.

Nano-embedded microparticles were obtained by spray drying starting from the blank and Flz-loaded HA nanosuspensions. Powders presented differences both in size and morphology, with higher $D_v(50)$, amounting to 7 μm, and irregular shapes for particles containing fluconazole. After redispersion in aqueous medium, nanoparticles were released after 5 minutes under stirring, without significant changes in size with sonication. Particles around 250 nm were released at 0.5 mg/mL and around 400 nm at 1 mg/mL, highlighting a slight aggregation during spray drying positively influenced by dilution. Negative surface around -40 mV was measured at both concentrations, suggesting the presence of polymeric chains on the outer surface of nanoparticles, potentially able to enhance particle presentation and to bind alveolar macrophages through CD44 receptor.

CHAPTER 4

Sodium hyaluronate microparticles for dexamethasone pulmonary delivery

1. INTRODUCTION

1.1 Dexamethasone

1.1.1 General aspects

Dexamethasone (DX) is a potent steroid molecule (*Figure 72*, [119]) belonging to the glucocorticoid class and available as tablets, injectable suspension and oral solution.

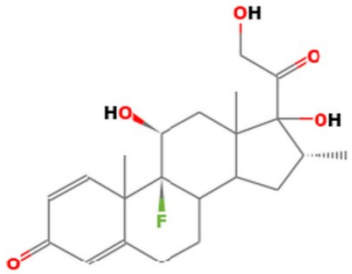

Figure 72. Chemical structure of dexamethasone [119].

As anti-inflammatory and immunosuppressant, it has a wide variety of uses in the medical field, in particular in the treatment of acute exacerbation of multiple sclerosis, allergies, cerebral edema, inflammation, shock and chronic obstructive lung disease. It is employed also in conditions such as asthma, atopic and contact dermatitis and drug hypersensitivity reactions. Off-label indications are for the treatment of chemotherapy-induced nausea and vomiting and for the treatment of spinal cord compression due to metastases in oncological cases [120].

The mechanism of action of dexamethasone depends on the dose, in particular with genomic and nongenomic mechanisms in case of low and high doses, respectively. At high doses of the medication, dexamethasone binds to the membrane-associated GR on cells, such as T lymphocytes, leading to the activation of FAK (focal adhesion kinase). A high dose of dexamethasone also interacts with the movement of Ca^{2+} and Na^{+} across the cell membrane, resulting in a rapid decrease in inflammation state. But more importantly, most effects of dexamethasone are via the genomic mechanism which require a longer

period and lower doses. Being small and lipophilic substance, dexamethasone can easily pass through the cell membrane by diffusion and enter the cytoplasm by binding the glucocorticoid receptor on the cell membrane. The formation of this complex leads to translocation of the corticosteroid into the cell, and then to the nucleus. Here, it reversibly binds to several specific DNA sites resulting in stimulation of anti-inflammatory cytokine synthesis, notably IL-10 and lipocortin-1, and suppression of genes of pro-inflammatory cytokines such as interleukin IL-1, IL-2, IL-6, IL-8, TNF, IFN-γ, VEGF and prostaglandins [121]. Importantly, most of them are linked to SARS-CoV-2 severity [122]. For this reason, the employment of dexamethasone in COVID-19 patients has been deeply investigated and several studies have demonstrated its usefulness in treating COVID-19 disease [123].

1.1.2 Dexamethasone for treatment of COVID-19-related acute respiratory distress syndrome

COVID-19 disease, caused by SARS-CoV-2 infection, is characterized by 3 different stages (*Figure 73*):

- **Phase I**: it occurs at the time of inoculation and the initial introduction of the disease. Patients begin to show nonspecific symptoms (most commonly a dry cough and fever). During this period, the virus multiplies and establishes residence in the host tissues by binding to the ACE-2 receptor in cells, with the respiratory system being primarily affected. The immune system is simultaneously attempting to expel it from the lungs, and, in some cases, causing immune-mediated damage of the pulmonary structures.
- **Phase II**: it is caused by the uncontrolled replication of the virus. This process is driven by the direct cytotoxicity of ACE-2 which acts as a catalyst for further activation of the immune system and therefore worsens the hyperinflammatory state. In addition to the other symptoms, patients begin to demonstrate severe hypoxemia.
- **Phase III**: granulocyte colony-stimulating factor, inflammatory cytokines and biomarkers such as IL-2, IL-6, IL-7 and TNF-α, C-reactive protein and ferritin are

elevated in patients who are critically ill. During this phase, patients are susceptible to developing shock, respiratory failure and even cardiopulmonary collapse [124][125].

Several clinical studies have been carried out to investigate the efficacy of dexamethasone in the treatment of COVID-19 disease. Among them, the largest one, called RECOVERY (Randomised Evaluation of COVID-19 Therapy), was carried out in UK in more than 170 National Health Service organizations. The trial highlighted the benefits of administering 6 mg/day dexamethasone orally or intravenously to hospitalized patients in Phase III, aiming to treat the COVID-19-related acute respiratory distress syndrome *(Figure 73).*

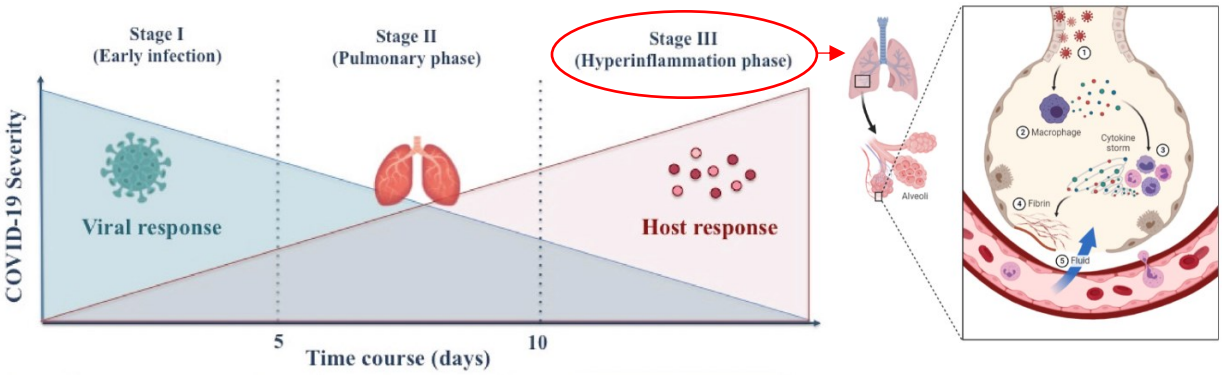

Figure 73. Phases of COVID-19 disease. Modified with permission from BioRender® and [124].

In particular, the trial revealed as primary outcome a reduction of 28 day-mortality in patients receiving oxygen and invasive mechanical ventilation (20% and 35%, respectively) but not in those receiving no respiratory support [126].

However, despite its highly potent therapeutic efficacy, long-term administration of corticosteroid has been hampered by the systemic side effects, such as renal failure, low blood pressure, weight loss and vision impairment. In this context, there have been growing needs to develop a strategy to fully realize therapeutic potential of corticosteroid, while reducing its systemic side effects. The proposal to employ dexamethasone

nanomedicines for treating COVID-19 was widely described thanks to the potential of nanoparticles to accumulate in inflammation phagocytic cells in the lung, upon intravenous administration as well as inhalation. Pulmonary route, in fact, could promote the targeted accumulation of the drug in inflammatory alveolar macrophages infiltrated at the pathological site avoiding the rapid capture by the liver- and spleen-resident macrophage populations that are responsible for clearing nanomedicine formulations from the blood stream [127]. Therefore, if the drug carrier is designed to exert intrinsic anti-inflammatory activity and to synergize with drug payload, the dose of drug and drug carrier could be significantly reduced and consequently their side effects could be avoided [128]. Sodium hyaluronate HMW presents potential anti-inflammatory effects that could be exploited for this purpose.

2. AIM

The aim of the present part of the thesis was to develop dexamethasone (DX) nano-embedded HA microparticles for the treatment of acute respiratory distress syndrome. Sodium hyaluronate with proper molecular weight was chosen to exploit both its technological role in particle production as well as its anti-inflammatory effect.

Precipitation of dexamethasone-HA nanoparticles was assessed by dynamic light scattering. Powders for inhalation were then obtained by spray drying starting from DX and DX-HA nanosuspensions, and then characterized by scanning electron microscopy and laser diffraction. SAXS/WAXS analyses were performed to investigate the internal structure of nanoparticles and their stability in contact with mucin. Aerodynamic performance of DX-HA powder aerosolized using a dry powder inhaler was compared to a device for aerosol therapy and assessed *in vitro* with a next generation impactor.

3. MATERIALS AND METHODS

3.1 MATERIALS

Sodium hyaluronate 750-1000 kDa was obtained by *Contipro* (Czech Republic) and dexamethasone by *Metapharmaceutical* (Spain). Mucin from porcine stomach (Type III, bound sialic acid 0.5-1%) was purchased from *Sigma-Aldrich* (U.S.A). Ultrapure water was purified by reverse osmosis with Purelab Pulse flex, *Elga-Veolia* (Italy). Ethanol, cyclohexane and acetonitrile were of analytical grade.

3.2 METHODS

3.2.1 Preparation of DX-HA nanoparticles

DX nanoparticles were obtained by anti-solvent precipitation using water as anti-solvent, added dropwise to an alcoholic solution of drug at 5 mg/mL. 180 mg of dexamethasone was first dissolved in 36 mL of ethanol and 29.5 mL of water was added dropwise to the alcoholic solution to promote drug precipitation. The anti-solvent was added manually, dripping 7 mL of water at a time and leaving 3 min of rest between each addition. During the precipitation, the temperature was maintained at 25°C using a thermostatic bath and the suspension was kept under magnetic stirring at 165 rpm. Separately, 220 mg of sodium hyaluronate 750-1000 kDa was dissolved in 14.5 mL of ultrapure water and then added in one shot to the dexamethasone nanosuspension, reaching the final anti-solvent concentration of 55% (v/v). The nanosuspension was left at room temperature under stirring at 280 rpm for 30 min before spray drying *(Figure 74)*. To produce dexamethasone nanoparticles without the addition of sodium hyaluronate, the same procedure was followed, but 14.5 mL of ultrapure water was added in one shot to the drug nanosuspension without previously solubilizing the polymer.

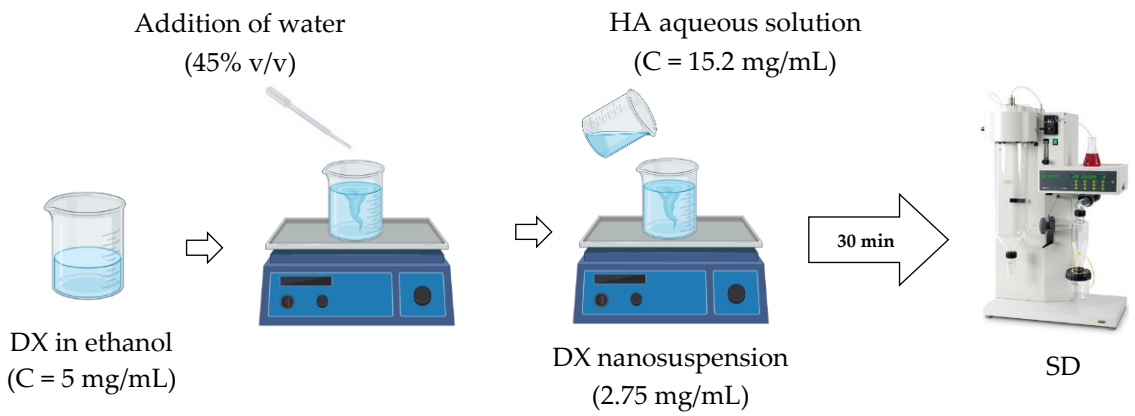

Figure 74. Graphic representation of preparation of DX-HA particles.

3.2.2 Nanoparticle characterization

Static and dynamic laser light scattering experiments (SLS and DLS, respectively) were performed on a home-made apparatus, equipped with a Nd-Yag laser source (532 nm) and four independent photomultipliers at 90°. All samples were submitted to parallel and independent SLS and DLS measurements at 25°C. The mean scattered intensity was acquired for the nanoparticle solutions and for HA solutions in a dilute regime along a dilution line (1:2 1:4 1:8 with respect to the original formulations 0.1% w/v) to check for the presence of inter-particle interaction. Parallel acquisition of the intensity correlation function by DLS gave their hydrodynamic diameter. The concentration range of dispersions analysed was 0.125 - 1 mg/mL.

Z-potential (ζ) of nanoparticles in suspension was measured with ZetaPlus and ZetaPals analyzer (*Brookhaven Instruments*, USA). The analyses were performed both in salt-free and PB solution suspensions at 25°C. Five measurements were carried out and averaged to obtain a mean value.

3.2.3 Small and Wide-Angle X-ray Scattering

Small- and wide-angle X-ray scattering (SAXS and WAXS) experiments were performed

on the ID02 beamline at ESRF (Grenoble, France) and on the SAXS beamline at ELETTRA (Trieste, Italy). The configuration with a flow-through cell was selected, which allowed the measurements of the samples and of the reference in identical conditions. The scattered intensity was acquired in the q range $7.10^{-2} \leq q \leq 0.7$ $Å^{-1}$ for SAXS and $1 \leq q \leq 2$ $Å^{-1}$ for WAXS. Ten short frames (0.1 s ESRF, 1 s ELETTRA) were acquired and averaged, after check, to avoid any radiation damage. After data normalization and correction, the cell and solvent contributions were subtracted from each spectrum to obtain the excess scattered intensity in absolute units I(q), mm^{-1}.

Data analysis was performed using SasView 4.2.1 software.

3.2.4 Spray Drying

DX and DX/HA nanosuspensions were dried using a Mini Spray Dryer B-290 (*Büchi*, Switzerland) connected with an Inert loop B-295 for organic solvents. The processes were carried out in N_2 at the following conditions:

1. Needle diameter = 0.7 mm
2. T_{inlet} = 100° C (T_{outlet} recorded = 68°C)
3. Aspiration = 35 m^3/h (100%)
4. Nitrogen flux = 473 L/h (40 mm)
5. Feed rate = 2 mL/min (7%)
6. T_{cond} = 10° C

The yield% of the process was calculated according to the *Eq. 5* (Chapter 2, *paragraph 3.2.4*).

3.2.5 Laser Diffraction

Analyses by laser diffraction were performed as described in *paragraph 3.2.6*, Chapter 2. Samples were sonicated for 5 minutes before measurements to improve their homogeneity.

Data were expressed in terms of volume-weighted diameter (D_v) for 10th, 50th and 90th percentiles, corresponding to $D_v(10)$, $D_v(50)$, and $D_v(90)$ respectively.

3.2.6 Scanning Electron Microscopy

Morphology of powders obtained by spray drying was analysed by scanning electron microscopy (SEM) with FESEM SUPRA™ 40 microscope (*Carl Zeiss*, Germany) at different magnifications (1k, 10k and 20k X). Samples were prepared as described in *paragraph 3.2.7*, Chapter 2.

3.2.7 High Pressure Liquid Chromatography: Drug content and Encapsulation efficiency

The drug content in the powder was assessed by liquid chromatography using an HPLC Agilent technologies 1200 (*Agilent*, USA). Powder was solubilized in a mixture of ethanol:water 30:70 (v/v) at 0.5 mg/mL and sonicated for 15 minutes. Samples were analysed by HPLC according to the following method, which represents a modification of the one proposed in the European Pharmacopeia [129]:

1. Column = C_{18}, 150 mm x 4.6 mm, 5μm
2. Flux rate = 1.2 mL/min
3. Temperature = 45 °C
4. t_{run} = 12 minutes (t_{rit} = 2.7 minutes)
5. Injection volume = 20 μL
6. λ = 254 nm
7. Mobile phase = water/acetonitrile (ACN) mixture in gradient:
   - 0 - 2.7 min ACN 40%
   - 2.7 - 2.8 min ACN 100%
   - 2.8 - 10 min ACN 100%
   - 10 - 12 min ACN 40%

The analytical method was assessed in terms of linearity of response (Area Under the Curve, AUC, of the peak at 2.7 minutes *vs* concentration) in the concentration range 2.5 - 500 μg/mL *(Figure 75)*.

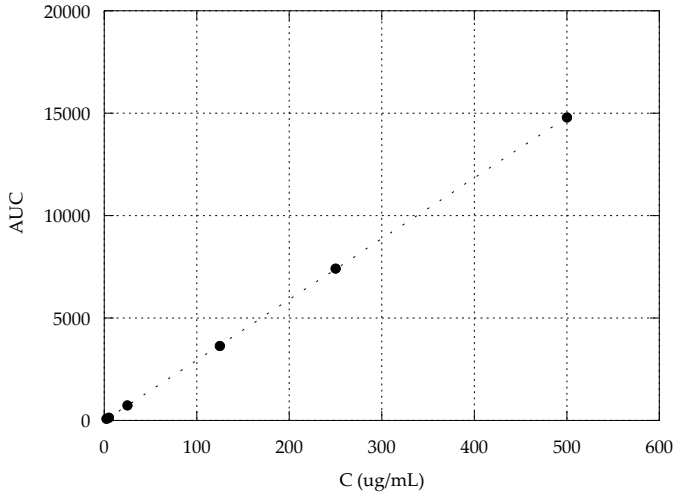

Figure 75. Calibration curve of dexamethasone in ethanol 30% (v/v): y = -16.235 + 29.629x, R^2 = 0.99998.

Limit of Quantification (LOQ) and Limit of Detection (LOD), calculated as reported in *paragraph 3.2.3* (*Eq. 2-3*, Chapter 1*)*, were 0.239 μg/mL and 0.0788 μg/mL, respectively. Stock solution of DX at 500 μg/mL was first sonicated for 15 minutes before performing dilutions for the calibration curve.

3.2.8 Powder redispersion

Powders were redispersed and analysed at the concentration range of 2.5 - 20 mg/mL, in water and in phosphate buffer (PB) pH = 7.4. PB was prepared as indicated in European Pharmacopeia from an aqueous solution of KH_2PO_4 200 mM and NaOH 100 mM (*Sigma-Aldrich*, U.S.A). The solution pH was adjusted to 7.4 with NaOH.

3.2.9 Aerodynamic performance

For the test of aerosolization *in vitro* by nebulization, 10 mg of powder were resuspended in 4 mL of ultrapure water to obtain a final concentration of 2.5 mg/mL. The suspension

was sonicated for 15 min and loaded into the ampoule. As a nebulizing device, a PARI LC-Sprint ampoule and the compressor PARI Turbo Boy (*Pari*, Germany) were used. The air flow of the device was fixed at 20 L/min and the compressor was activated 30s after switching on the aspiration that was set at 15 L/min. The nebulization was carried out until sputtering (about 16 min) and at the end of the aerosolization the aspiration was stopped 5s after the shut-down of the compressor. The nebulizer was connected through a rubber adaptor to a Next Generation Impactor (*Copley Scientific*, UK) composed of seven stages. After nebulization the ampoule, the induction port (IP), the rubber adaptor, the 7 stages and the micro-orifice collector (MOC) were washed with 5 mL of ethanol-water (30:70 v/v) and the collected solutions were sonicated for 15 min. Before HPLC injections, MOC-solution was filtered with a cellulose acetate filter with a cut-off of 0.45 μm (*Sartorius*, Germany).

For the tests of aerosolization *in vitro* of the dry powder, 10 mg were loaded into a V-Caps® (*Capsugel*, Switzerland) of hydroxy propyl-methylcellulose, size 3, and then located into a RS01® inhaler (*Plastiape*, Italy). The device was connected using a rubber adaptor to the NGI composed of seven stages, pre-treated with an alcoholic solution of Tween 20 at 2% to avoid particle bouncing. The aerosolization was carried out for 4s at an air flow of 60 L/min. The device and the capsule, the IP and the rubber adaptor, the 7 stages and the MOC were washed after the aerosolization with 5 ml of ethanol 30% and the collected solutions were sonicated for 15 minutes. Before HPLC injection, MOC and capsule/device solutions were filtered with a cellulose acetate filter with a cut-off of 0.45 μm *(Figure 76)*.

Figure 76. Schematic representation of in vitro aerosolization.

Mass median aerodynamic diameter (MMAD) and Geometric standard deviation (GSD) values were obtained by plotting in ordinate on probit scale the cumulative undersize percentage of drug collected and in abscissa the logarithm of cut-off values for each stage at 15 L/min and 60 L/min (for nebulization and DPI, respectively). MMAD is the value corresponding to the 50% mass distribution in the log-probit plot; GSD is the value corresponding to the square root of the ratio between the diameters when the cumulative mass is equal to 85% and 15%. The emitted dose (ED) was obtained by the sum of dexamethasone collected from the IP to the MOC of the NGI, while the emitted fraction (EF%) was calculated as percentage of the ED on the total amount of drug recovered at the end of the aerosolization. The fine particle dose (FPD), the amount of drug with an aerodynamic diameter below 5 μm, was obtained by the sum of drug collected from stage 3 or stage 2 (for nebulization and DPI, respectively) to the MOC of the NGI, while the respective fine particle fraction (FPF%) was calculated as the percentage of the FPD on the ED.

4. RISULTS AND DISCUSSION

4.1 Particle characterization

4.1.1 Preparation of nanoparticles

All data reported in this chapter concerning nanoparticle characterization were collected in collaboration with colleagues from the University of Milan, Department of Medical Biotechnology and Translational Medicine, who took care in particular of the SAXS and WAXS analysis as well as of laser light scattering experiments [130].

DX NP with hydrodynamic diameter of 356.3 ± 96 nm and PdI = 0.289 ± 0.134 were detected by DLS before the addition of the polymeric solution. Nevertheless, SAXS/WAXS spectra obtained from DX-HA nanosuspension (ethanol:water, 45:55 v/v and HA:DX, 55:45 w/w; 5 mg/mL) before spray drying, revealed that DX was molecularly dispersed in the solution, since no crystalline diffraction patterns were observed in the spectra *(Figure 77).* The single broad correlation peak present in SAXS spectrum was probably due to the spatial arrangement of HA chains [131].

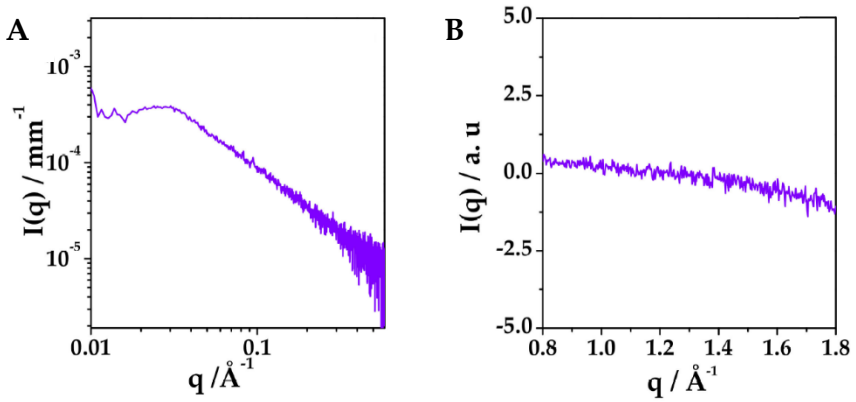

Figure 77. SAXS (Panel A) and WAXS (Panel B) spectra of DX-HA nanosuspension.

These results revealed the dissolution of DX nanoparticles after the addition of HA, probably due to the high affinity of HA for water, able to subtract DX anti-solvent and to promote the solubilization of the drug in ethanol.

4.1.2 Spray drying and powder characterization

The yield% of the process of spray drying was 32.9 ± 2.1% (w/w).

Particle size distribution of SD microparticles was assessed by laser diffraction. The analyses revealed a relatively wide size distribution of DX-HA microparticles *(Figure 78, Panel A)* with a $D_v(50)$ around 11 µm and a small population below 1 µm. On the contrary, powder obtained without the addition of the polymer presented a narrow size distribution *(Panel B)* with smaller microparticles, with Dv(90) around 6 µm and Dv(50) = 2.8 µm *(Table 37)*.

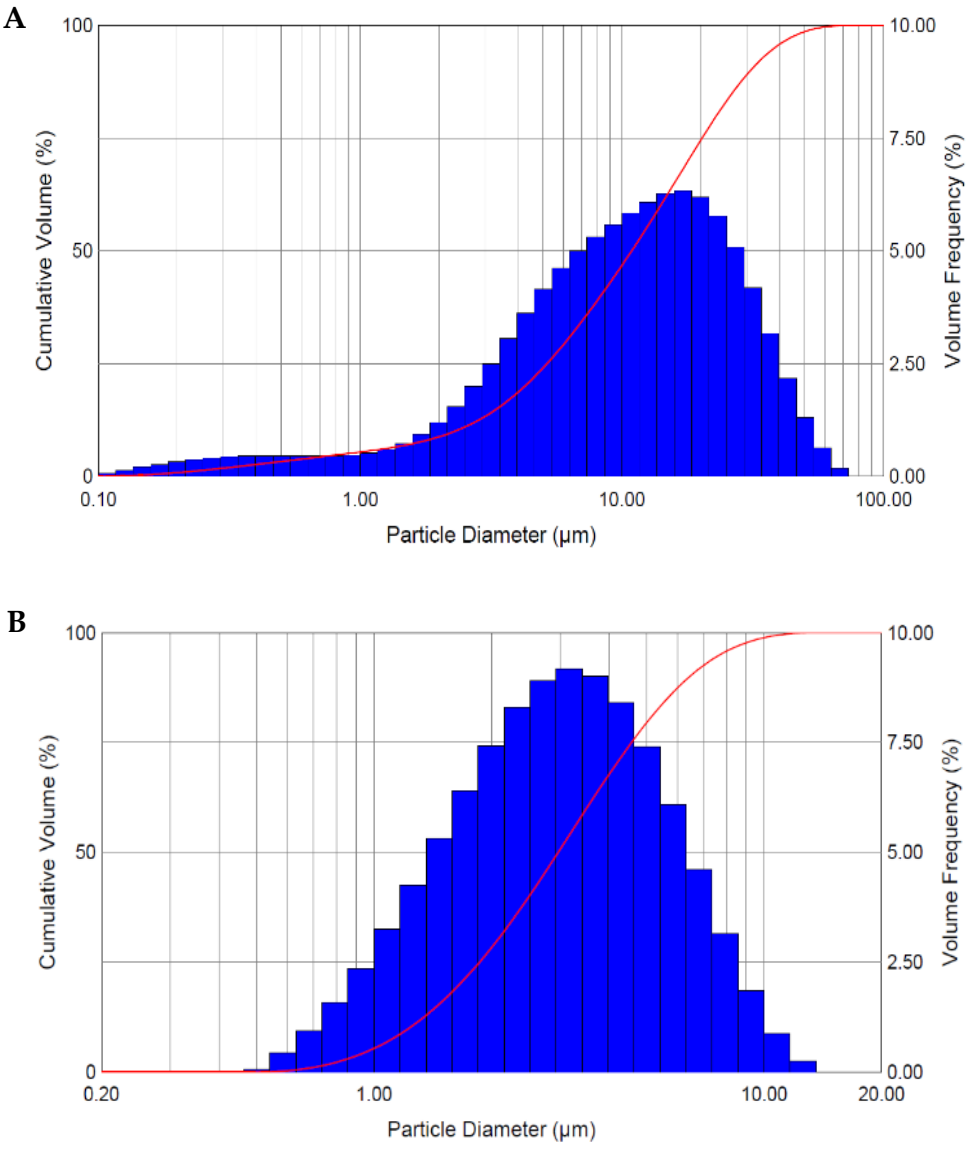

Figure 78. Frequency and cumulative size distribution of microparticles containing DX-HA (Panel A) and DX NP (Panel B).

Table 37. Volume-weighted diameters of microparticles at 10th, 50th and 90th percentiles obtained from the cumulative curve of spray-dried powders containing DX and DX + HA. Mean ± standard deviation (n = 3).

Size (μm)	DX + HA	DX
D_v(10)	2.5 ± 0.1	1.19 ± 0.06
D_v(50)	11.2 ± 0.2	2.8 ± 0.2
D_v(90)	31.7 ± 0.6	6.3 ± 0.2

The morphology of the powders was observed by scanning electron microscopy and reported in *Figures 79* and *80*.

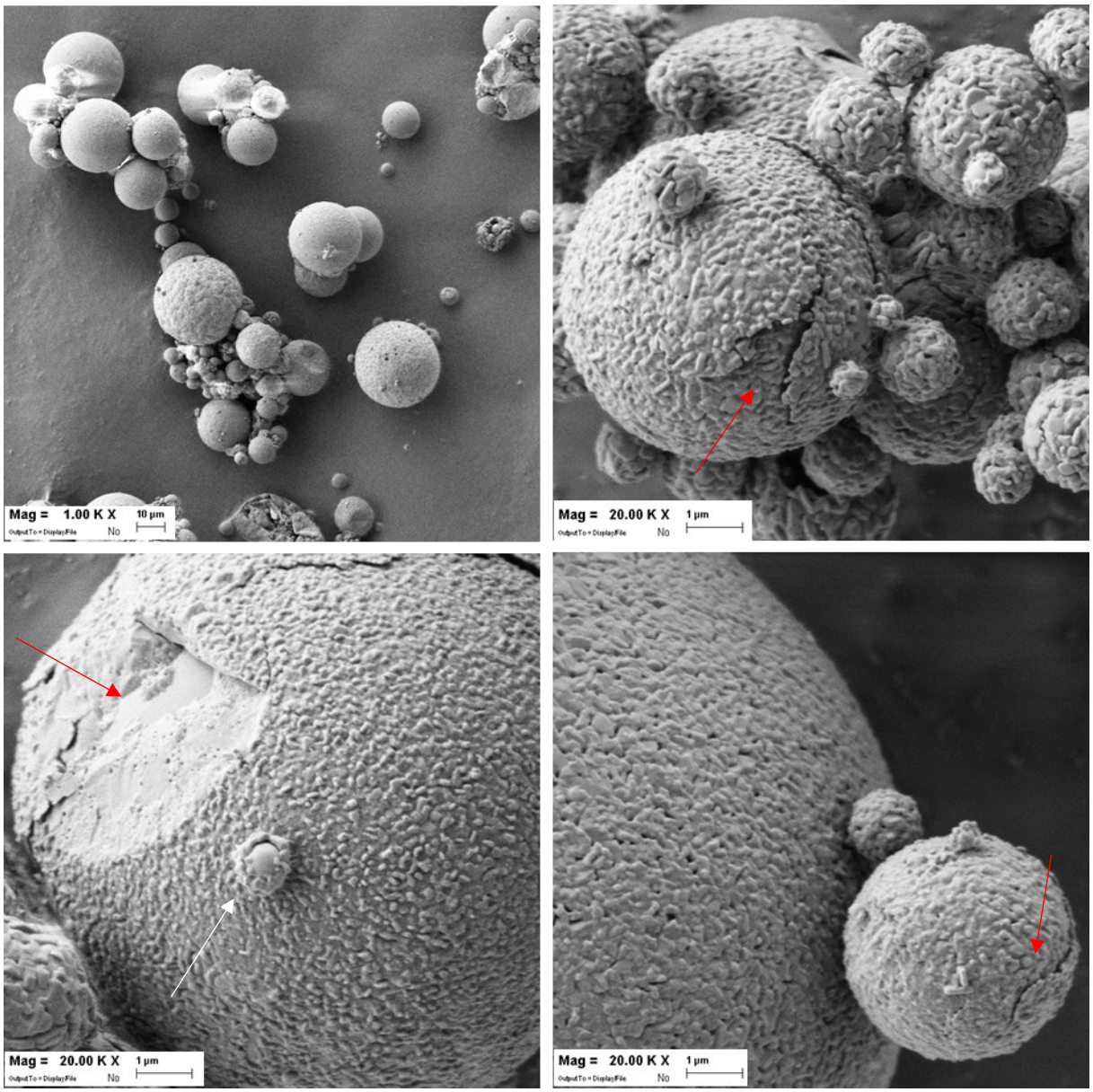

Figure 79. Morphology of DX-HA microparticles.

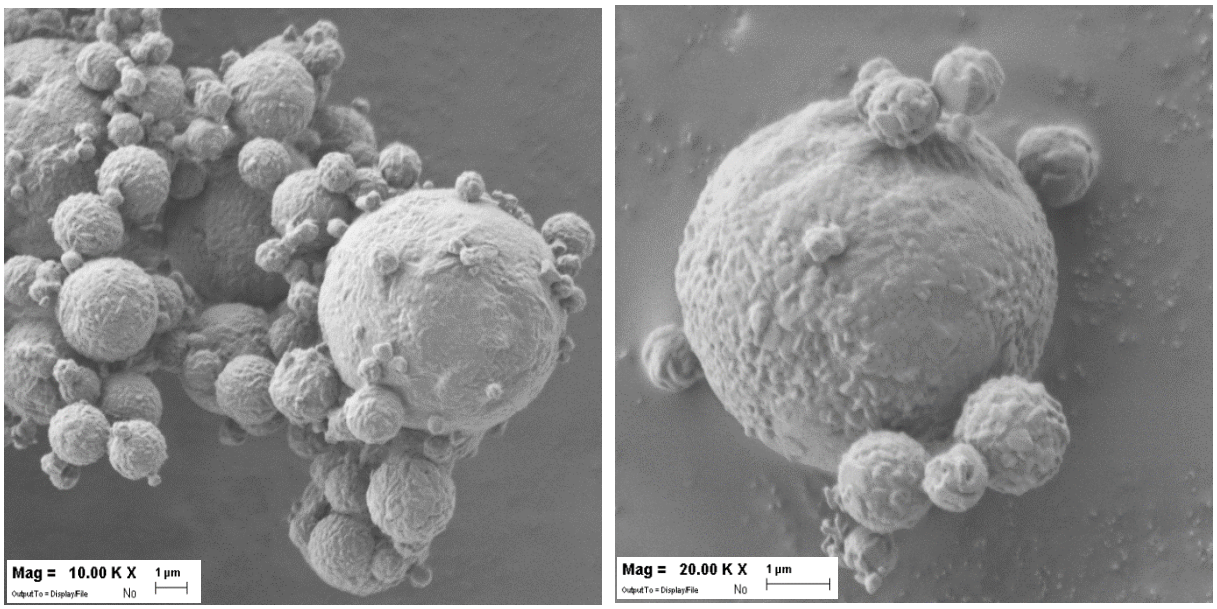

Figure 80. Morphology of DX microparticles.

Pictures acquired on DX-HA powder *(Figure 79)* confirmed the size distribution of microparticles previously measured by laser diffraction, displaying spherical particles around 10 µm clearly appreciable at lower magnification. Microparticles presented a very peculiar morphology characterized by wrinkled surface bread-crust looking and some cracks that revealed the coating on a smoother surface *(red arrows)*. This effect was present in bigger as well in smaller particles, as it is possible to observe in the particle evidenced by the *white arrow*. In contrast, DX-containing powder *(Figure 80)* presented particles more homogeneous in size and with a wrinkled surface at much lower extent and without cracks.

Based on these data, it can be hypothesized that particles are formed by nano-sized DX core surrounded by a HA shell. This structure is justified also from a technological point of view, since during the drying process, ethanol evaporates faster than water, thus leading to the nanoprecipitation of DX. Therefore, the slower evaporation of water determines the deposition of HA chains on and among the drug cores, as well as the outer surface of microparticles forming a polymeric coating.

The drug content of the powder, quantified by HPLC, revealed a lower amount of drug of 34.3 ± 0.5% (w/w) compared to the nominal one of 45% (w/w). This founding could be

explained by the loss of the very small drug particles during the drying process due to their transport by the gas aspiration into the filter of the spray dryer apparatus before HA deposition, that leads to an increase of their size. All considered, it can be calculated a loading capacity of about 35% and a loading efficiency slightly higher than 76%.

4.1.3 Particle redispersion

The release of nanoparticles from microparticles was assessed in water and in buffer phosphate (PB) by DLS and X-ray scattering techniques at different concentrations. For particles at higher concentrations in water, the viscosity was corrected (2.5 cP at 1 mg/mL and 1.2 cP at 0.5 mg/mL) due to the contribution of hyaluronan [132]. All samples presented release of nanoparticles with size around 280 - 300 nm in water and 170 - 200 nm in PB, and a quite high polydispersity, with a PdI value between 0.3 - 0.4 *(Table 38)*. In addition, a small fraction of aggregates in the micrometre range was always present, due to the lack of deaggregation of some microparticles. The larger hydrodynamic size observed in salt-free water could be due to a different, more stretched, arrangement of HA polymer chains protruding from the surface of the nanoparticles into the surrounding solvent. Z-potential values were negative for each sample, in the range -20 - -30 mV in PB, while below -50 mV at zero ionic strength (water) *(Table 38)*.

*Table 38. Hydrodynamic diameter and Z- potential (ζ) of NP measured by DLS at different concentrations in water and PB (corrected viscosity at * 1.2 cps, ** 2.5 cps). Mean ± standard deviation (n = 5).*

C_{NP} (mg/mL)	**Water**		**PB**	
	Size (nm)	**ζ (mV)**	**Size (nm)**	**ζ (mV)**
0.125	280	-61 ± 4	210	-28 ± 5
0.25	290	-60 ± 3	170	-22 ± 6
0.5	280 *	-57 ± 3	170	-27 ± 7
1	300 **	-57 ± 1	200	-23 ± 6

X-ray scattering techniques were employed to get information about the internal structure of released nanoparticles. SAXS results on NP in water and PB at 20 mg/mL revealed that the scattered intensity profiles derived from two different contributions *(Figure 81)*: DX-HA nanoparticles and free HA, not complexed with nanoparticles, characterized by a peak visible in the spectrum of nanoparticles in water at q = 0.058 $Å^{-1}$.

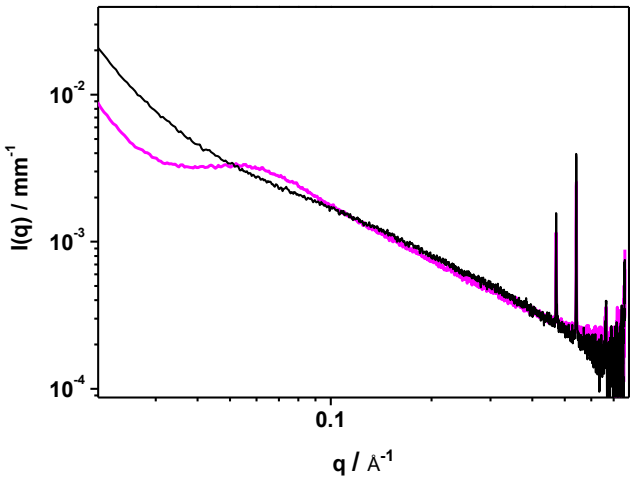

Figure 81. SAXS intensity profiles for DX-HA nanosuspension dispersed in water (magenta) and in PB (black).

This characteristic peak was observed also for sample in ethanol/water mixture before SD and it is probably due to the organization of HA in water, since it was not present in the spectrum obtained from particles in PB. In fact, in polyelectrolyte solutions, including polysaccharide chains, this peak was seen to be mainly modulated by repulsive electrostatic interactions, screened in presence of salt [131]. The correlation peak reflects the pseudo-periodic organization of polyelectrolyte chains in solution resulting from inter-chain repulsive interactions.

4.1.4 Bounded and unbounded sodium hyaluronate

To assess the fraction of the free HA both in water and PB, SAXS experiments were carried out on reconstituted nanoparticles at different concentrations and on HA solutions at the corresponding HA concentrations.

- **Sodium hyaluronate in solution**

Sodium hyaluronate solutions in the range 1.4 - 11.2 mg/mL were prepared and analysed by SAXS. The intensity profiles displayed the characteristic peak for polyelectrolytes in salt-free solution *(Figure 82)* [133]. The q value of the correlation peak (q_{peak}) depended on the inter-chain characteristic distance ξ according to $q_{peak} = 2\pi/\xi$. Therefore, with the increase of HA concentration, the measured correlation peak shifted to higher q values, corresponding to shorter inter-chain characteristic distances *(Table 39*, ξ value*)*.

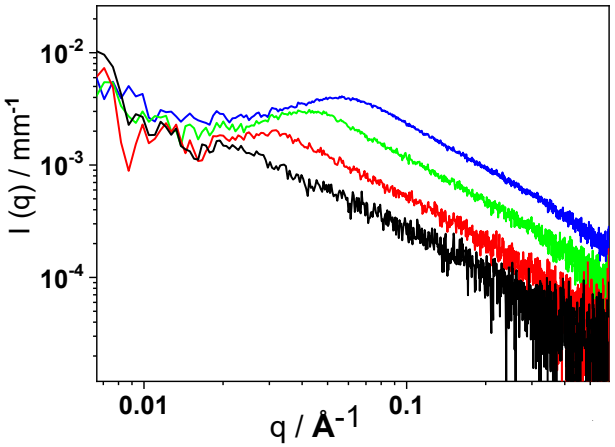

Figure 82. SAXS intensity profiles of HA in water at 1.4 mg/mL (black), 2.8 mg/mL (red), 5.6 mg/mL (green) and 11.2 mg/mL (blue).

Values of q_{peak} were plotted in function of HA concentration *(Figure 83, Panel A)*. A scaling with $c^{½}$ was derived, revealing the HA behaviour in salt-free solution for all the HA concentrations tested as a classical hydrophilic polyelectrolyte.

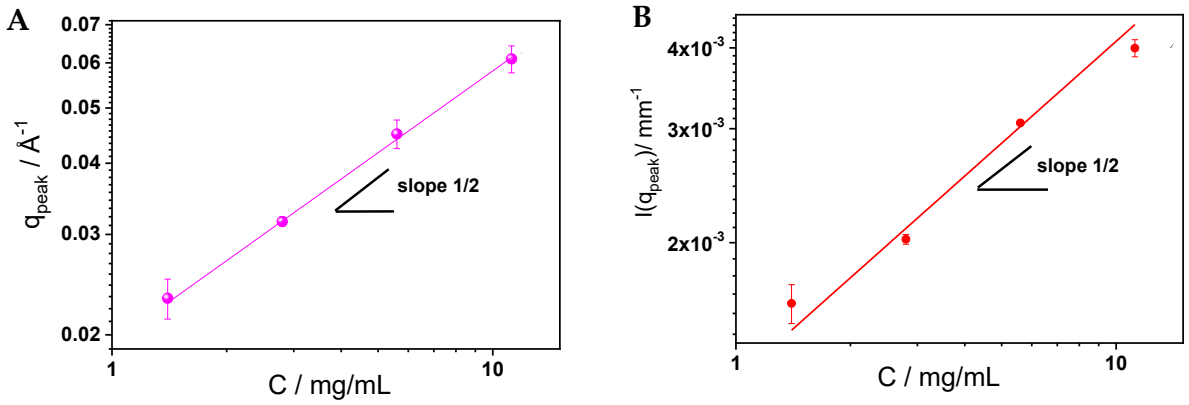

Figure 83. Scaling behaviour of the correlation peak position q_{peak} (Panel A) and of the scattered intensity at $q = q_{peak}$, $I(q_{peak})$ (Panel B).

The long-range electrostatic interactions govern the conformation of the polymer, which arranges in elongated rod-like chains, as reported for HA with similar molar mass [134]. The variation of the intensity of the scattered radiation $I(q_{peak})$ at $q = q_{peak}$ was scaled and reported in *Figure 83 (Panel B)*. The trend was proportional to $c^{½}$ as predicted by the model of Koyama for wormlike chain polymers with strong electrostatic interactions [135]. Its trend in the high-q range ($q > 0.2 - 0.3$ Å^{-1}) was determined from the spectra of HA in water. The values of the exponents, reported in *Table 39*, presented a similar value around 1.3, as expected for a rod-like conformation of HA in salt-free solution [134][136].

Table 39. Characteristic exponents (s) and inter-chain characteristic distance (ξ) of HA in water at different concentrations.

C (mg/mL)	ξ (Å)	s
1.4	270	1.3
2.8	220	1.3
5.6	140	1.3
11.2	110	1.3

Parallel SAXS experiments on solutions of HA in PB were carried out. Compared to those of HA in water, the intensity profiles presented differences both in low- and in high-q regions, with the disappearance of the polyelectrolyte correlation peak *(Figure 84).*

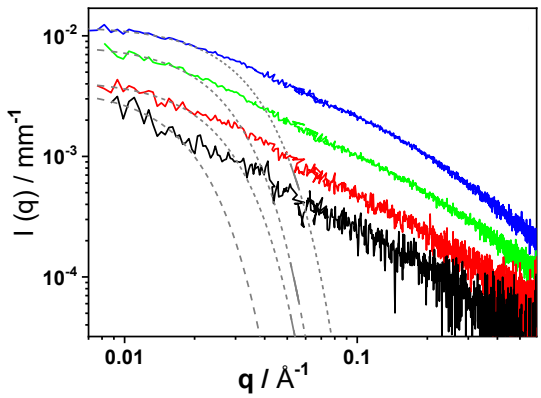

Figure 84. SAXS intensity profiles of HA in PB at 1.4 mg/mL (black), 2.8 mg/mL (red), 5.6 mg/mL (green) and 11.2 mg/mL (blue) with the corresponding Guinier Fit (gray dash line).

In PB, in fact, HA chains are governed not only by electrostatics, and the polymer can be modelled as a beaded necklace with globular denser regions [134]. The mean gyration radius of denser regions R_g was calculated according to the Guinier law [$I(q) = I_0 \exp(-q^2 \cdot R_g^2/3)$]. The size presented an inverse correlation with HA concentration, increasing from 54 to 98 Å with dilution. This behaviour was due to the reducing effect of electrostatics in case of diluted solutions of polyelectrolytes in the presence of non-zero ionic strength.

The trend of $I(q_{peak})$ at $q = q_{peak}$ at high-q values was determined also for HA in PB. The corresponding value of the exponents, reported in the *Table 40*, amounted to 1.3 at C < 3 mg/mL, similar to the salt-free conditions, and to 1.5 at higher concentrations.

Table 40. Characteristic exponents in PB (s) and mean gyration radius Rg at different HA concentrations.

C (mg/mL)	R_g (Å)	s
1.4	98	1.3
2.8	70	1.3
5.6	68	1.5
11.2	54	1.5

Therefore, HA presented a slight variation from the rod-like arrangement into a more compact conformation, while maintaining a quite rigidity and without assuming a random walk arrangement usually characterized by $I(q) = q_{peak}$ s = 2 [137].

- **<u>Bounded/unbounded sodium hyaluronate</u>**

Results about HA conformation in solution allowed to quantify the fraction of free and complexed HA after reconstitution of nanoparticles. DX-HA nanoparticles were redispersed at different concentrations in salt-free water and in PB. The intensity profiles obtained by SAXS, and reported in *Figure 85*, revealed the characteristic correlation peak of free HA in water at high concentrations (10 and 20 mg/mL), shifted at larger q-values with the increase of concentration *(Panel A)*.

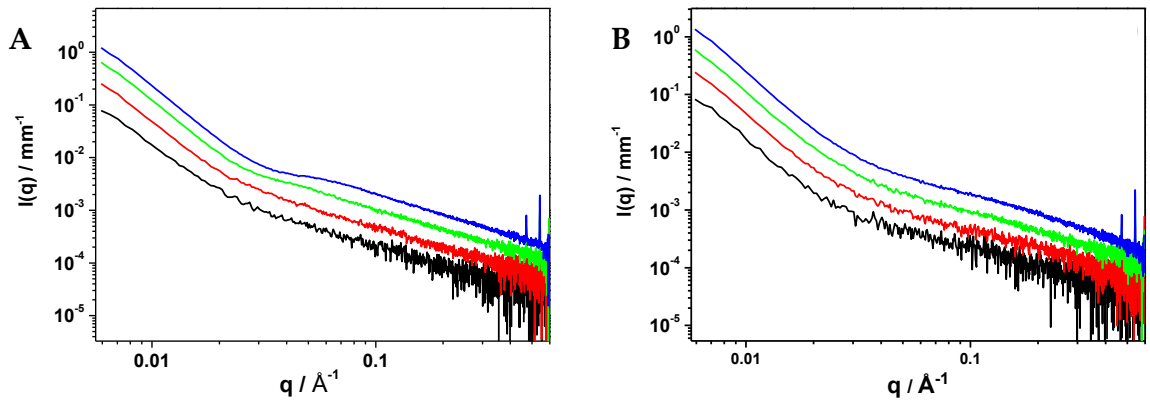

Figure 85. SAXS spectra of DX-HA nanoparticles at different concentrations in salt-free water (Panel A) and in PB (Panel B) at 2.5 mg/mL (black), 5 mg/mL (red), 10 mg/mL (green) and 20 mg/mL (blue).

SAXS analyses on DX-HA nanosuspensions were compared to the ones obtained from HA solutions at the same HA concentrations and reported in *Figure 86*. Obtained spectra showed differences in both peak position and intensity at high-q values, suggesting that a fraction of HA in DX-HA nanosuspensions was involved in particle formation, while a fraction was free in solution.

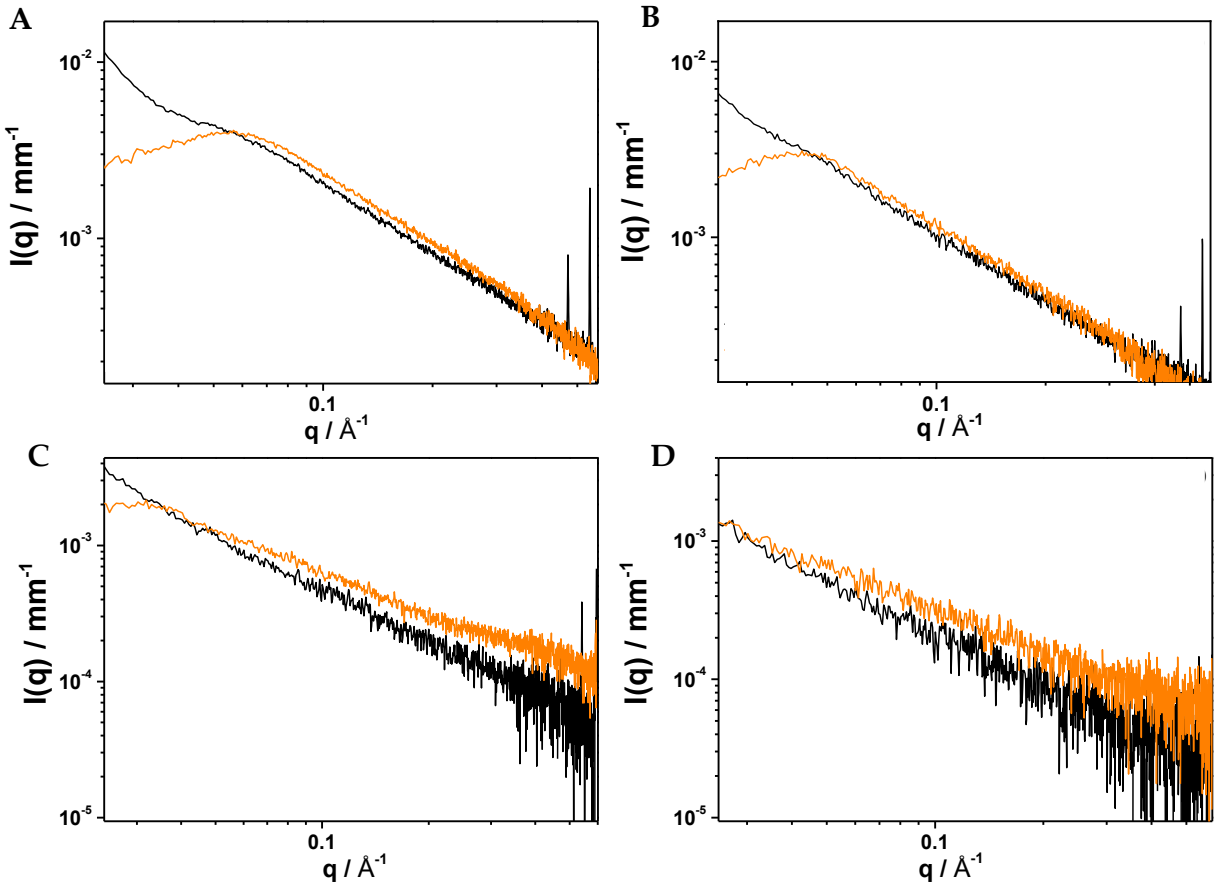

Figure 86. SAXS spectra of DX-HA nanoparticles (black) and HA (orange) in water, compared respectively at 20 mg/mL and 11.2 mg/mL (Panel A), 10 and 5.6 mg/mL (Panel B), 5 and 2.8 mg/mL (Panel C), 2.5 and 1.4 mg/mL (Panel D).

To quantify the exact fraction of free and complexed HA, different procedures were performed in parallel to reach reliable results.

Table 41. Fraction of bound/unbound HA as calculated by the analysis of the intensity contribution or by the q_{peak} position.

C_{NP} (mg/mL)	C_{HA} (mg/mL)	HA bounded/unbounded		
		Intensity water	Peak position (water)	Intensity PB
20	11.2	25/75	25/75	20/80
10	5.5	25/75	30/70	25/75
5	2.75	30/70	-	15/85
2.5	1.4	40/60	-	20/80

At C = 2.5 and 5 mg/mL, the deviation of the amount of free HA from the nominal concentration was visible as the difference in the intensity contribution at $q > 0.06$ Å^{-1}. For this reason, a fraction of free HA spectra was subtracted from the DX-HA ones in order to obtain similar intensity profiles, rigidly scaled in absolute intensity, as for identical nanoparticles at two different concentrations *(Figure 87)*.

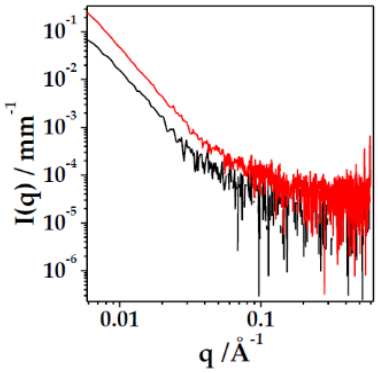

Figure 87. SAXS spectra of DX-HA nanoparticles obtained after subtraction of the scattered intensity contribution of unbounded HA.

The fraction of bound/unbound HA, reported in *Table 41*, was 30/70 and 40/60 for the samples at 5 mg/mL and 2.5 mg/mL, respectively. The experimental intensity profiles of DX-HA NP, obtained as described above, were then subtracted, after normalization for concentration, from the spectra of the 10 mg/mL and 20 mg/mL solutions, to obtain the intensity contribution of free HA. For the 20 mg/mL sample this process is reported in *Figure 88 (Panel A)*, with the obtainment of the purple signal.

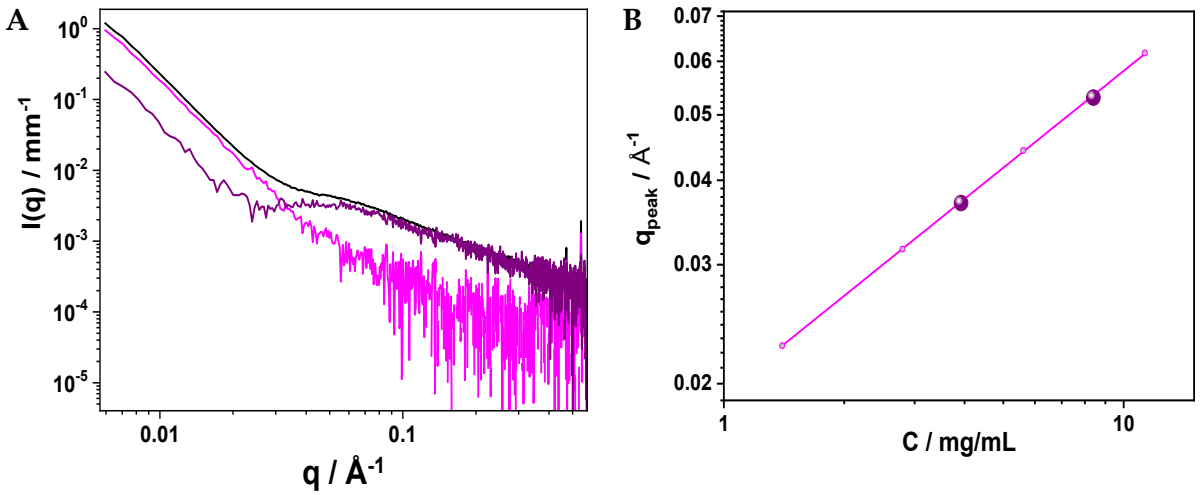

Figure 88. Panel A: SAXS spectra of DX-HA nanoparticles at 20 mg/mL in water (black), experimental intensity contribution of nanoparticles (magenta), difference between black and magenta signals (purple); Panel B: Peak position (q_{peak}) for 10 mg/mL and 20 mg/mL samples (purple dots). Magenta line represents the scaling behaviour of HA.

For the samples at higher concentrations, the correlation peak was visible, and its position could be determined and compared to the scaling law found for HA in water *(Figure 88, Panel B)*. On the scaling curve of HA, the experimental data *(dots)* lay at lower concentrations compared to the nominal ones, since a fraction of HA was involved in the DX NP. The actual concentration values of bound/unbound HA, reported in *Table 41*, were 25/75 for both the 10 mg/mL and 20 mg/mL solutions. Finally, also the absolute intensity of the contribution of unbound HA in the high q region was checked for samples at 10 mg/mL and 20 mg/mL to validate the procedure. Results, reported in the *Table 41* were in good agreement with the values obtained by the evaluation of the peak position.

For the DX-HA solutions in PB that did not show the correlation peaks, the fraction of bound/unbound HA was evaluated by the intensity discrepancy in the $q > 0.06$ Å^{-1} region, as reported in *Figure 89*. The contribution of complexed-HA in the solutions of DX-HA nanoparticles was about 20%, lower than the nominal content of HA, as estimated by subtraction to obtain intensity profiles realistic for nanoparticles *(Figure 90)*.

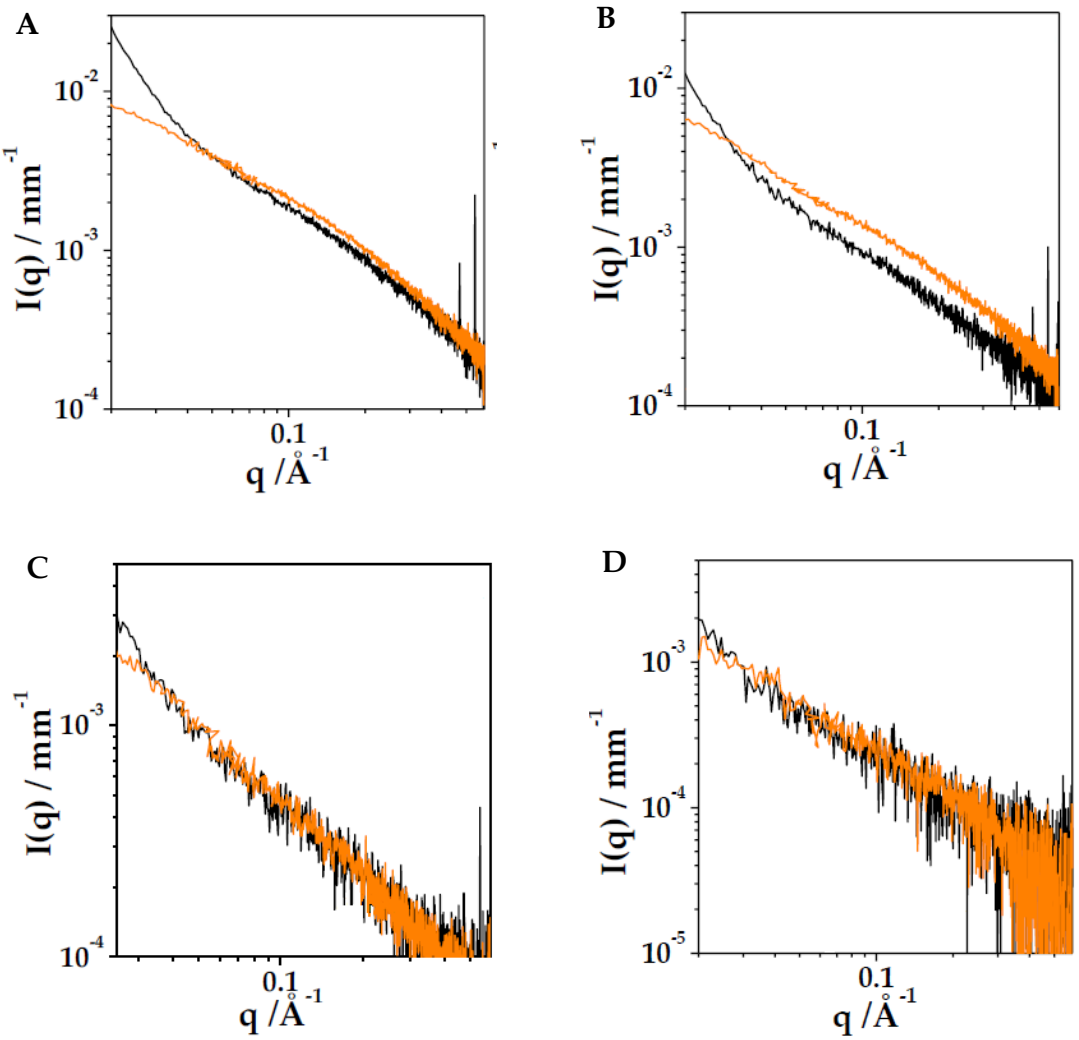

Figure 89. SAXS spectra of DX-HA nanoparticles (black) and HA (orange) in PB, compared respectively at 20 mg/mL and 11.2 mg/mL (Panel A), 10 and 5.6 mg/mL (Panel B), 5 and 2.8 mg/mL (Panel C), 2.5 and 1.4 mg/mL (Panel D).

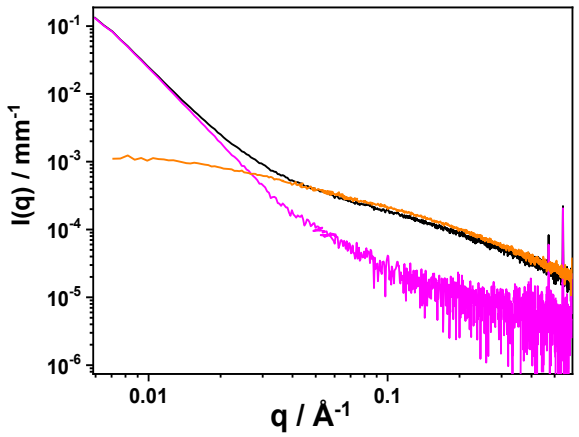

Figure 90. SAXS spectra of DX-HA NP at 20 mg/mL in PB (black), intensity contribution of HA at the same nominal concentration, 11.2 mg/mL (orange), difference between black and 0.8x orange signals (magenta) to obtain the contribution of NP.

The fraction of HA involved in the formation of DX-HA NP reconstituted in PB was slightly lower than in water, suggesting an influence of the environmental conditions on the final amount of HA associated with DX upon redispersion of microparticles. The presence of salt in the solvent could disturb the hydrogen bonding formation (DX/HA or HA/HA), allowing higher desorption of HA from the surface of the NP when dispersed in PB.

4.1.5 Nanoparticle structure

To determine the structure of NP, SAXS profiles of reconstituted DX-HA nanoparticles were obtained after subtraction of the intensity contribution of free HA. The spectra presented similar intensity decays at different concentrations and redispersion solvents. After modelling, all profiles fitted curves of a polydisperse core-shell sphere *(Figure 91)*.

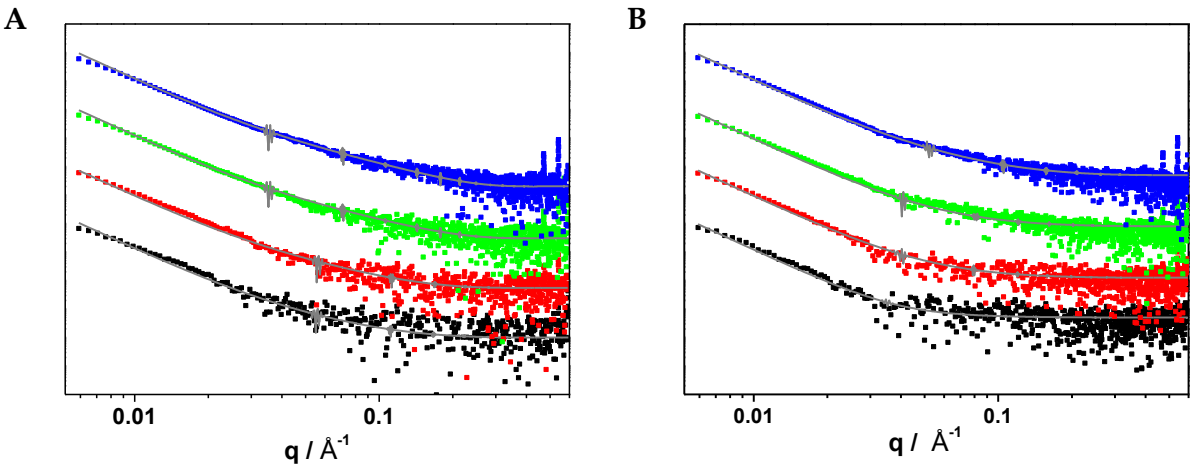

Figure 91. SAXS spectra of reconstituted DX-HA NP in water (Panel A) and PB (Panel B). Lines are the fit with a core-shell polydisperse spherical model.

In particular, the shape of the scattering curves was modelled using the form factor P(q) of polydisperse core-shell spherical particles ($i = 2$):

$$P(q) \div \left[\sum_{i=1}^{4} 3V_i\,(\rho_i - \rho_{i+1})\frac{\sin(qR_i) - qR_i\cos(qR_i)}{(qR_i)^3}\right]^2 \qquad \textit{(Eq. 8)}$$

where V_i and R_i indicate the volume and radius of the concentric spheres, and ρ_i are the scattering length densities (SLDs) of the core ($i = 1$) and of the shell ($i = 2$); ρ_3 is the scattering length density of the solvent. The polydispersity of particle size was determined based on Schultz distribution, corresponding to 0.2 for all systems.

Nanoparticles resulted formed by a core of about 200 nm (scattering length density = 11.8 $\cdot 10^{-6}$ Å^{-2}) surrounded by a thin shell of about 1.4 nm characterized by a high scattering length density (16 $\cdot 10^{-6}$ Å^{-2}) typical of polysaccharide chains *(Table 42)*.

Table 42. Particle structure after redispersion in water and phosphate buffer (PB) and SLD of particles and water.

C (mg/mL)	Core Radius (nm)		Shell Thickness (nm)	
	water	PB	water	PB
2.5	160	250	1.5	1.0
5	141	224	1.3	1.2
10	250	220	1.5	1.1
20	250	170	1.5	1.2

	SLD / Å^{-2}
Water	9.46 $\cdot 10^{-6}$
DX (core)	11.8 $\cdot 10^{-6}$
HA (shell)	16 $\cdot 10^{-6}$

Therefore, the structure of the nanoparticles was characterized by a DX core stabilized in suspension by the presence of HA chains, partially embedded in the core while partially surrounding the surface. This hypothesis was corroborated by features on the local scale, as assessed by parallel SAXS and WAXS measurements. In all the SAXS spectra, a sequence of narrow peaks was present in the high-q region (q_1 = 0.47 Å, q_2 = 0.54 Å), as could be easily visualized in *Figure 87* for the 20 mg/mL sample.

Moreover, WAXS measurements on the same samples showed characteristic diffraction patterns, preserved when nanoparticles were reconstituted in water and in PB *(Figure 92, Panels A* and *C)*. In both pattern the position of peaks was identical for all the investigated systems, while their intensities changed with concentration, as it can be observed in detail in *Panel B*. The experimental pattern was compared with the powder diffraction pattern of DX reported in literature and revealed a crystal structure identical to the DX orthorhombic geometry with lattice parameters a = 10.36 Å, b = 16.16 Å, c = 23.20 Å [138]. It can be

concluded that the internal structure of nanoparticles is so constituted by DX nanocrystals complexed into the core.

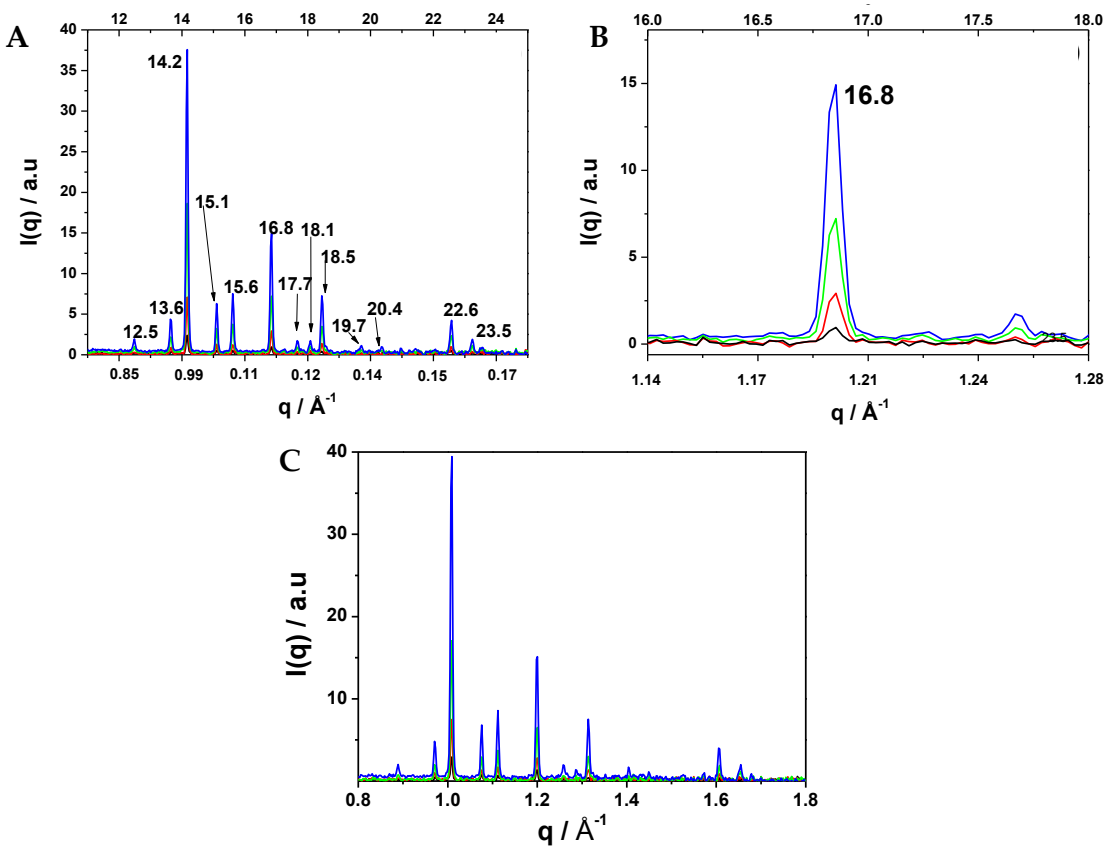

Figure 92. WAXS spectra of DX-HA NP in water (Panel A) and in PB (Panel C) in the full q range and in water in the region of one diffraction peak (Panel B). DX-HA at 2.5 (black), 5 (red), 10 (green) and 20 mg/mL (blue). Labels report the position of peaks expressed in 2θ.

4.1.6 Interaction with mucin

SAXS experiments were performed to assess the stability of nanoparticles in a mucus model, consisting of mucin at 0.5% and 1% w/v in PB. Their spectra, reported in *Figure 93 (Panel A)*, displayed the characteristic features of mucin in this range of concentration [139]. The intensity profile of DX-HA nanoparticles at 10 mg/mL in mucin 1% w/v was compared to the spectra of the two components at the same concentration in PB *(Figure 93, Panel B)*. Except for the low-q and high-q regions of the spectrum, most of the intensity signal resulted by the contribution of mucin.

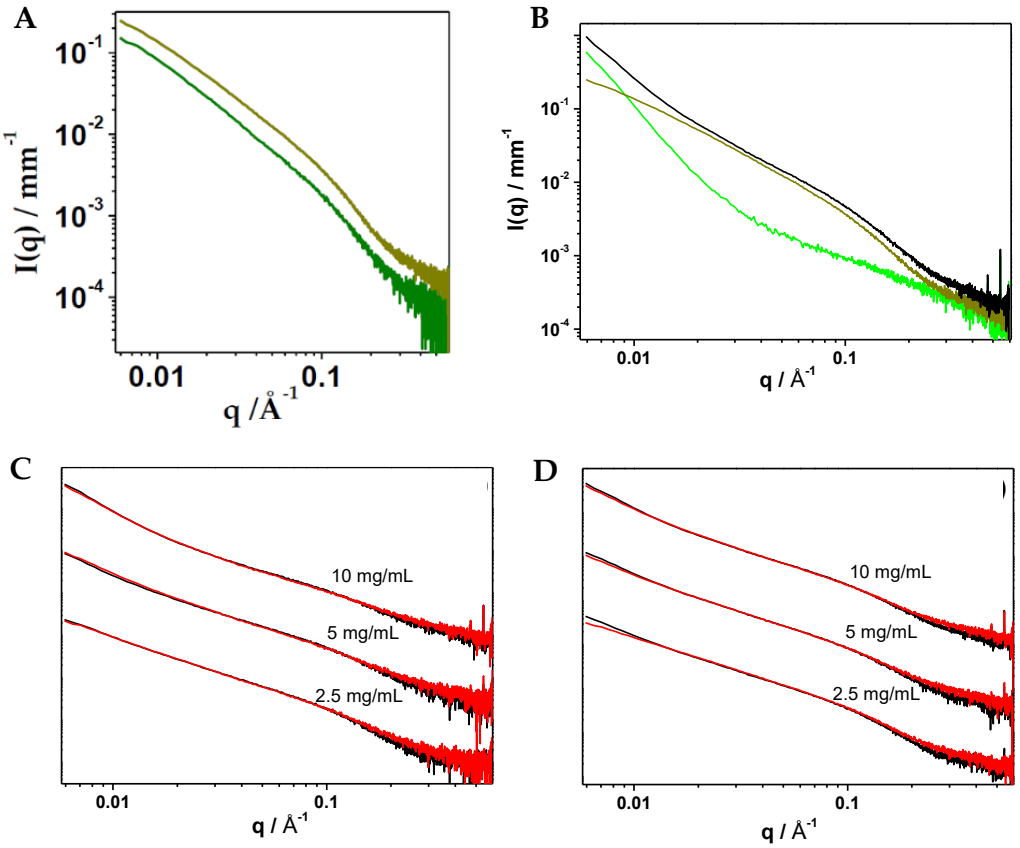

Figure 93. Panel A: SAXS spectra of mucin at 0.5% (green) and 1% w/v (dark yellow) in PB; B: SAXS intensity profiles of 10 mg/mL DX-HA (green), 1% w/v mucin (black) and mixed 10 mg/mL DX-HA nanoparticles in 1% w/v mucin (dark yellow); C and D: Scaled intensity profiles of DX-HA nanoparticles dispersed in mucin at 0.5% and 1% w/v, respectively (experimental profile in black and reconstructed profiles in red).

The same comparison was carried out at different concentrations of nanoparticles (2.5, 5 and 10 mg/mL), in both 0.5% and 1% (w/v) mucin *(Figure 93, Panel C* and *D)*. At 0.5% w/v mucin, it was possible to reconstruct the admixed spectra over the whole q-range, as for a mixture of non-interacting components. At 1% w/v mucin, a slight deviation of the linear-combination reconstruction from the experimental signals was visible in the low-q region only at 2.5 mg/mL nanoparticles.

Results indicate that nanoparticles were stable and did not change their structure when in interaction with mucin. This behaviour could be due to the unbound HA in solution and to the external shell of nanoparticles constituted by HA chains, conferring muco-inert properties and preventing the adhesion of mucin chains to the surface.

4.2 Aerodynamic performance

Aerodynamic performance of DX-HA microparticles was assessed comparing the use of a dry powder inhaler (DPI) and a nebulizer for the aerosolization *in vitro*. Powder distribution within the NGI apparatus is reported in *Figure 94.*

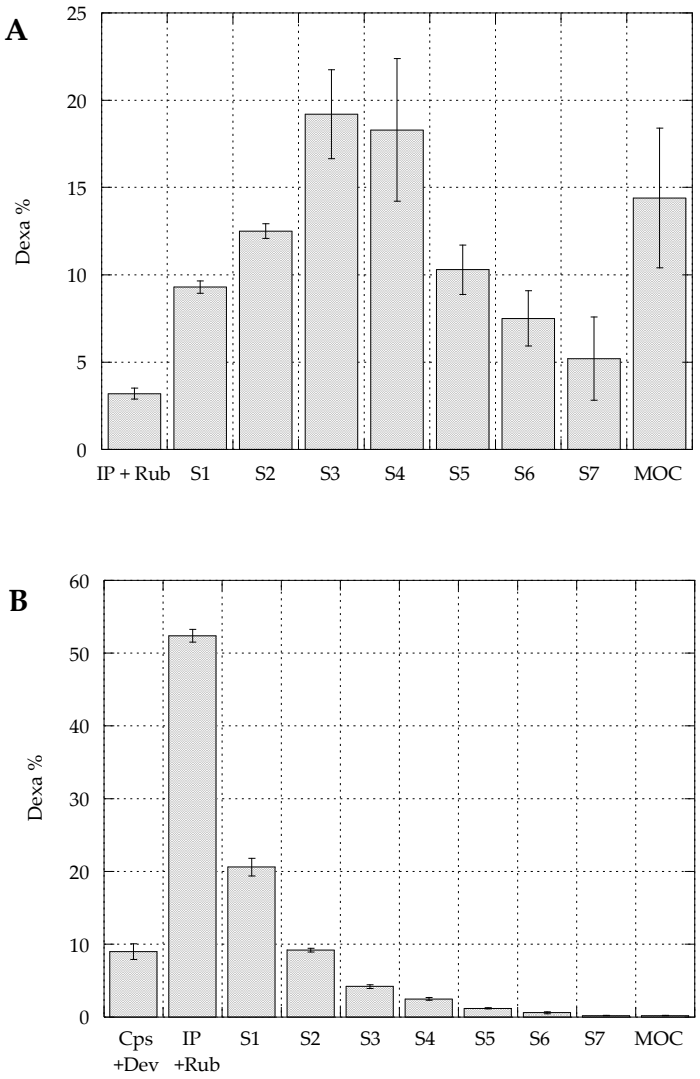

Figure 94. Powder distribution in the NGI apparatus after aerosolization with a nebulizer (Panel A) or a DPI (Panel B). The bars represent the standard deviation (n = 3).

Relevant aerodynamic parameters, reported in *Table 43*, allowed to compare the two methods of aerosolization and to get information about the performances of the DX-HA powder.

Table 43. Aerodynamic parameters of the powder. Mass median aerodynamic diameter (MMAD), geometric standard deviation (GSD), emitted dose and emitted fraction (ED and EF%), fine particle dose and fine particle fraction (FPD and FPF%). Mean ± standard deviation (n = 3).

	DPI	**Nebulizer**
MMAD (μm)	8.27 ± 0.25	4.66 ± 0.73
GSD	1.86 ± 0.05	3.93 ± 2.08
ED (mg)	3.06 ± 0.16	0.707 ± 0.113
EF%	90.96 ± 1.07	26.37 ± 2.88
FPD (mg)	0.607 ± 0.055	0.53 ± 0.09
FPF%	19.82 ± 0.99	74.97 ± 0.24

The EF% of powder aerosolised with the nebulizer was around 25% of the loaded dose, in agreement with the typical performance of this type of nebulizer [140], but significantly lower compared to the DPI, that presented an EF% of almost 91%. Nevertheless, in contrast to nebulization, the aerosolization with the DPI led to a lower FPF% amounting to 19% compared to 75% obtained using the nebulizer. It is worth noting that the FPD was comparable for both methods, amounting to 0.6 mg of powder. The higher FPF% of powder aerosolized with the nebulizer was justified by the lower MMAD, lower than 5 μm, that indicates good de-aggregation properties of the nanosuspension reconstituted from the spray-dried powder. This differed from the dry powder that presented a MMAD > 8 μm. In light of these results, nebulizer represents the better method for the aerosolization of DX-HA powder, considering that the relatively low EF%, in the proposed final application, could be overcome by nebulizing the nanosuspension directly in the pipe of a ventilator.

5. CONCLUSIONS

The aim of the present part of the thesis was to develop dexamethasone-sodium hyaluronate nanoparticles for the treatment of acute respiratory distress syndrome (ARDS). The research led to the production of a spray dried powder for inhalation containing DX-HA NP of 200 - 250 nm in size after reconstitution, consisting of a crystalline DX core surrounded by polymeric chains. The structure and the size resulted in a particulate system suitable to foster the alveolar macrophages pathway in the reduction of lung inflammation typical of ARDS. In fact, HA with high MW presents an anti-inflammatory effect that can work in synergy with its payload, in addition to enhancing its interaction with the targeted alveolar macrophages via CD44 binding. In addition, HA increases particle stability in mucus avoiding mucoadhesion, which represent a further positive aspect for the proposed application.

The studies of aerosolization *in vitro* revealed a better performance of the powder aerosolised using a high-efficiency nebulizer compared to a DPI. This positive aerosolization performance, that led to an FPF% = 75%, was the result of the peculiar structure of the suspended nanoparticles, constituted of the DX nanocrystals stabilized by a network of HA, mainly located at the interface with the solvent and making the first-stage biological identity of the nanoparticle. It is worth remembering that the nebulization led to a low value of EF% typical of nebulizers and here amounting to 26%. Nevertheless, this issue could be easily overcome by administering the nanosuspension directly in the pipe of the ventilation of the patients.

In conclusion, the present formulation represents a promising tool for the lung administration of dexamethasone, bypassing the systemic route, or complementing the parenteral administration as an adjunct therapy in patients in critical conditions, with severe lung inflammation.

CONCLUSIONS

The aim of the present thesis was to study the and set up a platform for pulmonary drug delivery based on the use of hyaluronic acid as active excipient in the construction of nanoparticles-embedding microparticulate respirable powders.

The study started with the investigation of HA MW for particle production, setting up the optimal conditions for the precipitation of nanoparticles *(Chapter 1)*. The concentration of the polymeric aqueous solution, the volume of anti-solvent and the temperature were investigated for each HA MW, basing on the viscosity of the solution as well as on the characteristics of nanoparticles in term of size and size distribution, obtained by DLS. Results highlighted some important outcomes, including the effect of HA concentration and of the volume of ethanol on particle size, and the positive effect of the increase of temperature on size distribution. In particular, for HA at high MW a lower concentration was employed (0.06% w/v) compared to HA at low MW (2% w/v). In contrast, a higher volume of ethanol, amounting to 90% v/v was necessary to precipitate HA NP at high MW. After setting up the optimal conditions for particle production, they were fixed to investigate the effect of HA MW on particle size and size distribution. The comparison revealed that HA with MW < 1000 kDa led to the production of bigger NP (hydrodynamic diameter > 200 nm) compared to high HA MW (hydrodynamic diameter < 100 nm), and with lower size distribution.

Once established the method for the preparation of blank HA NP, three different drugs were employed for the loading, in order to exploit HA-based carrier for pulmonary delivery, together with its biological effects. Amphotericin B, fluconazole and dexamethasone, employed for the treatments of various lung diseases, were successfully loaded into HA NP according to three different methods.

Amphotericin B-loaded HA NP were developed for potential use in the treatment of cystic fibrosis *(Chapter 2)*. For this purpose, HA 750-1000 kDa was employed. Due to the low solubility of AmB in both water and ethanol, the drug was first dissolved in propylene glycol and then added to the polymeric aqueous solution promoting the precipitation of drug NP. Ethanol, added dropwise to the mixture, promoted the precipitation of polymeric chains onto AmB NP creating drug-loaded nanocapsules with an EE% = 80%

and a hydrodynamic diameter between 60 - 80 nm. Dry powders for inhalation were obtained by spray drying, also in presence of excipients, including α-CD, β-CD and leucine. The presence of bulking agents enhanced the disaggregation of microparticles, but without restoring the original size of nanoparticles with hydrodynamic diameters around 200 nm. Tests *in vitro* on NCI-H441 and Calu-3 pulmonary cell lines guaranteed the safety of treatments for 4h and 24h with microparticles containing 1 - 50 μg/mL of AmB. Light microscopy allowed to assess over time the dissolution of particles in contact with mucus, after aerosolization on Calu-3 cell lines growth at ALI. The study revealed a faster release of nanoparticles in presence of α-CD and leucine, and, in comparison of AmB RM, of all nano-embedded microparticles.

Fluconazole-loaded HA NP were developed for the treatment of fungal pulmonary infections *(Chapter 3)*. For this purpose, HA 130-300 kDa was employed, thanks to the affinity for alveolar macrophages and in stimulating immune response. The drug was solubilized in water with the polymer, and ethanol was added dropwise to promote the simultaneous precipitation of the drug and the polymer with an EE% = 98%. Blank nanoparticles of 135 nm in diameter presented an increase to 200 nm when loaded with fluconazole, with a quite high polydispersion (PdI = 0.4). After spray drying, nanoparticles with size around 250 nm and 400 nm were released in aqueous medium at 0.5 mg/mL and 1 mg/mL, respectively. Negative surface around -40 mV was measured at both concentrations, suggesting the presence of polymeric chains on the outer surface of nanoparticles, able to enhance particle presentation and to bind alveolar macrophages through CD44 receptor.

Finally, dexamethasone-loaded HA NP were developed for the treatment of COVID-19-related acute respiratory distress syndrome *(Chapter 4)*. For this purpose, HA 750-1000 kDa was employed. In this case, the polymeric aqueous solution was added to an alcoholic solution of dexamethasone and then spray dried. SAXS and WAXS measurements revealed that before SD no nanoparticles were present in suspension. In contrast, after particle reconstitution in aqueous media (water and PB), nanoparticles around 200-250 nm were detected, thus suggesting the NP precipitation during the process of SD. In

particular, the faster evaporation of ethanol promoted the precipitation of DX-nanocrystals surrounded by polymeric chains, leading to the formation of a core-shell structure of 200 nm and a shell thickness of 1.4 nm, as described by SAXS analyses. Aerodynamic assessment revealed a better performance when the powder was resuspended in water and aerosolized using a nebulizer, guaranteeing a 74% (w/w of ED) of powder able to reach the deep lungs.

Concluding, a method for the production of HA nanoparticles has been developed. These particles, obtained with different HA MW and presenting a wide range of sizes, represent a versatile platform for pulmonary delivery of different active ingredients (API). In particular, it allows to reach different aims with just minor adjustments to the method and to the composition, according to the nature of the API being incorporated and of the desired type of targeting (alveolar macrophages or epithelial cells).

Bibliography

[1] A. Fallacara, E. Baldini, S. Manfredini, and S. Vertuani, "Hyaluronic acid in the third millennium," *Polymers (Basel).*, vol. 10, no. 7, 2018, doi: 10.3390/polym10070701.

[2] J. R. Fraser, T. C. Laurent, and U. B. Laurent, "Hyaluronan: its nature, distribution, functions and turnover," *J. Intern. Med.*, pp. 27–33, 1997.

[3] T. C. Laurent, "Nomenclature of hyaluronic acid," *Biochem. J.*, 1986.

[4] J. Necas, L. Bartosikova, P. Brauner, and J. Kolar, "Hyaluronic acid (hyaluronan): A review," *Vet. Med. (Praha).*, vol. 53, no. 8, pp. 397–411, 2008, doi: 10.17221/1930-VETMED.

[5] J. M. Cyphert, C. S. Trempus, and S. Garantziotis, "Size Matters: Molecular Weight Specificity of Hyaluronan Effects in Cell Biology," *Int. J. Cell Biol.*, vol. 2015, 2015, doi: 10.1155/2015/563818.

[6] A. D'Agostino *et al.*, "Is molecular size a discriminating factor in hyaluronan interaction with human cells?," *Carbohydr. Polym.*, vol. 157, pp. 21–30, 2017, doi: 10.1016/j.carbpol.2016.07.125.

[7] D. Y. Sirin *et al.*, "The association between different molecular weights of hyaluronic acid and CHAD , HIF-1 α , COL2A1 expression in chondrocyte cultures," *Exp. Ther. Med.*, vol. 15, pp. 4205–4212, 2018, doi: 10.3892/etm.2018.5943.

[8] S. Mizrahy *et al.*, "Hyaluronan-coated nanoparticles: The influence of the molecular weight on CD44-hyaluronan interactions and on the immune response," *J. Control. Release*, vol. 156, no. 2, pp. 231–238, 2011, doi: 10.1016/j.jconrel.2011.06.031.

[9] C. M. McKee *et al.*, "Hyaluronan (HA) fragments induce chemokine gene expression in alveolar macrophages: The role of HA size and CD44," *J. Clin. Invest.*, vol. 98, no. 10, pp. 2403–2413, 1996, doi: 10.1172/JCI119054.

[10] A. Avenoso *et al.*, "Hyaluronan fragments produced during tissue injury : A signal amplifying the inflammatory response," *Arch. Biochem. Biophys.*, vol. 663, pp. 228–238, 2019, doi: 10.1016/j.abb.2019.01.015.

[11] C. Termeer *et al.*, "Oligosaccharides of Hyaluronan Activate Dendritic Cells via Toll-like Receptor 4," *J. Exp. Med.*, vol. 195, no. 1, 2002.

[12] F. E. Lennon and P. A. Singleton, "Role of hyaluronan and hyaluronan-binding proteins in lung pathobiology," *Am. J. Physiol. - Lung Cell. Mol. Physiol.*, vol. 301, no. 2, 2011, doi: 10.1152/ajplung.00071.2010.

[13] H. Knop-Marques, M. Pravda, L. Wolfova, and V. Velebny, "Hyaluronic acid and its derivatives in coating and delivery systems: applications in tissue engineering, regenerative medicine and immunomodulation," *Adv. Healthc. Mater.*, vol. 5, no. 22, pp. 2841–2855, 2016.

[14] K. S. Girish and K. Kemparaju, "The magic glue hyaluronan and its eraser hyaluronidase: A biological overview," *Life Sci.*, vol. 80, no. 21, pp. 1921–1943, 2007.

[15] B. P. Toole, "Hyaluronan: From extracellular glue to pericellular cue," *Nat. Rev. Cancer*, vol. 4, no. 7, pp. 528–539, 2004, doi: 10.1038/nrc1391.

[16] E. A. Turley, P. W. Noble, and L. Y. W. Bourguignon, "Signaling properties of hyaluronan receptors," *J. Biol. Chem.*, vol. 277, no. 7, pp. 4589–4592, 2002.

[17] D. Vigetti, E. Karousou, M. Viola, S. Deleonibus, G. De Luca, and A. Passi, "Hyaluronan: Biosyntesis and signaling," *Biochim. Biophys. Acta - Gen. Subj.*, vol. 1840, no. 8, pp. 2452–2459, 2014.

[18] D. Jiang, J. Liang, and P. W. Noble, "Hyaluronan as an immune regulator in

human diseases," *Physiol. Rev.*, vol. 91, no. 1, pp. 221–264, 2011.

[19] R. Ebid, J. Lichtnekert, and H.-J. Anders, "Hyaluronan is not a ligand but a regulator of Toll-like receptor signaling in mesangial cells: Role of Extracellular matrix in innate immunity," *ISRN Nephrol.*, vol. 2014, 2014.

[20] K. R. Taylor, K. Yamasaki, K. A. Radek, D. Golenbock, B. Beutler, and R. L. Gallo, "Recognition of Hyaluronan Released in Sterile Injury Involves a Unique Receptor Complex Dependent on Toll-like Receptor 4, CD44, and MD-2," *J. Biol. Chem.*, vol. 282, no. 25, pp. 18265–18275, 2007.

[21] S. Garantziotis, Z. Li, E. N. Potts, and J. Y. Lindsey, "TLR4 is necessary for hyaluronan-mediated airway hyperresponsiveness after ozone inhalation," *Am. J. Respir. Crititcal Care Med.*, vol. 181, no. 7, pp. 666–675, 2010.

[22] K. E. Black *et al.*, "Hyaluronan fragments induce IFNβ via a novel TLR4-TRIF-TBK1-IRF3- dependent pathway," *J. Inflamm.*, vol. 10, no. 1, pp. 1–9, 2013, doi: 10.1186/1476-9255-10-23.

[23] D. Jiang, J. Liang, J. Fan, S. Yu, and S. Chen, "Regulation of lung injury and repair by Toll-like receptors and hyaluronan," *Nat. Med.*, vol. 11, no. 11, pp. 1173–1179, 2005.

[24] J. E. Rayahin, J. S. Buhrman, Y. Zhang, T. J. Koh, and R. A. Gemeinhart, "High and Low Molecular Weight Hyaluronic Acid Differentially Influence Macrophage Activation," *ACS Biomater. Sci. Eng.*, vol. 1, no. 7, pp. 481–493, 2015, doi: 10.1021/acsbiomaterials.5b00181.

[25] M. Dovedytis, Z. J. Liu, and S. Bartlett, "Hyaluronic acid and its biomedical applications: A review," *Eng. Regen.*, vol. 1, pp. 102–113, 2020, doi: 10.1016/j.engreg.2020.10.001.

[26] S. Vasvani, P. Kulkarni, and D. Rawtani, "Hyaluronic acid: A review on its biology, aspects of drug delivery, route of administrations and a special

emphasis on its approved marketed products and recent clinical studies," *Int. J. Biol. Macromol.*, vol. 151, pp. 1012–1029, 2020, doi: 10.1016/j.ijbiomac.2019.11.066.

[27] R. Altman, A. Bedi, A. Manjoo, and F. Niazi, "Anti-inflammatory effects of intra-articular hyaluronic acid: a systematic review," *Cartilage*, vol. 10, no. 1, pp. 43–52, 2019.

[28] A. Fallacara, L. Busato, M. Pozzoli, M. Ghadiri, H. X. Ong, and P. M. Young, "Co-spray-dried urea cross-linked hyaluronic acid and sodium ascorbyl phosphate as novel inhalable dry powder formulation," *J. Pharm. Sci.*, vol. 108, pp. 2964–2971, 2019.

[29] S. Garantziotis, M. Brezina, P. Castelnuovo, and L. Drago, "The role of hyaluronan in the pathophisiology and treatment of respiratory disease," *Am. J. Physiol. - Lung Cell. Mol. Physiol.*, vol. 310, pp. 785–795, 2016.

[30] G. Huang and H. Huang, "Application of hyaluronic acid as carriers in drug delivery," *Drug Deliv.*, vol. 25, no. 1, pp. 766–772, 2018.

[31] G. Y. Lee, J.-H. Kim, K. Y. Choi, H. Y. Yoon, and K. Kim, "Hyaluronic acid nanoparticles for active targeting atherosclerosis," *Biomaterials*, vol. 53, pp. 341–348, 2015.

[32] A. P. Bernardes Almeida, G. Bernardes Rodrigues Damaceno, A. F. Carneiro, and A. Bohr, "Mucopenetrating lipoplexes modified with PEG and hyaluronic acid for CD44-targeted local siRNA delivery to the lungs," *J. Biomater. Appl.*, vol. 34, no. 5, pp. 617–630, 2019.

[33] C. Buzea, I. I. Pacheco, and K. Robbie, "Nanomaterials and nanoparticles: Sources and toxicity," *Biointerphases*, vol. 2, no. 4, pp. 17–71, 2007.

[34] M. J. Mitchell, M. M. Billingsley, R. M. Haley, M. E. Wechsler, N. A. Peppas, and R. Langer, "Engineering precision nanoparticles for drug delivery," *Nat. Rev. Drug Discov.*, vol. 20, pp. 101–124, 2021.

[35] I. Venditti, "Morphologies and functionalities of polymeric nanocarriers as chemical tools for drug delivery: A review," *J. King Saud Univ. - Sci.*, vol. 31, pp. 398–411, 2019, doi: 10.1016/j.jksus.2017.10.004.

[36] K. M. El-Say and H. S. El-Sawy, "Polymeric nanoparticles: Promising platform for drug delivery," *Int. J. Pharm.*, vol. 528, pp. 675–691, 2017.

[37] J. U. Menon, P. Ravikumar, A. Pise, D. Gyawali, C. C. W. Hsia, and K. T. Nguyen, "Polymeric nanoparticles for pulmonary protein and DNA delivery," *Acta Biomater.*, vol. 10, no. 6, pp. 2643–2652, 2014, doi: 10.1016/j.actbio.2014.01.033.

[38] M. Bodnár, L. Daróczi, and G. Batta, "Preparation and characterization of cross-linked hyaluronan nanoparticles," *Colloid Polym. Sci.*, vol. 287, pp. 991–1000, 2009, doi: 10.1007/s00396-009-2061-9.

[39] X. Deng *et al.*, "Hyaluronic acid-chitosan nanoparticles for co-delivery of MiR-34a and doxorubicin in therapy against triple negative breast cancer," *Biomaterials*, vol. 35, pp. 4333–4344, 2014, doi: 10.1016/j.biomaterials.2014.02.006.

[40] A. Almalik, R. Donno, C. J. Cadman, F. Cellesi, P. J. Day, and N. Tirelli, "Hyaluronic acid-coated chitosan nanoparticles: Molecular weight-dependent effects on morphology and hyaluronic acid presentation," *J. Control. Release*, vol. 172, pp. 1142–1150, 2013, doi: 10.1016/j.jconrel.2013.09.032.

[41] M. De La Fuente, B. Seijo, and M. J. Alonso, "Novel Hyaluronan-Based nanocarriers for transmucosal delivery of macromolecules," *Macromol. Biosci.*, vol. 8, pp. 441–450, 2008, doi: 10.1002/mabi.200700190.

[42] S. Boddohi, N. Moore, P. A. Johnson, and M. J. Kipper, "Polysaccharide-based polyelectrolyte complex nanoparticles from chitosan, heparin, and hyaluronan," *Biomacromolecules*, vol. 10, pp. 1402–1409, 2009, doi: 10.1021/bm801513e.

[43] F. A. Oyarzun-Ampuero, F. M. Goycoolea, D. Torres, and M. J. Alonso, "A new drug nanocarrier consisting of polyarginine and hyaluronic acid," *Eur. J. Pharm.*

Biopharm., vol. 79, pp. 54–57, 2011.

[44] I. Rossi *et al.*, "Sodium hyaluronate nanocomposite respirable microparticles to tackle antibiotic resistance with potential application in treatment of mycobacterial pulmonary infections," *Pharmaceutics*, vol. 11, no. 203, 2019.

[45] W. H. Lee, C. Y. Loo, D. Traini, and P. M. Young, "Nano- and micro-based inhaled drug delivery systems for targeting alveolar macrophages," *Expert Opin. Drug Deliv.*, vol. 12, pp. 1009–1026, 2015, doi: 10.1517/17425247.2015.1039509.

[46] G. Mattheolabakis, L. Milane, A. Singh, and M. M. Amiji, "Hyaluronic acid targeting of CD44 for cancer therapy: from receptor biology to nanomedicine," *J. Drug Target.*, vol. 23, no. 7–8, pp. 605–618, 2015.

[47] L. Yang *et al.*, "Hyaluronic acid/chitosan nanoparticles for delivery of curcuminoid and its in vitro evaluation in glioma cells," *Int. J. Biol. Macromol.*, vol. 72, pp. 1391–1401, 2015, doi: 10.1016/j.ijbiomac.2014.10.039.

[48] S. Yin *et al.*, "Intracellular delivery and antitumor effects of a redox-responsive polymeric paclitaxel conjugate based on hyaluronic acid," *Acta Biomater.*, vol. 26, pp. 274–285, 2015, doi: 10.1016/j.actbio.2015.08.029.

[49] K. Y. Choi, G. Saravanakumar, J. H. Park, and K. Park, "Hyaluronic acid-based nanocarriers for intracellular targeting: Interfacial interactions with proteins in cancer," *Colloids Surfaces B Biointerfaces*, vol. 99, pp. 82–94, 2012, doi: 10.1016/j.colsurfb.2011.10.029.

[50] J. E. Hastedt *et al.*, "Scope and relevance of a pulmonary biopharmaceutical classification system AAPS/FDA/USP Workshop March 16-17th, 2015 in Baltimore, MD," AAPS Open, 2016. doi: 10.1186/s41120-015-0002-x.

[51] J. S. Patton and P. R. Byron, "Inhaling medicines: delivering drugs to the body through the lungs," *Nat. Rev. Drug Discov.*, vol. 6, pp. 67–74, 2007.

[52] M. Ibrahim, R. Verma, and L. Garcia-Contreras, "Inhalation drug delivery

devices: Technology update," *Med. Devices Evid. Res.*, vol. 8, pp. 131–139, 2015, doi: 10.2147/MDER.S48888.

[53] J. C. Sung, B. L. Pulliam, and D. A. Edwards, "Nanoparticles for drug delivery to the lungs," *Trends Biotechnol.*, vol. 25, no. 12, pp. 563–570, 2007, doi: 10.1016/j.tibtech.2007.09.005.

[54] S. P. Newman, "Drug delivery to the lungs: challenges and opportunities," *Ther. Deliv.*, vol. 8, no. 8, pp. 647–661, 2017.

[55] T. Praphawatvet, J. I. Peters, and R. O. Williams, "Inhaled nanoparticles - An updated review," *Int. J. Pharm.*, vol. 587, p. 119671, 2020, doi: 10.1016/j.ijpharm.2020.119671.

[56] Q. Liu, J. Guan, L. Qin, X. Zhang, and S. Mao, "Physicochemical properties affecting the fate of nanoparticles in pulmonary drug delivery," *Drug Discov. Today*, vol. 25, no. 1, pp. 150–159, 2020, doi: 10.1016/j.drudis.2019.09.023.

[57] M. A. Lemke, "Amphotericin B," *Appl. Microbiol. Biotechnol.*, no. 68, pp. 151–162, 2005, doi: 10.1007/s00253-005-1955-9.

[58] I. Echevarría, C. Barturen, M. J. Renedo, and M. C. Dios-Viéitez, "High-performance liquid chromatographic determination of amphotericin B in plasma and tissue. Application to pharmacokinetic and tissue distribution studies in rats," *J. Chromatogr. A*, vol. 819, no. 1–2, pp. 171–176, 1998, doi: 10.1016/S0021-9673(98)00425-7.

[59] P. Snetkov, K. Zakharova, S. Morozkina, R. Olekhnovich, and M. Uspenskaya, "Hyaluronic acid: The influence of molecular weight on structural, physical, physico-chemical, and degradable properties of biopolymer," *Polymers (Basel).*, vol. 12, pp. 1–33, 2020, doi: 10.3390/polym12081800.

[60] L. Ambrosio, A. Borzacchiello, P. A. Netti, and L. Nicolais, "Rheological study on hyaluronic acid and its derivative solutions," *J. Macromol. Sci. - Pure Appl.*

Chem., vol. 36 A, no. 7–8, pp. 991–1000, 1999, doi: 10.1080/10601329908951195.

[61] E. Fouissac, M. Milas, and M. Rinaudo, "Shear-Rate, concentration, molecular weight, and temperature viscosity dependences of hyaluronate, a wormlike polyelectrolyte," *Macromolecules*, vol. 26, pp. 6945–6951, 1993, doi: 10.1021/ma00077a036.

[62] S. J. Falcone, D. M. Palmeri, and R. A. Berg, "Rheological and cohesive properties of hyaluronic acid," *J. Biomed. Mater. Res. - Part A*, vol. 76A, no. 4, pp. 721–728, 2006, doi: 10.1002/jbm.a.30623.

[63] A. Fakhari, Q. Phan, S. V Thakkar, C. R. Middaugh, and C. Berkland, "Hyaluronic Acid Nanoparticles Titrate the Viscoelastic Properties of Viscosupplements," *Langmuir, ACS*, 2013, doi: 10.1021/la304575x.

[64] Z. Li, G. Lu, and G. Meng, "Pathogenic fungal infection in the lung," *Front. Immunol.*, vol. 10, pp. 1–20, 2019, doi: 10.3389/fimmu.2019.01524.

[65] N. Rajagopalan, M. C. Dicken, L. J. Ravin, and L. A. Sternson, "A study of the solubility of amphotericin B in nonaqueous solvent systems," *J. Parenter. Sci. Technol.*, vol. 42, pp. 97–102, 1988.

[66] Y. Zu *et al.*, "Preparation and characterization of amorphous amphotericin B nanoparticles for oral administration through liquid antisolvent precipitation," *Eur. J. Pharm. Sci.*, vol. 53, pp. 109–117, 2014, doi: 10.1016/j.ejps.2013.12.005.

[67] C. Ernst, J. Grange, and L. D. S. De, "Structure of Amphotericin B aggregates as revealed by UV and CD spectroscopies," *Biopolymers*, vol. 20, pp. 1575–1588, 1981.

[68] P. Sawangchan, "The effect of aggregation state on the degradation kinetics of Amphotericin B in aqueous solution," 2017.

[69] S. Castellani, S. Di Gioia, L. Di Toma, and M. Conese, "Human cellular models for the investigation of lung inflammation and mucus production in cystic

fibrosis," *Anal. Cell. Pathol.*, vol. 2018, pp. 1–15, 2018, doi: 10.1155/2018/3839803.

[70] D. A. Stoltz, D. K. Meyerholz, and M. J. Welsh, "Origins of Cystic Fibrosis Lung Disease," *N. Engl. J. Med.*, vol. 372, pp. 351–362, 2015, doi: 10.1056/nejmra1300109.

[71] M. M. Rey, M. P. Bonk, and D. Hadjiliadis, "Cystic fibrosis: Emerging understanding and therapies," *Annu. Rev. Med.*, vol. 70, pp. 197–210, 2019, doi: 10.1146/annurev-med-112717-094536.

[72] A. L. Cooney, P. B. McCray, and P. L. Sinn, "Cystic fibrosis gene therapy: Looking back, looking forward," *Genes (Basel).*, vol. 9, no. 538, pp. 1–23, 2018, doi: 10.3390/genes9110538.

[73] K. A. Muraglia *et al.*, "Small-molecule ion channels increase host defences in cystic fibrosis airway epithelia," *Nature*, vol. 567, no. 7748, pp. 405–408, 2019, doi: 10.1038/s41586-019-1018-5.

[74] R. S. Chorghade, B. R. Kim, J. L. Launspach, P. H. Karp, M. J. Welsh, and M. D. Burke, "Amphotericin B induces epithelial voltage responses in people with cystic fibrosis," *J. Cyst. Fibros.*, 2020, doi: 10.1016/j.jcf.2020.11.018.

[75] S. P. Vyas, S. Quraishi, S. Gupta, and K. S. Jaganathan, "Aerosolized liposome-based delivery of amphotericin B to alveolar macrophages," *Int. J. Pharm.*, vol. 296, pp. 12–25, 2005, doi: 10.1016/j.ijpharm.2005.02.003.

[76] G. Muniz Fèlix Araujo, A. R. Albuquerque Barros, J. A. Oshiro-Junior, L. Ferreira Soares, and L. Guerra da Rocha, "Nanoemulsions loaded with Amphotericin B: development, characterization and leishmanicidal activity," *Curr. Pharm. Des.*, vol. 25, pp. 1616–1622, 2019, doi: 10.2174/1381612825666190705202030.

[77] P. Jansook, Z. Fülöp, and G. C. Ritthidej, "Amphotericin B loaded solid lipid nanoparticles (SLNs) and nanostructured lipid carrier (NLCs): physicochemical and solid-solution state characterizations," *Drug Dev. Ind. Pharm.*, vol. 45, no. 4,

pp. 560–567, 2019, doi: 10.1080/03639045.2019.1569023.

[78] K. Gilani, E. Moazeni, T. Ramezanli, M. Amini, and M. R. Fazeli, "Development of Respirable Nanomicelle Carriers for Delivery of Amphotericin B by Jet Nebulization," *J. Pharm. Sci.*, vol. 100, no. 1, pp. 252–259, 2011, doi: 10.1002/jps.22274.

[79] D. M. Kamiński, "Recent progress in the study of the interactions of amphotericin B with cholesterol and ergosterol in lipid environments," *Eur. Biophys. J.*, vol. 43, pp. 453–467, 2014, doi: 10.1007/s00249-014-0983-8.

[80] M. V. Chaubal and C. Popescu, "Conversion of nanosuspensions into dry powders by spray drying: A case study," *Pharm. Res.*, vol. 25, no. 10, pp. 2302–2308, 2008, doi: 10.1007/s11095-008-9625-0.

[81] A. Grenha, B. Seijo, and C. Remuñán-López, "Microencapsulated chitosan nanoparticles for lung protein delivery," *Eur. J. Pharm. Sci.*, vol. 25, pp. 427–437, 2005, doi: 10.1016/j.ejps.2005.04.009.

[82] D. M. K. Jensen, D. Cun, M. J. Maltesen, S. Frokjaer, H. M. Nielsen, and C. Foged, "Spray drying of siRNA-containing PLGA nanoparticles intended for inhalation," *J. Control. Release*, vol. 142, pp. 138–145, 2010, doi: 10.1016/j.jconrel.2009.10.010.

[83] S. Kumar, R. Gokhale, and D. J. Burgess, "Sugars as bulking agents to prevent nano-crystal aggregation during spray or freeze-drying," *Int. J. Pharm.*, vol. 471, pp. 303–311, 2014, doi: 10.1016/j.ijpharm.2014.05.060.

[84] T. Lebhardt, S. Roesler, H. P. Uusitalo, and T. Kissel, "Surfactant-free redispersible nanoparticles in fast-dissolving composite microcarriers for dry-powder inhalation," *Eur. J. Pharm. Biopharm.*, vol. 78, pp. 90–96, 2011, doi: 10.1016/j.ejpb.2010.12.002.

[85] N. Alhajj, N. J. O'Reilly, and H. Cathcart, "Leucine as an excipient in spray dried

powder for inhalation," *Drug Discov. Today*, vol. 26, no. 10, pp. 2384–2396, 2021, doi: 10.1016/j.drudis.2021.04.009.

[86] A. Bouchard, G. W. Hofland, and G. J. Witkamp, "Properties of sugar, polyol, and polysaccharide water-ethanol solutions," *J. Chem. Eng. Data*, vol. 52, pp. 1838–1842, 2007, doi: 10.1021/je700190m.

[87] M. A. Boraey, S. Hoe, H. Sharif, D. P. Miller, D. Lechuga-Ballesteros, and R. Vehring, "Improvement of the dispersibility of spray-dried budesonide powders using leucine in an ethanol-water cosolvent system," *Powder Technol.*, vol. 236, pp. 171–178, 2013, doi: 10.1016/j.powtec.2012.02.047.

[88] A. K. Chatjigakis, C. Donzé, A. W. Coleman, and P. Cardot, "Solubility behavior of beta-Cyclodextrin in water/cosolvent mixtures," *Anal. Chem.*, vol. 64, no. 14, pp. 1632–1634, 1992.

[89] Y. Chang, Y. H. Wang, and C. Q. Hu, "Simultaneous determination of purity and potency of amphotericin B by HPLC," *J. Antibiot. (Tokyo).*, vol. 64, pp. 735–739, 2011, doi: 10.1038/ja.2011.83.

[90] M. E. Kreft *et al.*, "The characterization of the human cell line Calu-3 under different culture conditions and its use as an optimized in vitro model to investigate bronchial epithelial function," *Eur. J. Pharm. Sci.*, vol. 69, pp. 1–9, 2015, doi: 10.1016/j.ejps.2014.12.017.

[91] N. Sibinovska, S. Žakelj, R. Roškar, and K. Kristan, "Suitability and functional characterization of two Calu-3 cell models for prediction of drug permeability across the airway epithelial barrier," *Int. J. Pharm.*, vol. 585, pp. 1–10, 2020, doi: 10.1016/j.ijpharm.2020.119484.

[92] M. M. Nociari, A. Shalev, P. Benias, and C. Russo, "A novel one-step, highly sensitive fluorometric assay to evaluate cell- mediated cytotoxicity," *J. Immunol. Methods*, vol. 213, pp. 157–167, 1998, doi: 10.1016/S0022-1759(98)00028-3.

[93] M. A. Selo, J. A. Sake, K.-J. Kim, and C. Ehrhardt, "In vitro and ex vivo models in inhalation biopharmaceutical research - advances, challenges and future perspectives," *Adv. Drug Deliv. Rev.*, vol. 177, pp. 1–32, 2021, doi: 10.1016/j.addr.2021.113862.

[94] I. Martinez, *Properties of some particular solutions*. Universidad Politecnica de Madrid, 2015.

[95] L. Ferreira da Silva, R. da Silva Eustacio, M. R. Fraguas Neto, C. de Souza Silva, M. F. Mendes, and C. de S. Siqueira Pereira, "Simulation of the Extractive Distillation Process of Ethanol-Water-Propylene Glycol System," *J. Thermodyn. Catal.*, vol. 8, no. 3, pp. 1–5, 2017, doi: 10.4172/2157-7544.1000191.

[96] R. Vehring, "Pharmaceutical particle engineering via spray drying," *Pharm. Res.*, vol. 25, no. 5, pp. 999–1022, 2008, doi: 10.1007/s11095-007-9475-1.

[97] I. Gatej, M. Popa, and M. Rinaudo, "Role of the pH on hyaluronan behavior in aqueous solution," *Biomacromolecules*, vol. 6, pp. 61–67, 2005, doi: 10.1021/bm040050m.

[98] Y. Cui, Y. Ding, L. Chen, Y. Li, Y. C. Li, and H. Nie, "Dexmedetomidine enhances human lung fluid clearance through improving alveolar sodium transport," *Fundam. Clin. Pharmacol.*, vol. 31, pp. 429–437, 2017, doi: 10.1111/fcp.12278.

[99] D. Y. Han *et al.*, "K+ channel openers restore verapamil-inhibited lung fluid resolution and transepithelial ion transport," *Respir. Res.*, vol. 11, no. 65, pp. 1–17, 2010, doi: 10.1186/1465-9921-11-65.

[100] C. I. Grainger, L. L. Greenwell, D. J. Lockley, G. P. Martin, and B. Forbes, "Culture of Calu-3 cells at the air interface provides a representative model of the airway epithelial barrier," *Pharm. Res.*, vol. 23, no. 7, pp. 1482–1490, 2006, doi: 10.1007/s11095-006-0255-0.

[101] E. Cingolani, S. Alqahtani, R. C. Sadler, D. Prime, S. Stolnik, and C. Bosquillon,

"In vitro investigation on the impact of airway mucus on drug dissolution and absorption at the air-epithelium interface in the lungs," *Eur. J. Pharm. Biopharm.*, vol. 141, pp. 210–220, 2019, doi: 10.1016/j.ejpb.2019.05.022.

[102] B. E. de Pauw, "What are fungal infections?," *Mediterr. J. Hematol. Infect. Dis.*, vol. 3, pp. 1–8, 2011, doi: 10.4084/MJHID.2011.001.

[103] A. K. Haque, "Pathology of common pulmonary fungal infection," *J. Thorac. Imaging*, vol. 7, no. 4, pp. 1–11, 1992.

[104] B. N. Nelson, A. N. Hawkins, and K. L. Wozniak, "Pulmonary Macrophage and Dendritic Cell Responses to Cryptococcus neoformans," *Front. Cell. Infect. Microbiol.*, vol. 10, pp. 1–10, 2020, doi: 10.3389/fcimb.2020.00037.

[105] T. Di Mambro, I. Guerriero, L. Aurisicchio, M. Magnani, and E. Marra, "The yin and yang of current antifungal therapeutic strategies: How can we harness our natural defenses?," *Front. Pharmacol.*, vol. 10, pp. 1–11, 2019, doi: 10.3389/fphar.2019.00080.

[106] A. M. Nicola *et al.*, "Antifungal drugs: New insights in research & development," *Pharmacol. Ther.*, vol. 195, pp. 21–38, 2019, doi: 10.1016/j.pharmthera.2018.10.008.

[107] L. Ostrosky-Zeichner, A. Casadevall, J. N. Galgiani, F. C. Odds, and J. H. Rex, "An insight into the antifungal pipeline: Selected new molecules and beyond," *Nat. Rev. Drug Discov.*, vol. 9, pp. 719–727, 2010, doi: 10.1038/nrd3074.

[108] K. L. Goa and L. B. Barradell, "Fluconazole," *Drugs*, vol. 50, no. 4, pp. 658–690, 1995.

[109] N. P. Wiederhold, "Antifungal resistance: current trends and future strategies to combat," *Infect. Drug Resist.*, vol. 10, pp. 249–259, 2017.

[110] E. L. Berkow and S. R. Lockhart, "Fluconazole resistance in Candida species: a current perspective," *Infect. Drug Resist.*, vol. 10, pp. 237–245, 2017.

[111] J. A. Smith and C. A. Kauffman, "Pulmonary fungal infections," *Respirology*, vol. 17, pp. 913–926, 2012, doi: 10.1111/j.1440-1843.2012.02150.x.

[112] M. A. Moustafa, Y. S. R. Elnaggar, W. M. El-Refaie, and O. Y. Abdallah, "Hyalugel-integrated liposomes as a novel ocular nanosized delivery system of fluconazole with promising prolonged effect," *Int. J. Pharm.*, vol. 534, no. 1–2, pp. 14–24, 2017.

[113] S. El-Housiny, M. A. Shams Eldeen, Y. A. El-Attar, and H. A. Salem, "Fluconazole-loaded solid lipid nanoparticles topical gel for treatment of pityriasis versicolor: formulation and clinical study," *Drug Deliv.*, vol. 25, no. 1, pp. 78–90, 2018.

[114] M. Ghosh, S. Mandal, A. Roy, and S. Chakrabarty, "Enhanced antifungal activity of fluconazole conjugated with Cu-Ag-ZnO nanocomposite," *Mater. Sci. Eng. C*, vol. 106, pp. 1–10, 2020.

[115] B. Patel, N. Gupta, and F. Ahsan, "Particle engineering to enhance or lessen particle uptake by alveolar macrophages and to influence the therapeutic outcome," *Eur. J. Pharm. Biopharm.*, vol. 89, pp. 163–174, 2015, doi: 10.1016/j.ejpb.2014.12.001.

[116] S. M. Hwang, D. D. Kim, S. J. Chung, and C. K. Shim, "Delivery of ofloxacin to the lung and alveolar macrophages via hyaluronan microspheres for the treatment of tuberculosis," *J. Control. Release*, vol. 129, no. 2, pp. 100–106, 2008, doi: 10.1016/j.jconrel.2008.04.009.

[117] V. Porta, K. H. Chang, and S. Storpirtis, "Evaluation of the bioequivalence of capsules containing 150 mg of fluconazole," *Int. J. Pharm.*, vol. 288, pp. 81–86, 2005, doi: 10.1016/j.ijpharm.2004.09.013.

[118] P. A. Rivera, M. C. Martinez-Oharriz, M. Rubios, J. M. Irache, and S. Espuelas, "Fluconazole encapsulation in PLGA microspheres by spray-drying," *J.*

Microencapsul., vol. 21, no. 2, pp. 203–211, 2004, doi: 10.1080/02652040310001637811.

[119] Dexamethasone, PubChem, *Compound Summary*.

[120] D. B. Johnson, M. J. Lopez, and B. Kelley, *Dexamethasone*. 2018.

[121] S. Ramamoorthy and J. A. Cidlowski, "Corticosteroids: Mechanisms of Action in Health and Disease," *Rheum. Dis. Clin. North Am.*, vol. 42, no. 1, pp. 15–31, 2016.

[122] J. Zhong, J. Tang, C. Ye, and L. Dong, "The immunology of COVID-19: is immune modulation an option for treatment?," *Lancet Rheumatol.*, vol. 2, no. 7, pp. 428–436, 2020.

[123] "Dexamethasone for the Treatment of Coronavirus Disease (COVID-19): a Review," *Ahmed, M. H. Hassan, A.*, vol. 2, pp. 2637–2646, 2020.

[124] M. Ciaccio and L. Agnello, "Biochemical biomarkers alterations in Coronavirus Disease 2019 (COVID-19)," *Diagnosis*, vol. 7, no. 4, pp. 365–372, 2020, doi: 10.1515/dx-2020-0057.

[125] N. Pillalamarri *et al.*, "Exploring the utility of extracellular vesicles in ameliorating viral infection-associated inflammation, cytokine storm and tissue damage," *Transl. Oncol.*, vol. 14, no. 7, pp. 1–7, 2021, doi: 10.1016/j.tranon.2021.101095.

[126] P. Horby, W. S. Lim, J. R. Emberson, R. Haynes, and M. J. Landray, "Dexamethasone in Hospitalized Patients with Covid-19," *N. Engl. J. Med.*, vol. 384, no. 8, pp. 693–704, 2021, doi: 10.1056/nejmoa2021436.

[127] T. Lammers *et al.*, "Dexamethasone nanomedicines for COVID-19," *Nat. Nanotechnol.*, vol. 15, pp. 618–624, 2020, doi: 10.1038/s41565-020-0751-0.

[128] H. Lee, S. W. Jeong, E. Jung, and D. Lee, "Dexamethasone-loaded H2O2-

activatable anti-inflammatory nanoparticles for on-demand therapy of inflammatory respiratory diseases," *Nanomedicine Nanotechnology, Biol. Med.*, vol. 30, p. 102301, 2020, doi: 10.1016/j.nano.2020.102301.

[129] European Department for the Quality of Medicines, "European Pharmacopeia, 5th ed.," Strasbourg, 2004, p. 433.

[130] C. I. Camara *et al.*, "Hyaluronic Acid-Dexamethasone nanoparticles for local adjunct therapy of lung inflammation," *Int. J. Mol. Sci.*, vol. 22, p. 10480, 2021, doi: 10.3390/ijms221910480.

[131] M. Michel, "Organization in semi-dilute polyeleetrolyte solutions observed by Small-Angle Neutron Scattering," *J. Appl. Crystallogr.*, vol. 11, pp. 519–523, 1978.

[132] J. Kim, J.-Y. Chang, Y.-Y. Kim, M.-J. Kim, and H.-S. Kho, "Effects of molecular weight of hyaluronic acid on its viscosity and enzymatic activities of lysozyme and peroxidase," *Arch. Oral Biol.*, vol. 89, pp. 55–64, 2018.

[133] S. Popa-Nita, C. Rochas, L. David, and A. Domard, "Structure of Natural Polyelectrolyte Solutions: Role of the Hydrophilic/Hydrophobic Interaction Balance," *Langmuir, ACS*, vol. 25, no. 11, pp. 6460–6468, 2009.

[134] G. Lalevèe *et al.*, "Polyelectrolyte complexes via desalting mixtures of hyaluronic acid and chitosan - Physicochemical study and structural analysis," *Carbohydr. Polym.*, vol. 154, pp. 86–95, 2016.

[135] R. Koyama, "Small-angle scattering of polyelectrolyte solutions," *Macromolecules*, vol. 17, no. 8, pp. 1594–1598, 1984.

[136] F. Heatley and J. E. Scott, "A water molecule participates in the secondary structure of hyaluronan," *Biochem. J.*, vol. 254, no. 2, pp. 489–493, 1988.

[137] P. Schurtenberger, *Neutron, X-rays and Light. Scattering Methods Applied to Soft Condensed Matter*, 1st Ed. Amsterdam: Elsevier, 2002.

[138] J. W. Raynor, W. Minor, and M. Chruszcz, "Dexamethasone at 119 K," *Acta Crystallogr. Sect. E*, vol. E63, pp. o2791–o2793, 2007.

[139] E. Di Cola *et al.*, "Novel O/W nanoemulsions for nasal administration: Structural hints in the selection of performing vehicles with enhanced mucopenetration," *Colloids Surfaces B Biointerfaces*, vol. 183, p. 110439, 2019.

[140] F. Buttini *et al.*, "Combinations of colistin solutions and nebulisers for lung infection management in cystic fibrosis patients," *Int. J. Pharm.*, vol. 502, pp. 242–248, 2016, doi: 10.1016/j.ijpharm.2016.02.005.